TRAPPING TRIPLY IONIZED THORIUM ISOTOPES

A Thesis
Presented to
The Academic Faculty

by

Layne R. Churchill

In Partial Fulfillment
of the Requirements for the Degree
Doctor of Philosophy in the
School of Physics

Georgia Institute of Technology
December 2010

TRAPPING TRIPLY IONIZED THORIUM ISOTOPES

Approved by:

Michael Chapman, Advisor
School of Physics
Georgia Institute of Technology

T.A. Brian Kennedy
School of Physics
Georgia Institute of Technology

Kenneth Brown
School of Chemistry
Georgia Institute of Technology

Alex Kuzmich
School of Physics
Georgia Institute of Technology

Jennifer Curtis
School of Physics
Georgia Institute of Technology

Date Approved: 30 July 2010

To He who created all things, and in whom, all things are held together

ACKNOWLEDGEMENTS

Sometimes it feels like I have lived an entire lifetime at Georgia Tech. I know that statement can be taken in several ways, but I mean it in a positive sense. I am very grateful that I have had this opportunity to learn so much and meet so many wonderful people. There are many people I would like to thank for their support and friendship.

I would especially like to thank my Ph.D advisor, Dr. Michael Chapman. I recall an incident in my early days in the lab when, in some display of ignorance typical of a new graduate researcher, I drew the ire of my colleague Adam Steele who exclaimed (only half-jokingly) to Mike, who happened to be present, "Where did you get this guy?" Mike simply smiled and said, "Everyone gets a chance to learn." That incident has stuck with me, because I think it demonstrates the noble philosophy of a true educator. Mike created an environment that allowed me to mature into a competent experimentalist and atomic physicist. In the process, I was able to take part in the first stages of two exciting experiments on the cutting edge of atomic physics. And because of that, I am one of the very few people in the world who can say that he's seen a single atom with his naked eye. For that I am very grateful.

I would also like to thank Dr. Alex Kuzmich. Alex and Mike started the thorium ion trapping experiment together, and it has been a privilege to work with Alex and his students. Alex approaches his experiments with an intensity that is contagious. He is a marvel to watch when confronted with a physics problem. He has one of the sharpest and fastest minds of any person I have ever met.

It would be wrong for me to leave Adam Steele in the slightly negative light of my earlier anecdote any longer. Adam has been a trusted colleague and a close friend. Adam is an extremely talented scientist; I have learned much from his example. His leadership

and tenacity helped our group overcome many experimental hurdles. He is one of the most honest and principled persons I have ever had the pleasure of knowing. I was honored to have Adam stand beside me when I was married in June of 2008, and I will be honored to stand next to him when he is married this December.

It has been a pleasure as well to work with Corey Campbell. Corey reflects the intensity of his advisor, the aforementioned Alex Kuzmich. He is ambitious and unrelenting. I have thoroughly enjoyed pondering the future of the thorium experiment with Corey at each of its many stages. He too has been a great friend and colleague. I wish him the greatest success in all his future endeavors, especially in his attempts to use his acting and dancing talents to break into the world of entertainment.

I have also been fortunate to work alongside Michael DePalatis. Michael has an excellent work ethic and a great many talents that have made him a valuable member of the thorium ion trapping experiment. Michael is also a great source for the latest news. All I ever had to ask him was, "What should I be outraged about today, Michael?", and he would give me the scoop.

There have been many others in the Chapman lab who have made my experience here that much more fulfilling. Kevin Fortier, Paul Griffin, and Ming-Shien Chang were my early mentors. Soo Kim always made the lab a more pleasant place to work with her warmth and caring spirit. Michael Gibbons did his best to always make me feel welcome in the lab. Christopher Hamley was always able to give me answers for questions, even questions I never asked. Chung-Yu Shih was always in the lab as late at night as I was, so I never felt lonely. Peyman Ahmadi was a valuable resource for information. He and his wife, Ghazal, nurtured the community spirit of the lab.

I would like to especially thank Joanna Hass and Eva Bookjans for their friendship and for being such great study partners. They helped make studying for the graduate physics courses and the qualifying exam more bearable.

This thesis could not have been completed without the support and encouragement

of my parents, Gene and Dawn Churchill. I thank them for always being there for me, especially through the tough times in my undergraduate education when I was struggling to figure out what to do with the rest of my life.

My wife, Victoria Churchill, has been a tremendous source of comfort and strength through many stressful times. Her family's warmth and generosity gave me a home away from home here in Georgia. I am glad they are now my family too. It was while I was at Georgia Tech that I first met Victoria. During my time here, she has been my friend, girlfriend, fiancé, and finally my wife. She has made it all worthwhile.

Finally, I would like to thank my Lord and Savior, Jesus Christ. "I know how to be brought low, and I know how to abound. In any and every circumstance, I have learned the secret of facing plenty and hunger, abundance and need. I can do all things through him who strengthens me." (Philippians 4:12,13)

TABLE OF CONTENTS

CHAPTERS

APPENDICES

LIST OF TABLES

LIST OF FIGURES

LIST OF SYMBOLS OR ABBREVIATIONS

BIP	built-in purifier (BIP is a registered trademark of Air Products and Chemicals, Inc.).
CCD	charge coupled device.
CEM	channel electron multiplier.
CF	conflat.
DC	direct current.
ECDL	extended cavity diode laser.
FWHM	full-width half-maximum.
GPS	Global Positioning System.
Nd:YAG	neodymium-doped yttrium aluminum garnet.
ppb	parts-per-billion.
ppm	parts-per-million.
PZT	piezoelectric transducer.
RF	radio-frequency.
ROI	region of interest.
SNR	signal-to-noise ratio.
THC	total hydrocarbons.
UHP	ultra-high purity.
UHV	ultra-high vacuum.
UV	ultraviolet.

LIST OF LISTINGS

SUMMARY

Cold trapped ions have many applications in quantum information science and precision metrology. In this thesis, we present progress toward two objectives involving ions confined to linear RF traps: the strong coupling of Ba^+ ions with a high finesse optical cavity, and the observation of an optical nuclear transition in $^{229}Th^{3+}$. In pursuit of the first objective, a novel high-temperature vapor cell for the spectroscopy of neutral barium was constructed. Using this vapor cell, a new technique for isotope-selective photoionization loading of Ba^+ in an ion trap was developed. In pursuit of the second objective, techniques ultimately to be used in creating, trapping, and observing $^{229}Th^{3+}$ are studied using $^{232}Th^{3+}$. Ion traps are loaded with $^{232}Th^{3+}$ via laser ablation of thorium targets. $^{232}Th^{3+}$ is detected optically using laser-induced fluorescence and electronically using a channel electron multiplier. A technique for creating ablation targets from trace quantities of thorium nitrate is presented. The primary loss mechanisms of Th^{3+}, charge exchange and chemical reactions, are studied.

CHAPTER I

INTRODUCTION

Among the many contributions of atomic physics to the world of science, two that have had an especially profound impact on modern technology are the laser and the atomic clock. The Information Age owes much to the creation of the laser, as its use revolutionized the telecommunications industry. The fiber-optic cables that carry information encoded in optical signals have vastly higher bandwidth capabilities than their coaxial copper predecessors. Furthermore, the laser is featured in a number of consumer electronic devices such as CD, DVD, and Blu-Ray players, laser printers and laser pointers. They find continued use in manufacturing, medicine, and research.

The laser may owe its invention to the field of atomic physics, but its use has in turn opened up many new areas of research in the science that created it. Lasers can be used to control both the external and internal degrees of freedom of an atom. In 1975, Wineland and Dehmelt [1], and independently, Hänsch and Schawlow [2], proposed using the radiation pressure exerted by a laser tuned slightly below the resonance of an electronic transition to cool atoms. For their further development of the technique of laser cooling, Steven Chu, William Phillips, and Claude Cohen-Tannoudji were awarded the 1997 Nobel Prize in Physics. The technique is now routinely used in laboratories the world over to cool atoms and ions to fractions of a degree above absolute zero. Laser cooling was instrumental in the first demonstrations of Bose-Einstein Condensation [3, 4], for which Eric Cornell, Carl Wieman, and Wolfgang Ketterle shared the 2001 Nobel Prize in Physics.

As an experimental resource, cold atoms offer a significant advantage over atoms at room temperature: at microkelvin temperatures, atoms essentially stand still, allowing for long periods of interrogation and observation. This property of cold atoms has led to their

use in numerous applications. Quantum logic gates [5–7] and quantum teleportation [8, 9] have been demonstrated using cold trapped ions. Cold atomic ensembles have been used to implement long-lived quantum memory [10]. New high precision measurements of the fine structure constant [11, 12] have been performed. The use of cold atoms has greatly enhanced the sensitivity of inertial sensors [13] and atomic clocks.

Atomic clocks are the current standard-bearers in precision timekeeping. The Global Positioning System (GPS) [14], which has become a ubiquitous element of navigation in military, commercial, and personal applications, relies on the accuracy of atomic clocks in determining the position of a receiver on earth. Each GPS satellite features multiple atomic clocks, which it uses to encode the precise time (accurate to within 10s of nanoseconds) along with its position in each of its transmissions. GPS receivers then use transmissions from multiple satellites to triangulate their position to within just a few meters. Synchronization to the GPS time standard allows businesses and banks to better regulate their transactions, and helps public utility companies manage their vital infrastructure. Because of atomic clocks, the second is now the most precise unit of measure known to man [15].

The first atomic frequency standard was developed in 1955 by Louis Essen [16] at the National Physical Laboratory (NPL) in Great Britain. The clock measured the ground state hyperfine splitting in cesium by directing an atomic beam through two physically separated microwave oscillators in a technique developed by Ramsey [17]. It had an uncertainty of 1 part in 10^9. Decades of research in atomic beam clocks at the National Institute of Standards and Technology (NIST) culminated in the NIST-7, which achieved a fractional uncertainty of 5 parts in 10^{15} [18] and acted as the United States national primary frequency standard (NPFS) from 1993 to 1998 [15].

One of the primary limitations of a clock based on an atomic beam is the short interrogation time. The linewidth of the peak that defines the resonance is inversely proportional to the time between the points of microwave interaction. Atoms moving at thermal velocities pass quickly between these points, but by using cold atoms, the interrogation time can

be extended considerably. The current NPFS, NIST-F1, which uses cold cesium atoms to make its frequency measurement, has achieved an accuracy of 4×10^{-16} [15]. Measurements of optical transitions in cold atoms confined to optical lattices and cold trapped ions are reaching even higher levels of accuracy. New frequency standards based upon optical transitions in atomic strontium [19] and ytterbium [20] are being explored. Fractional uncertainties in the measurement of optical transitions in Hg^+ and Al^+ ions have reached 1.9×10^{-17} and 2.3×10^{-17}, respectively [21].

In this thesis, we present progress toward the realization of a new potential frequency standard based upon a unique nuclear transition in ^{229}Th. Beyond its use as a clock, the transition may provide orders of magnitude greater sensitivity in measurements of time variation of fundamental constants. Furthermore, the demonstration of coherent control of a nucleus with a laser would represent a new bridge between atomic and nuclear physics. In order to observe the transition, we intend to confine and laser cool triply-ionized ^{229}Th in an ion trap. Using the more common thorium isotope, ^{232}Th, and building upon our experience in trapping and laser cooling singly-ionized barium, our group has demonstrated the creation, trapping, and laser cooling of Th^{3+}.

In the next section, our group's initial work in barium ion trapping will be introduced. That will be followed by a discussion of the optical nuclear transition in ^{229}Th and our progress toward the ultimate goal of observing it in laser cooled $^{229}Th^{3+}$. The chapter concludes with a description of the specific contributions of the present work, and an outline of the rest of the thesis.

1.1 Barium Ion Trapping

The epoch of cold trapped ion research at Georgia Tech occurred on February 28, 2006. The fluorescence of a small cloud of singly-ionized barium was observed inside a linear RF ion trap. The experiment was performed in the laboratory of Dr. Michael Chapman, and the experimental effort was led by Adam Steele. Steele was assisted by the present author

and Dr. Paul Griffin, a post-doctoral researcher.

The ultimate goal of the barium ion trapping experiment is to integrate a miniature ion trap with a high-finesse optical cavity. This architecture would facilitate experiments exploring long term interactions between single ions and single photons. There are many intriguing applications for such a system. For example, an ion strongly coupled to a cavity could serve as a quantum repeater or single-photon generator in a quantum information network or processing system [22]. Barium was specifically chosen for this experiment because the optical transitions between its low-lying energy states are in the visible spectrum, where high quality mirrors are available.

In pursuit of this goal, we developed a new two-photon photoionization scheme for barium [23]. The first step in this technique involves the resonant excitation of neutral barium atoms on an intercombination transition between the $^1S_0$ ground state and the $^3P_1$ state. This is done with a diode laser at 791 nm. From the $^3P_1$ state, the atoms are ionized with 337 nm light from a nitrogen pulse laser.

The linewidth of the 791 nm transition used in the first step of the photoionization process is much less than the shift in resonance between the various barium isotopes. By tuning the 791 nm laser to the resonance of a particular barium isotope, we are able to exclusively load that isotope into the ion trap. The ability to tune the 791 nm laser to the resonance of a particular isotope is made possible by a novel, high-temperature vapor cell that is used for the spectroscopy of neutral barium. This vapor cell is discussed extensively in Chapter 3.

The valuable knowledge and experience provided by the early progress in the barium ion trapping experiment were eventually applied to another ion trapping experiment, which is introduced in the next section. Singly-ionized barium was used as a diagnostic tool for initially testing the first ion traps used in this second experiment.

1.2 Observation of an Optical Nuclear Transition in $^{229}Th^{3+}$

Unlike most atomic nuclei, which have excitation energies in the range of keV to MeV, the nucleus of the thorium isotope, ^{229}Th, has an excited state just several eV above the nuclear ground state. The transition between the nuclear ground state and this unique isomeric state lies within the UV optical spectrum, where it can be addressed using coherent light sources. The coherent control of the electronic states of atoms with tunable lasers has been a major focal point of modern atomic physics. Extending this paradigm to the control of nuclear states of atoms would represent a significant achievement. The transition between the states could potentially be used as a frequency reference with a fractional uncertainty approaching 10^{-20} [24]. Furthermore, the transition may be especially sensitive to changes in the value of the fine structure constant, allowing up to $5-6$ orders of magnitude enhancement in measurements of its time variation [25]. However, this latter point is one of some contention [26–28].

1.2.1 Concept

Since its discovery by Kroger and Reich in 1976 [29], the existence of the low-lying metastable nuclear state, which is denoted ^{229m}Th, has been well-established experimentally [30–34]. However, the transition between it and the nuclear ground state, ^{229g}Th, has never been directly observed. Each of the reported values for the transition energy has been determined by comparing gamma decay paths through the two states from a common nuclear excited state. By calculating the difference between the two paths in terms of total gamma energy emitted, the difference in energy between the ^{229g}Th and ^{229m}Th states was inferred. Obtaining a precise result using this method is difficult given the energy scales involved. The method calls for adding and subtracting gamma decay energies on the order of 10s of keV and obtaining an energy for the $^{229g}\text{Th} \leftrightarrow {}^{229m}\text{Th}$ transition that is on the order of only a few eV.

The most recent measurement of the energy of the ^{229m}Th state was made by Beck et

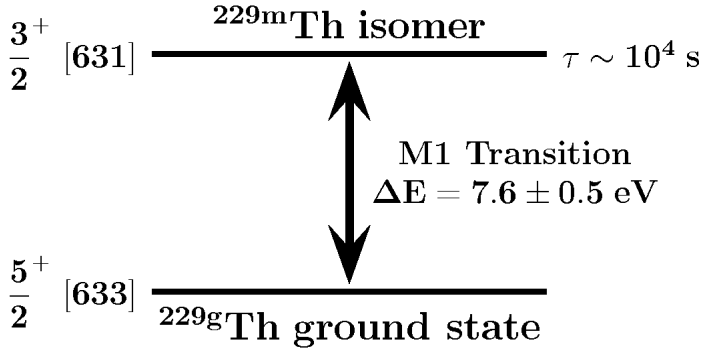

Figure 1: ^{229g}Th $\leftrightarrow$ ^{229m}Th nuclear transition.

al. [33] in 2007. They determined that the ^{229m}Th state lay just 7.6±0.5 eV above the nuclear ground state. This corresponds to a wavelength of 160 ± 11 nm for the ^{229g}Th $\leftrightarrow$ ^{229m}Th transition. By comparison to a similar metastable energy level in the nucleus of ^{233}U, they estimated the radiative lifetime of the ^{229m}Th state to be ~ 5 hr. The ^{229g}Th $\leftrightarrow$ ^{229m}Th transition is depicted in Figure 1. The ^{229g}Th and ^{229m}Th states have nuclear spins of $5/2$ and $3/2$, respectively [29]. They are connected by a magnetic dipole (M1) transition [24].

Direct observation of the nuclear transition via an emitted photon is complicated by the long lifetime of the metastable state. To achieve an emission rate sufficient for detection, it would be preferable to have a large number of confined ^{229}Th atoms available for spectroscopy. However, with large quantities of atoms, mechanisms like Doppler and collisional broadening may reduce the precision of direct measurement or prevent the realization of a significant excited state population. Furthermore, any detection scheme would have to take into account the potential for interaction of the UV photon with the surrounding environment.

An alternative approach of measuring the transition energy via direct excitation of the isomer in a single, laser-cooled thorium atom overcomes the aforementioned difficulties. As was pointed out by Peik and Tamm [24], the lowest charge state of thorium with electronic transitions amenable to laser cooling is Th^{3+}. The Grotrian diagram of Figure 2 is helpful for visualizing the energy states of the combined nuclear/electronic system in

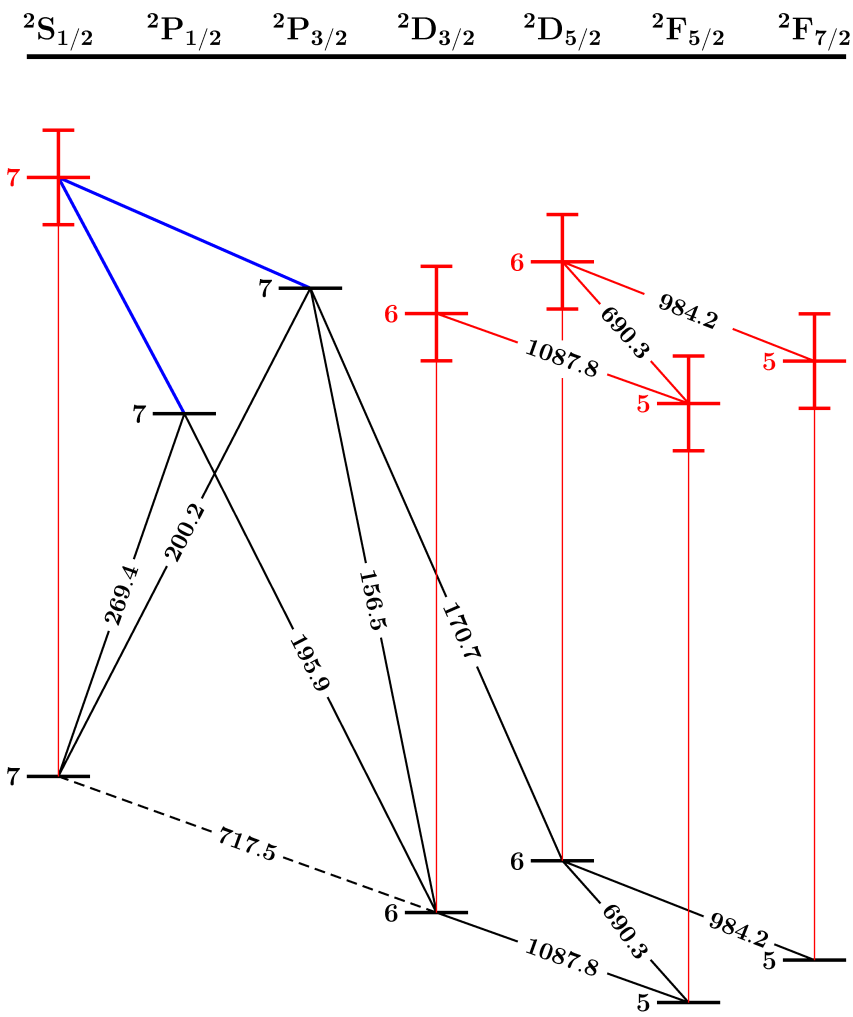

Figure 2: Grotrian diagram of energy states of the combined nuclear/electronic system in $^{229}Th^{3+}$. Energy states represented by black lines correspond to the nuclear ground state, while energy states represented by red lines correspond to the nuclear excited state. Each of the connected black and red states are separated by 7.6 ± 0.5 eV (160 ± 11 nm). Solid black/red lines between states are dipole allowed transitions. The dashed black line is a dipole forbidden transition. Electronic transitions are labeled in units of nm. Values for the transitions between the $5F_{5/2}$, $5F_{7/2}$, $6D_{3/2}$, and $6D_{5/2}$ states are from our measurements of the transitions in $^{232}Th^{3+}$ [35]. Other transition values are from spectroscopy performed by Klinkenberg [36]. The blue lines represent possible electron bridge transitions.

$^{229}Th^{3+}$. The nuclear ground and metastable states manifest themselves as pairs of electronic states with identical n, ℓ, s, and j quantum numbers, separated by the energy of the $^{229g}Th \leftrightarrow {}^{229m}Th$ transition.

The detection of the isomeric excitation is accomplished by observing the fluorescence arising from the laser cooling of the $^{229}Th^{3+}$ ion. The nuclear transition represents a change in the nuclear spin of the atom, and hence, a change in the hyperfine structure of the electronic states. Consider a $^{229}Th^{3+}$ ion in the nuclear ground state being laser cooled by connecting states in the hyperfine manifolds of the $5F_{5/2}$ and $6D_{3/2}$ states shown in Figure 2. Upon excitation of the nuclear isomer, the ion will no longer be resonant with the incident laser, and the fluorescence signal will be lost. If the nucleus is then driven back to the ground state via stimulated emission, the fluorescence signal will return. Alternatively, while the nucleus is still in the isomer state, the cooling laser could be tuned to resonance between two states in the shifted hyperfine manifolds. Either technique would allow 100% detection efficiency of the isomer transition.

Excitation and decay of the metastable nuclear state can occur in several ways. A photon at the wavelength corresponding to the difference in energy between the two states can be absorbed or emitted, allowing for a transition between electronic states with equivalent n, ℓ, s, and j quantum numbers in the $^{229g}Th^{3+}$ and $^{229m}Th^{3+}$ manifolds. Another channel exists between different electronic states of the ground and metastable nuclear states. This is called the *electron bridge* [37, 38]. In this case, a photon with energy equivalent to the difference in absolute energy between the two states is absorbed or emitted. The process is shown in Figure 2. Recent theoretical work [39] suggests that the strongest electron bridge channels are between the $7P_{1/2}$ and $7P_{3/2}$ states of the nuclear ground manifold, and the $7S_{1/2}$ state of the metastable nuclear manifold. The existence of the electron bridge decay channels reduces the lifetime of the nuclear excited state.

It is also possible for the nuclear excited state to decay via an internal conversion process, whereby the energy difference between the ground and metastable nuclear states is

carried away in the form of kinetic energy of an ejected electron. However, this particular decay process is unlikely to occur in Th^{3+} because its ionization energy is 28.8 eV, while the energy of the ^{229g}Th $\leftrightarrow$ ^{229m}Th transition is only $\sim$ 8 eV.

The first suggestion that the isomeric transition in ^{229}Th might be used as an optical clock was made by Peik and Tamm [24]. They pointed out that a measurement of the ^{229g}Th $\leftrightarrow$ ^{229m}Th transition between $m_F = 0$ sublevels of the nuclear ground and isomer $7S_{1/2}$ states in $^{229}Th^{3+}$ would be unaffected by the linear Zeeman effect, linear and quadratic Stark effect, and the quadrupole shift. A similar transition utilizing the $7P_{1/2}$ electronic state would also be unaffected. The extended lifetime of the isomer state combined with the high frequency of the optical transition result in an oscillator quality factor, $\delta\omega/\omega$, of between 10^{19} and 10^{20}.

Laser cooling $^{229}Th^{3+}$ will require precise knowledge of its hyperfine structure. However, the hyperfine structure of the electronic states of $^{229}Th^{3+}$ has never been measured. Precision spectroscopy of the $^{229g}Th^{3+}$ and $^{229m}Th^{3+}$ hyperfine structure would provide a rigorous measurement of the magnetic dipole moments and the electric quadrupole moments of the ^{229}Th nucleus in its ground and metastable states. These values are currently known only approximately [40–42]. Furthermore, a measurement of the change in the nuclear electric quadrupole moment between the ^{229g}Th and ^{229m}Th states would help to determine if the isomeric transition is especially sensitive to variations in the fine structure constant [42].

An additional factor determining the sensitivity of the transition to changes in the fine structure constant is the isomer shift in the center frequencies of the electronic transitions [42]. The isomer shift is due to the deformation of the nucleus that occurs with the ^{229g}Th $\leftrightarrow$ ^{229m}Th transition. The deformation leads to a change in the charge distribution of the nucleus, which in turn shifts the frequencies of the electronic transitions. Differences in the physical structure of the nucleus are partially responsible for the more familiar shift of electronic resonances among different isotopes of an atom [43]. In the case of the

^{229}Th nucleus, the change in nuclear structure between the states represents a change in the Coulomb energy of the nucleus. If this change in Coulomb energy is denoted ΔV_C, the fractional change in the fine structure constant is related to the change in the transition frequency by [42]

$$\frac{\delta\alpha}{\alpha} = \frac{\delta\omega}{\Delta V_C} \tag{1}$$

1.2.2 Progress

We chose to use the ^{232}Th isotope to develop and refine our methods of Th^{3+} ion trapping. This isotope does not possess the low-lying isomer state. However, unlike ^{229}Th, it is relatively inexpensive and easily obtainable. Furthermore, the nuclear spin of ^{232}Th is zero, so the electronic states of $^{232}Th^{3+}$ exhibit no hyperfine structure. This simplifies laser cooling and observation of fluorescence by reducing the number of states involved. Both ^{232}Th and ^{229}Th are radioactive alpha emitters, but the specific activity of ^{232}Th is less than that of ^{229}Th by a factor of $\sim 2,000,000$. Therefore, ^{232}Th presents much less of a radiological hazard.

Our group has developed several different linear RF ion traps for the confinement of Th^{3+}. These traps are loaded with Th^{3+} ions created via laser ablation. Helium buffer gas is used to thermalize the Th^{3+} ions after they are trapped. Diode lasers are used to excite optical transitions between the low-lying electronic states of the trapped $^{232}Th^{3+}$, and the resulting fluorescence is observed with a CCD camera. Using the same optical transitions, our group has demonstrated laser cooling of $^{232}Th^{3+}$ [35].

To date, most of our work with $^{232}Th^{3+}$ has been done with ions ablated from a solid thorium metal target. However, the ^{229}Th isotope is not available in metallic form. This isotope can only be extracted from nuclear reactor sources in the form of a thorium compound. We were able to obtain a sample of ^{229}Th in the form of thorium nitrate ($^{229}Th\,(NO_3)_4$) from Oak Ridge National Laboratory (ORNL).

In our earliest observations of $^{232}Th^{3+}$, the ions would remain in the trap for only a few

seconds. This is in stark contrast to singly-ionized barium, which can remain in an ion trap for long periods ($>$ 1 day). The primary loss mechanisms of Th^{3+} are charge exchange and chemical reactions. With higher purity buffer gas and improved vacuum conditions, we were able to extend the trap lifetime of Th^{3+} to minutes. By removing the buffer gas immediately after the initial trap loading and laser cooling the ions, a lifetime of $\sim$ 11 minutes was obtained [35].

1.3 Contribution of Present Work

Toward the goal of coupling a Ba^+ ion to a high-finesse cavity, a simple and reliable vapor cell was constructed for narrow-line, Doppler-free spectroscopy of neutral barium. This instrument is a critical component in implementing our method of barium photoionization. High resolution Doppler and sub-Doppler spectra were obtained for the $^1S_0 \rightarrow {}^3P_1$ inter-combination line of all isotopes with natural abundance $>$ 1%. The vapor cell, which is typically held at $\gtrsim$ 600°C, is still functional after over a year of continuous use.

Toward the goal of observing the optical nuclear transition in $^{229}Th^{3+}$, a deposition technique for creating ablation targets from trace quantities of thorium nitrate was developed. Thorium nitrate is dissolved in a solvent, and a small droplet of the solution is dried on a metal substrate. Tests of loading from a ^{232}Th nitrate target were performed. Procedures for the safe handling of the ^{229}Th radioisotope were formulated. The ^{229}Th sample from ORNL was put in the form of a solution, and two ^{229}Th ablation targets were made. Additional solutions of ^{232}Th nitrate were produced to establish a lab standard for future tests.

To better understand the charge exchange and chemical reaction processes that limit the trap lifetime of Th^{3+}, a series of experiments was conducted to determine the reaction rate coefficients between $^{232}Th^{3+}$ and various gases. Reactions of Th^{3+} with carbon dioxide, methane, and oxygen were found to occur near the classical Langevin rate limit, while reaction rates with argon, hydrogen, and nitrogen were found to be orders of magnitude lower. Loss rates of Th^{3+} in helium and neon gases are consistent with reaction with impurities in

the respective gases. The data establishes a standard for determining the purity of helium buffer gas and the quality of the background vacuum in the ion trap system. This standard has already been applied in the analysis of existing vacuum apparatus and in developing strategies for future apparatus.

1.4 Organization of Thesis

The remainder of the thesis is divided into five chapters. Chapter 2 provides an introduction to the theory and operation of linear RF ion traps. Chapter 3 provides an overview of the barium ion trapping experiment, with a particular focus on the vapor cell that was developed for neutral barium spectroscopy. Chapter 4 discusses the experimental apparatus and techniques used in trapping triply-ionized thorium. This chapter also includes a description of the technique for producing ablation targets from thorium nitrate solution. Chapter 5 discusses the experimental program for determining the reaction rate coefficients between Th^{3+} and various gases. The thesis concludes with Chapter 6, which summarizes the results presented and provides an outlook for the future of the experiments.

CHAPTER II

LINEAR RADIO-FREQUENCY ION TRAPS

There are a many types of apparatus designed for the confinement of charged particles. We limit our discussion here to the specific type of instrument relevant to this thesis, the linear Paul trap, or equivalently, the linear RF trap. As the latter name implies, these traps utilize dynamic fields to create their confining potential. They are further characterized by their relatively large trap depths and their ability to selectively confine ions according to their mass-to-charge ratio. More will be said on these attributes in Section 2.1.2 and Section 2.3.

The linear Paul trap was first proposed by Prestage, et al. in [44]. Central to their design was the linear RF ion guide, invented by Wolfgang Paul in 1953 [45]. The linear RF ion guide utilizes oscillating quadrupole fields to constrain the motion of ions in two dimensions, thereby guiding them as they move freely in the third, axial dimension. With the addition of a DC field and judicious choices of the amplitude and frequency of oscillation, the ion guide can selectively constrain ions according to their mass-to-charge ratios, making it an effective mass filter. Commercial mass spectrometers and residual gas analyzers commonly employ linear ion guides as mass filters to perform their measurements.

To make the linear RF ion guide into a three-dimensional trap, Prestage and his colleagues added to each end of the ion guide a small electrode on its axis. To these electrodes, they applied a positive DC bias. The combination of the oscillating field of the ion guide with the DC field of the new electrodes created a three-dimensional trap for positive ions. The group went on to use their trap to perform some of the original work in the mercury ion frequency standard [46].

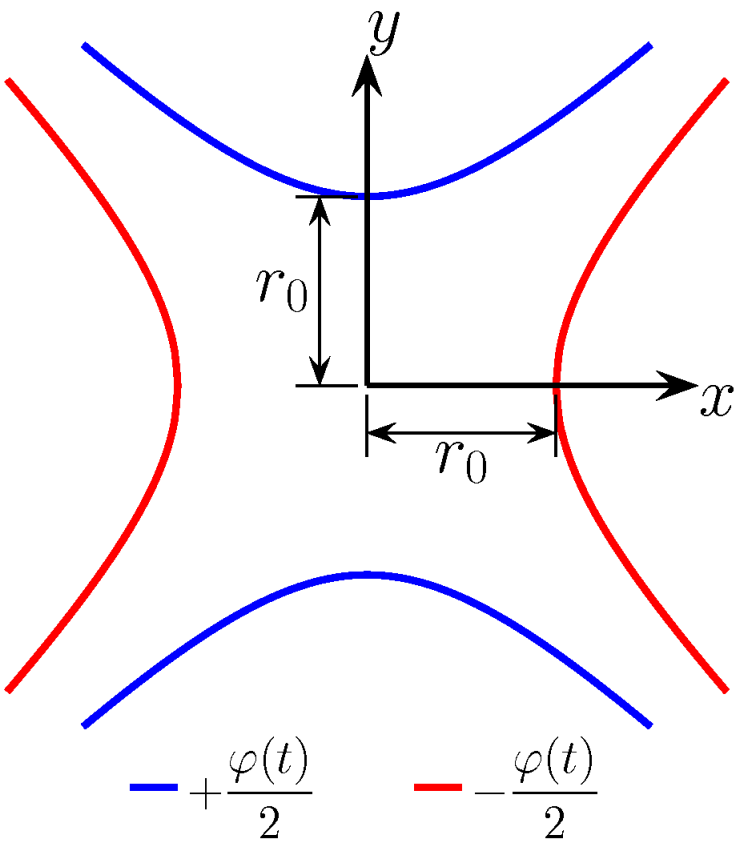

Figure 3: The cross-section of an ideal linear Paul trap. The distance between the center of the trap and the nearest point on any electrode is r_0, and the electrodes are assumed to be infinitely long in the axial z-dimension.

The remainder of this chapter is devoted to more thoroughly describing the characteristics of the linear Paul trap. A mathematical description of the trapping fields is developed, and this theoretical formulation is subsequently analyzed with respect to physically realized ion traps. The chapter concludes with a discussion of the mass-selective characteristics of the linear Paul trap.

2.1 Formulation

The cross-section of an ideal linear Paul trap is shown in Figure 3. The electrodes of an ideal linear Paul trap are assumed to extend to positive and negative infinity in the z-dimension while maintaining this cross-section.

The red and blue lines in Figure 3 represent the equipotential surfaces of the trap electrodes. These lines are defined by the hyperbolic equations

$$\pm\frac{y^2 - x^2}{r_0^2} = 1, \tag{2}$$

and the electrodes they represent carry voltages $\pm\varphi(t)/2$. Here the top and bottom signs correspond to the blue and red lines, respectively. The electrical potential in the region between the electrodes, $\Phi(\mathbf{r}, t)$, must be a solution to Laplace's equation ($\nabla^2\Phi = 0$) and must satisfy the boundary conditions on the electrode surfaces. Clearly,

$$\Phi(\mathbf{r}, t) = \varphi(t)\,\frac{y^2 - x^2}{2r_0^2}. \tag{3}$$

fulfills both requirements. This is the potential of an electric quadrupole; hence another common moniker for this style of system, the quadrupole trap.

The potential $\Phi(\mathbf{r}, t)$ is plotted in Figure 4. For obvious reasons, the electric potential $\Phi(\mathbf{r}, t)$ is called a *saddle potential*. This is a specific manifestation of Earnshaw's theorem, which states that electrostatic potentials cannot have local minima or maxima in freespace [47]. The immediate corollary to Earnshaw's theorem is that a charged particle can not be held in stable equilibrium by electrostatic forces alone. Consider Figure 4 again. It is clear that for the case $\varphi(t) > 0$, a positively-charged particle would be bound in the y-dimension but not in the x-dimension. On the other hand, if $\varphi(t) < 0$, the positively-charged particle would be bound in the x-dimension but not in the y-dimension.

Now consider an oscillating potential, $\varphi(t) = V_{\mathrm{rf}} \cos\Omega t$. As $\varphi(t)$ oscillates between positive and negative values, the confining dimension oscillates between x and y. We shall see that for certain values of V_{rf} and Ω such an oscillation can ultimately produce a confining *pseudo*-potential in both dimensions.

We will generalize the expression for the applied voltage by adding a DC offset: $\varphi(t) = U_{\mathrm{dc}} - V_{\mathrm{rf}} \cos\Omega t$. The equations of motion for a particle with charge Ze in the resulting

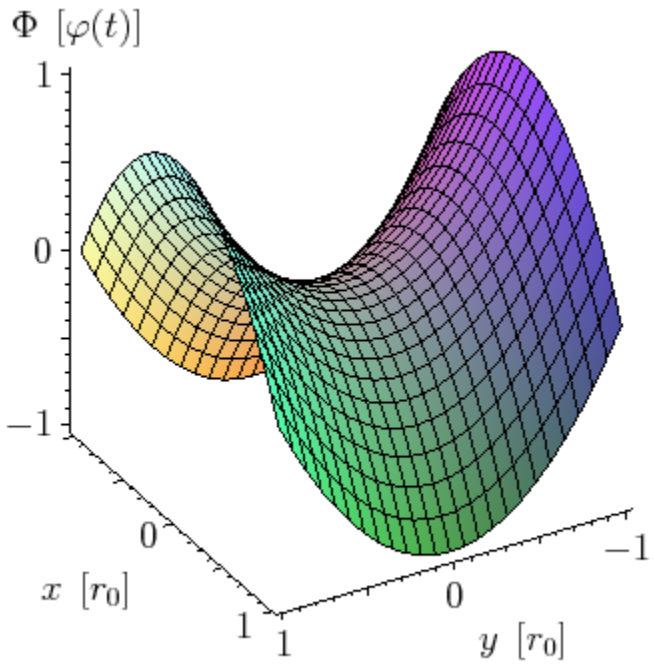

Figure 4: The saddle potential of an electric quadrupole. The electric potential is given by $\Phi(\mathbf{r}, t) = \varphi(t)\,\frac{y^2-x^2}{r_0^2}$.

electric potential are[1]

$$m\ddot{x} = \frac{Ze}{r_0^2}\,(U_{\mathrm{dc}} - V_{\mathrm{rf}}\cos\Omega t)\,x \tag{4}$$

$$m\ddot{y} = -\frac{Ze}{r_0^2}\,(U_{\mathrm{dc}} - V_{\mathrm{rf}}\cos\Omega t)\,y. \tag{5}$$

Making the substitutions

$$q = \frac{2ZeV_{\mathrm{rf}}}{mr_0^2\Omega^2} \tag{6}$$

$$a = \frac{4ZeU_{\mathrm{dc}}}{mr_0^2\Omega^2} \tag{7}$$

$$\zeta = \frac{\Omega t}{2}, \tag{8}$$

[1] Here we use the formula $m\ddot{x}_i = -Ze\nabla_i\Phi(\mathbf{r}, t)$.

we can rewrite the equations of motion as

$$\frac{d^2x}{d\zeta^2} + (a_x - 2q_x \cos 2\zeta)x = 0 \tag{9}$$

$$\frac{d^2y}{d\zeta^2} + (a_y - 2q_y \cos 2\zeta)y = 0, \tag{10}$$

with $q_y = -q_x = q$ and $a_y = -a_x = a$. Note that q_y and a_y have the same signs as q and a given in Eqs. 6 and 7, while q_x and a_x have the opposite signs.

Our interest is in trapped particles, so we seek solutions to the equations of motion such that both x and y remain finite for all time. Compare the equations of motion in Eq. (9) and Eq. (10) with the canonical Mathieu equation:

$$\frac{d^2u}{d\zeta^2} + (a - 2q \cos 2\zeta)\, u = 0. \tag{11}$$

Stable solutions[2] to the Mathieu equation can be found for specific values of q and a. For this reason, q and a are known as the *stability parameters* [48]. Note that due to the periodicity of Eq. (11), if a solution is stable for (q, a), it must also be stable for $(-q, a)$. Thus, with regards to the discussion of stable solutions, we can neglect the sign difference between q_x and q_y and consider only the value of q.

Figure 5 shows regions within qa-space where stable solutions to the Mathieu equation exist. Given its direct correspondence with the Mathieu equation, the equation of motion in y (Eq. (10)) also yields stable solutions in these regions. The difference in sign between a_x and a_y suggests that the regions of stability for the equation of motion in the x-dimension (Eq. (9)) can be obtained by inverting the graph about the q-axis. This is shown in Figure 6. The regions where the two graphs overlap are where stable solutions to both equations of motion can be found. Thus, with an appropriate choice of parameters, confinement in both dimensions can be obtained. More will be said on the nature of this confinement in Section 2.1.2.

[2]That is, solutions such that $u(\zeta) \nrightarrow \infty$ as $\zeta \to \infty$.

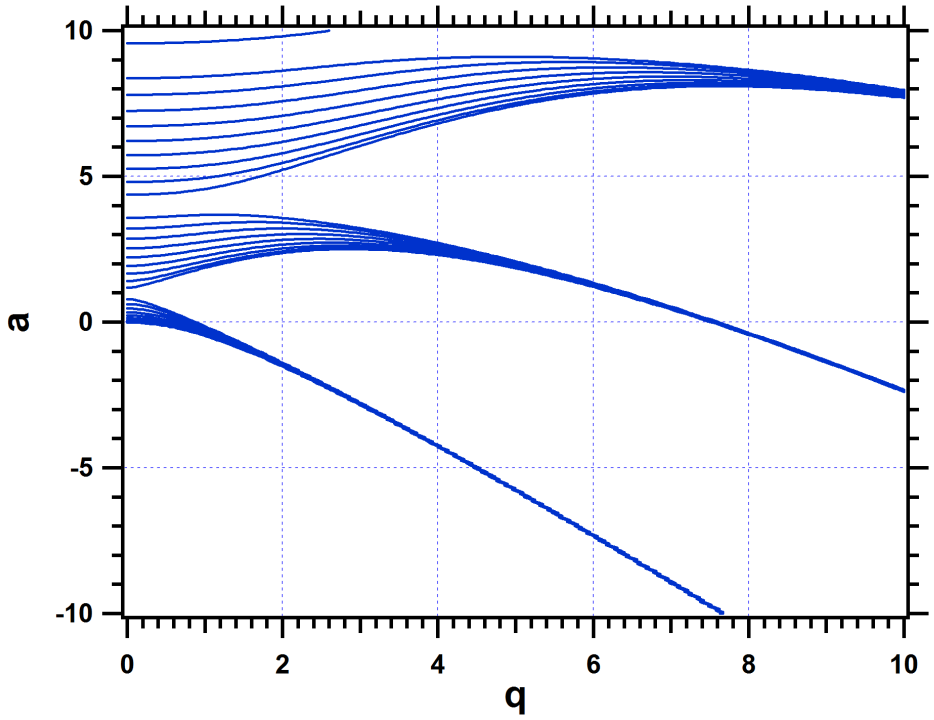

Figure 5: The stability regions for the canonical Mathieu equation.

2.1.1 Plotting the Stability Regions of the Mathieu Equation

It is instructive to briefly consider how one may obtain an accurate plot of the regions of stability of the Mathieu equation (Eq. (11)). Following the examples of [49] and [50], we consider two linearly independent solutions of the Mathieu equation, $u_1(\zeta; q, a)$ and $u_2(\zeta; q, a)$, with initial values

$$\begin{aligned} u_1(0; q, a) &= 1 \qquad u_2(0; q, a) = 0 \\ u_1'(0; q, a) &= 0 \qquad u_2'(0; q, a) = 1 \end{aligned} \tag{12}$$

Note that the specific form of each of the solutions, u_1 and u_2, depends on the stability parameters, q and a. For the sake of readability, we will omit the explicit reference to the stability parameters in the functions u_1, u_2, and their derivatives in what follows.

Recalling that u represents one of the cartesian coordinates x or y, we note that any solution to the Mathieu equation with initial conditions $u(0) = x_0$ and $u'(0) = v_0$ can be

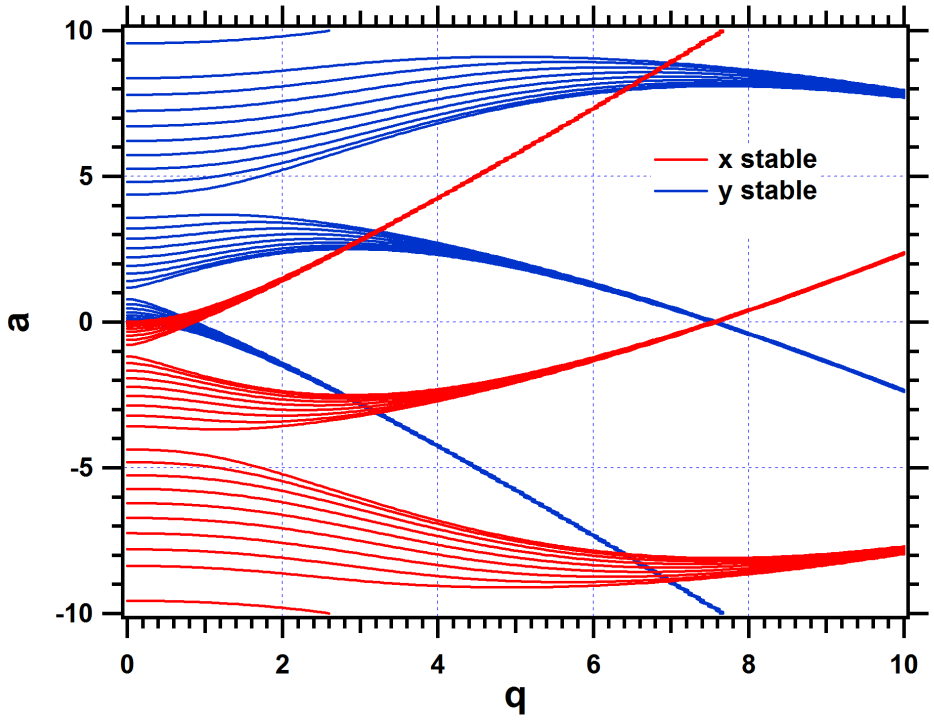

Figure 6: The stability regions for the x and y equations of motion. The regions of stability for the y equation of motion are the same as those in Figure 5, while the regions of stability for the x equation of motion are obtained by inverting the graph of Figure 5 about the q-axis. This inversion is due to the difference in sign between a_x and a_y in the equations of motion.

written as a linear combination of u_1 and u_2:

$$u(\zeta) = x_0 u_1(\zeta) + v_0 u_2(\zeta)\,. \tag{13}$$

Although Eq. (13) is valid for all ζ, when considering ion stability we ignore the fast evolution due to the RF drive, and consider only motion over integral numbers of RF cycles. That is, we ignore the ion's *micromotion*, and consider only its *secular motion* [51]. These concepts will be discussed in greater extent in Section 2.1.2.

After a single RF cycle, we have

$$\begin{aligned} u(\pi) &= x_0 u_1(\pi) + v_0 u_2(\pi) = x_1 \\ u'(\pi) &= x_0 u_1'(\pi) + v_0 u_2'(\pi) = v_1 \end{aligned} \tag{14}$$

This can be rewritten in matrix form as

$$\begin{pmatrix} x_1 \\ v_1 \end{pmatrix} = \boldsymbol{\mathcal{M}} \begin{pmatrix} x_0 \\ v_0 \end{pmatrix}, \tag{15}$$

where we have defined the *transfer matrix*,

$$\boldsymbol{\mathcal{M}} \equiv \begin{bmatrix} u_1(\pi) & u_2(\pi) \\ u_1'(\pi) & u_2'(\pi) \end{bmatrix}. \tag{16}$$

Of course, to compute the position and velocity of an ion after n cycles, one would use Eq. (15) with x_0 and v_0 equal to the position and velocity after $n-1$ cycles. Equivalently, one may write

$$\begin{pmatrix} x_n \\ v_n \end{pmatrix} = \boldsymbol{\mathcal{M}}^n \begin{pmatrix} x_0 \\ v_0 \end{pmatrix}. \tag{17}$$

The transfer matrix is a real matrix with $\det(\boldsymbol{\mathcal{M}}) = 1$. Its eigenvalues are easily calculated:

$$\lambda_\pm = s \pm \imath \sqrt{1 - s^2}, \qquad s = \frac{1}{2}\left[u_1(\pi) + u_2'(\pi)\right]. \tag{18}$$

The initial position and velocity of the ion can be written in terms of the corresponding eigenfunctions, $m_\pm$. To wit,

$$\begin{pmatrix} x_0 \\ v_0 \end{pmatrix} = C_+ m_+ + C_- m_-. \tag{19}$$

Substituting this expression into Eq. (17),

$$\begin{aligned}\begin{pmatrix} x_n \\ v_n \end{pmatrix} &= \boldsymbol{\mathcal{M}}^n \left[C_+ m_+ + C_- m_-\right] \\ &= C_+ \boldsymbol{\mathcal{M}}^n m_+ + C_- \boldsymbol{\mathcal{M}}^n m_- \\ &= C_+ \lambda_+^n m_+ + C_- \lambda_-^n m_-. \end{aligned} \tag{20}$$

Clearly, for the motion to remain bounded, we require $|\lambda_\pm| \leq 1$. Recalling Eq. (18), we can see that this requirement is met when $|s| \leq 1$, or equivalently,

$$\left|u_1(\pi) + u_2'(\pi)\right| \leq 2. \tag{21}$$

Thus, to determine whether a given position in qa-space is stable, one needs only to evaluate the eigenfunction u_1 and the eigenfunction derivative, u_2', after a single RF cycle. A method for numerically evaluating these functions after a period of the RF is discussed in [49]. Alternatively, one may obtain the numerical solutions to the functions from advanced mathematical software such as Maple 11 [52]. The u_1 and u_2' functions are featured in Maple 11 as *MathieuC* and *MathieuSPrime*, respectively. These functions can be called in C programs via the OpenMaple interface. Programs utilizing OpenMaple and these functions to produce graphs of the regions of stability of the Mathieu equations can be found in Appendix B. These programs were used to produce the stability diagrams featured in this thesis.

The lowest region of common stability for the x and y equations of motion is shown in Figure 7. This region is the most experimentally utilized since the voltages necessary to occupy it are the lowest for any given trap radius and drive frequency. The experiments described in this thesis specifically utilized this region of qa-space. The region is symmetric about the q-axis, so only the positive a-axis is shown. Due to this symmetry, the sign difference between a_x and a_y is commonly ignored, though we note it explicitly on this graph.

There is not a simple analytic expression for the boundaries of the stability region shown

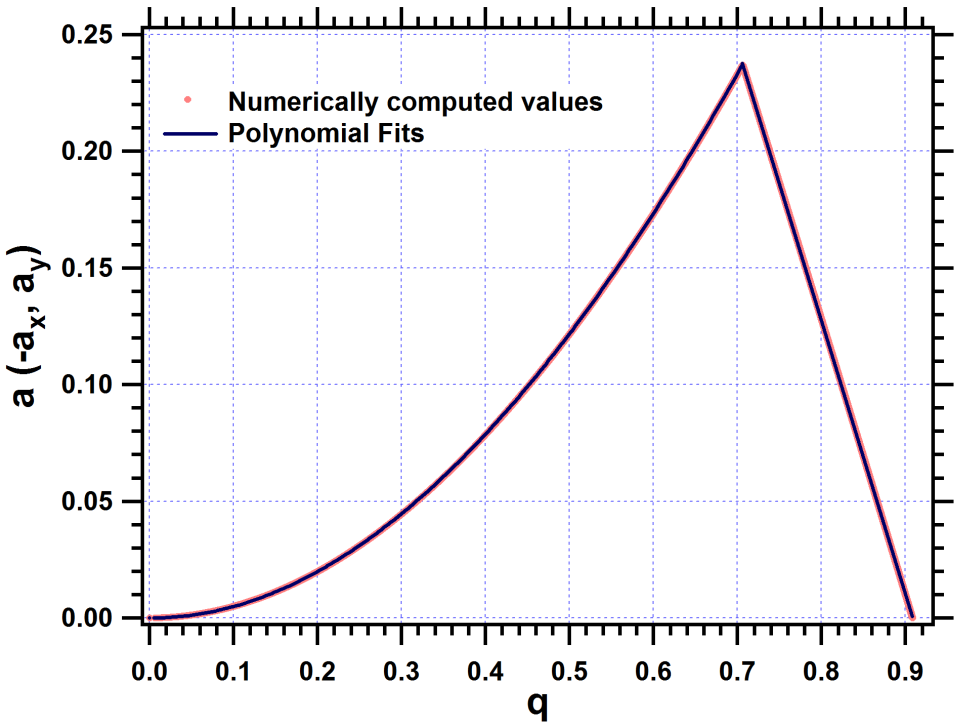

Figure 7: The lowest region of common stability. The region bounded by the solid line and the q-axis allows stable solutions to both the x and y equations of motion. Numerical values for the boundary were computed using the programs in Appendix B. The expressions for the polynomial fits and the values of the coefficients can be found in Table 1.

Table 1: The fit coefficients for the stability diagram. The standard deviations for the fit coefficients are all less than one in the least significant digit given. The curves defining the boundary of the region of stability shown in Figure 7 are given by $\sum_{n=0}^{3} A_n q^n$ in the range $0 \leq q \leq 0.706$ and $B_0 + B_1 q$ in the range $0.706 \leq q \leq 0.908$.

Coefficient	Fit Value
A_0	0.0
A_1	-3.23×10^{-3}
A_2	0.5256
A_3	-6.43×10^{-2}
B_0	1.0657
B_1	-1.173

in Figure 7. However, simple polynomial fits are sufficient to accurately reproduce the curves. This removes any need to repeat the numerical computations, which can be very time-consuming. The coefficients of the fits shown in Figure 7 are given in Table 1. The intersection of the two boundaries forming the apex of the stable region occurs approximately at the point $(q, a) = (0.706, 0.237)$. The region extends from $q = 0$ to $q \approx 0.908$.

2.1.2 Ion Motion and Pseudo-Potential

At any single instant in time, an ion subject to the potential given in Eq. (3) experiences a force that is directed toward the origin in one dimension and away from the origin in the other dimension. We know from the earlier discussion, however, that it is possible to confine an ion in such a potential. What ultimately determines whether an ion will be trapped is the *time-average* of the forces it experiences. If the time-averaged force on the ion is directed toward the origin in all dimensions, the ion will be trapped. The time-averaged force can be defined as the gradient of a scalar *pseudo*-potential. In this section, we derive an expression for this confining pseudo-potential and use it to gain more insight into the linear Paul trap.

We begin by separating the ion motion into a slow, large-amplitude *secular motion* and

a fast, small-amplitude *micromotion* [51]. For example, in the x-dimension:

$$x = X + \delta_x. \tag{22}$$

Here, X is the amplitude of the secular motion in the x-dimension, and δ_x is the amplitude of the micromotion in this dimension. Our assumptions about the secular and micromotion imply

$$(i) \quad X \gg \delta_x \qquad (ii) \quad \frac{d\delta_x}{d\zeta} \gg \frac{dX}{d\zeta}. \tag{23}$$

Substituting the expression for x into the equation of motion for x (Eq. (9)) and using the preceding assumptions,

$$\frac{d^2\delta_x}{d\zeta^2} = -\left(a_x - 2q\cos 2\zeta\right) X. \tag{24}$$

If X does not vary significantly over a single RF cycle, and if $|a_x| \ll |q|$,[3] we can integrate this to give

$$\delta_x = \frac{qX}{2}\cos 2\zeta. \tag{25}$$

Note that the micromotion occurs at the fundamental frequency of the trap, and its amplitude is linearly related to the instantaneous secular amplitude. It is also proportional to the RF amplitude through the factor q. The time-average of the micromotion over an RF cycle is zero.

Now we consider the secular motion. Plugging the expression for the micromotion into Eq. (22) and then into the equation of motion for x (Eq. (9)),

$$\frac{d^2}{d\zeta^2}\left(X + \delta_x\right) = -\left[a_x + \frac{qa_x}{2}\cos 2\zeta - 2q\cos 2\zeta - q^2\cos^2 2\zeta\right] X. \tag{26}$$

The amplitude of the secular motion is considered approximately constant over a single RF cycle; therefore, we can simplify the above equation by averaging over an RF cycle. This eliminates the micromotion and cosine terms leaving

$$\frac{d^2X}{dt^2} = -\left[a_x + \frac{q^2}{2}\right]\frac{\Omega^2}{4}X. \tag{27}$$

[3]It is clear from Figure 6 that this inequality does not hold in all regions of common stability between x and y. However, it does hold in the region nearest the origin of the qa-space, which is the region of primary importance here.

Here we have substituted for ζ using Eq. (8). Eq. (27) is the equation of motion for a harmonic oscillator with frequency

$$\omega_x = \left[a_x + \frac{q^2}{2}\right]^{1/2} \frac{\Omega}{2}. \tag{28}$$

Note that, in light of the preceding equation, the difference in sign between a_x and a_y results in different secular frequencies in the two dimensions when a DC field is present. In [53], the different resonances were used to detect and ultimately eliminate a stray field in the trapping region.

Now that we have established that the secular motion of the trapped ion is that of a harmonic oscillator, we can write the confining pseudo-potential[4] in terms of the secular frequencies in the x and y dimensions:

$$\varphi_{\text{eff}}(\mathbf{r}) = \frac{1}{2} m\omega_x^2 x^2 + \frac{1}{2} m\omega_y^2 y^2. \tag{29}$$

The maximum trap depth in either dimension can be obtained by substituting the trap radius, r_0, for the appropriate spatial coordinate. For the case $a_y = -a_x = 0$, the trap depth is

$$\varphi_{\text{eff}}(r_0) = \frac{1}{16} m q^2 r_0^2 \Omega^2 \tag{30}$$

The trap depth for ^{232}Th in a trap of radius $r_0 = 4.13\,\text{mm}$ operating at $\Omega = 2\pi \times 2.04\,\text{MHz}$ as a function of q is shown in Figure 8.

We see from Figure 8 that an ion trap can have a depth of hundreds of electronvolts, or hundreds of thousands of degrees Kelvin. This is enormous compared to the depths of neutral atom traps, which are typically on the order of just a few mK. To put the magnitude of this trap depth in further context, consider the energy of an ion created in an ablation plasma. In [54], laser ablation of metal targets with the third harmonic of an Nd:YAG laser produced ions traveling between $10 - 30\,\text{km/s}$. Our own measurement of the speed of ablated thorium ions yielded a result of $12\,\text{km/s}$ [55]. This corresponds to a kinetic energy

[4]We choose here to represent the pseudo-potential as a function of potential energy, not as an electrical potential. The equivalent electric potential can be obtained by dividing by the elementary charge.

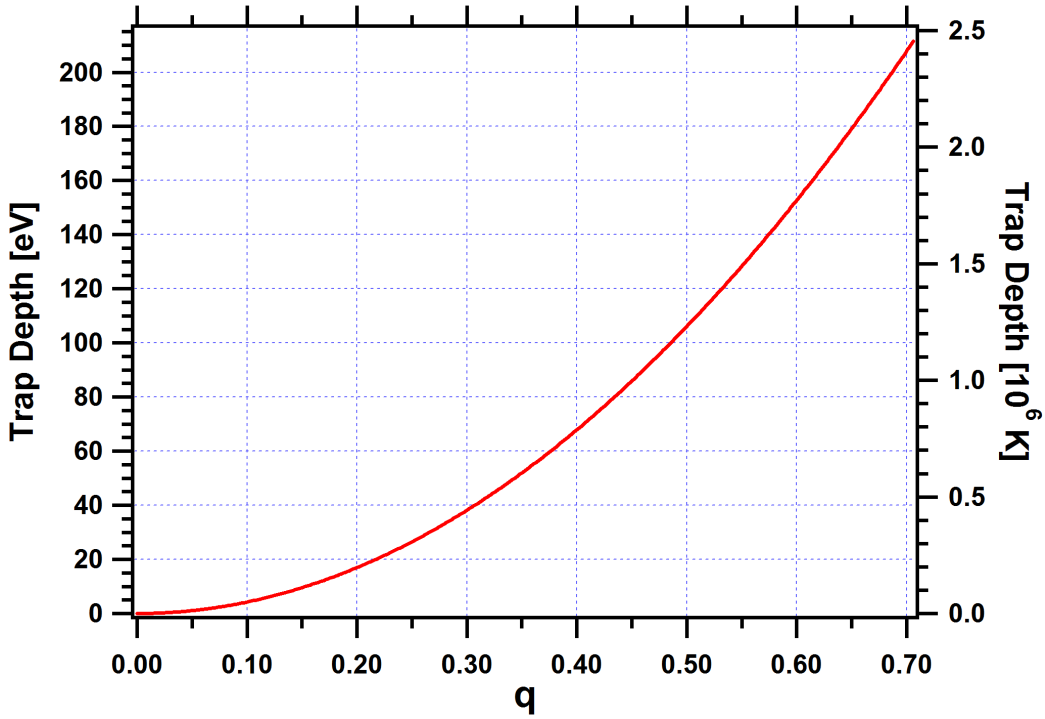

Figure 8: ^{232}Th trap depth as a function of q. The trap has radius $r_0 = 4.13\,\text{mm}$ and operates at frequency $\Omega = 2\pi \times 2.04\,\text{MHz}$.

greater than 100 eV. Without this extraordinary trap depth, trapping significant quantities of ablated ions might not be possible.

In the preceding discussion, we found that the micromotion of the ion occurs at the RF drive frequency, while the frequency of the secular motion is given by the expression in Eq. (28). However, the accuracy of these results is limited by the approximations used to obtain Eq. (24) and Eq. (25). The ion motion is actually made up of an infinite series of frequency components. An exact expression for all of the frequency components that contribute to the motion of the ion can be obtained by considering the analytical solution to the Mathieu equation as in [48]. Generally, the frequency components are given by

$$\omega_n = (2n \pm \beta)\,\frac{\Omega}{2}, \tag{31}$$

with the fundamental secular frequency being $\omega_0 = \beta\Omega/2$. The value of the parameter β, itself sometimes called *the stability parameter* [56], depends on the stability parameters q and a. It is related to the diagonal components of the transfer matrix (Eq. (16)) by the

expression [49]

$$\cos(\pi\beta) = \frac{1}{2}\left[u_1(\pi) + u_2'(\pi)\right]. \tag{32}$$

This relationship allows β to be calculated for any given values of q and a using the Maple 11 functions *MathieuC* and *MathieuSPrime* discussed in Section 2.1.1. Programs utilizing these functions to compute β are given in the appendix.

The stability diagram can be defined in terms of β. The lowest stability region in qa-space is bounded by the lines $\beta = 0$ and $\beta = 1$. At any point on a line of constant β, the ion motion is comprised of the same frequency components, though the amplitude of each component depends on the specific values of q and a.

2.1.3 Axial Confinement

For the linear Paul trap, confinement along the z-axis is most commonly accomplished by a DC field. There are a variety of electrode configurations that can be used to produce such a field. Several examples are shown in Figure 9. The electrode configurations labeled (b) and (e) were each used in the design of traps for the work presented in this thesis. In both cases, the confining field is created between a set of electrodes with an applied DC bias. In the case of configuration Figure 9(b), the electrodes are hollow tubes that slip over the RF trap rods. The tubes are electrically isolated from the trap rods with a suitable insulator such as polyimide [57].

Electrode configuration Figure 9(e) utilizes endcaps in the form of electrostatic lenses, which can focus ions as they pass through their apertures. This style of endcap is especially suitable for experiments requiring injection of ions from an external source or ejection of ions into detection electronics [58–61]. This type of endcap can also be used to facilitate transfer of ions from one linear ion trap to another. The apertures in the endcaps can serve to limit conductance between the various trapping regions, allowing each to be held at a different vacuum pressure. Such a system allows ions loaded in a region of high ambient pressure (say, from an electrospray ionization source) to be quickly moved to a region of

better vacuum [62, 63].

An example of the axial electric potential created by a set of DC electrodes in the form of Figure 9(e) is shown in Figure 10. The dimensions of the trap in this example are taken from a trap that will be discussed in Chapter 4. The trap rods are 37 mm long and 3/8″ (9.53 mm) in diameter. The trap radius is $r_0 = 4.13$ mm. The endcaps are 3/8″ wide and 25 mm in diameter. Each endcap has an aperture 6.25 mm in diameter in its center. The rods and endcaps are separated by insulating washers 1/32″ (0.79 mm) in width.

The electric potential in Figure 10 was calculated using Simion 8.0 [68]. Simion is a software package that uses finite element analysis to solve for electrostatic fields in two and three-dimensions. Simion can also calculate the trajectories of charged particles in these fields. A robust programming interface allows Simion to simulate dynamic fields and particle interaction. In [69], Simion was used to simulate ion motion in a three-dimensional Paul trap. Ion interaction with background gas, external ion injection, dc ejection from the trap, and resonance ejection were also simulated in this work. Other references to Simion in ion trap literature can be found in [66, 70, 71].

To lowest order, the potential on the axis near the center of the trap due to the DC field is harmonic:

$$\varphi_{\text{axial}}(z) = \frac{1}{2} m\omega_z^2 z^2. \tag{33}$$

This can be seen in Figure 11, which shows an enlarged view of the potential of Figure 10 near the center of the trap. The axial secular frequency obeys the relation [64, 72]

$$\omega_z = \sqrt{-2a_{\text{end}}}\frac{\Omega}{2}, \qquad a_{\text{end}} = \frac{4Ze\kappa U_{\text{end}}}{mr_0^2\Omega^2}. \tag{34}$$

Here, U_{end} is the voltage applied to the endcaps, and κ is a dimensionless constant that depends on the geometry of the system. Note that for ω_z to be real, a_{end} must be negative. Thus, κ must also be negative, since Z and U_{end} must have the same sign to create a confining potential.

The validity of Eq. (33) and Eq. (34) can be demonstrated using Simion 8.0. For the

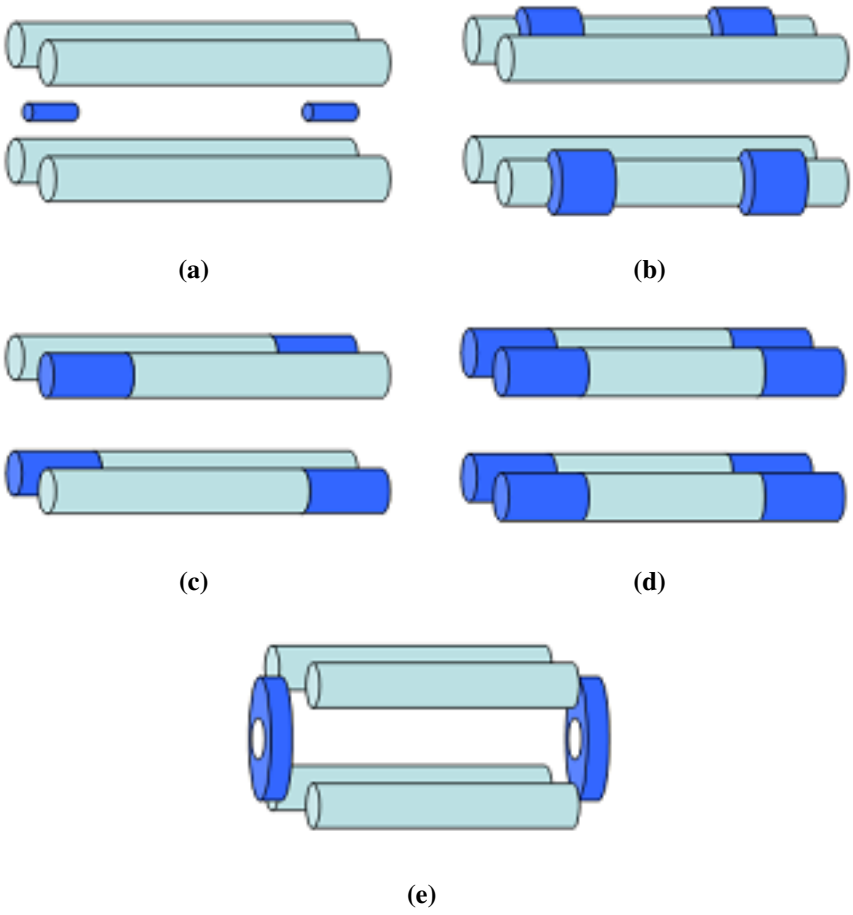

Figure 9: Endcap configurations for axial confinement. In each example, a DC bias is placed on the dark colored electrodes to provide axial confinement. A positive (negative) DC bias allows for confinement of positive (negative) ions. (a) Endcap electrodes are located on the trap axis. The first experimentally realized linear Paul trap utilized this configuration [44]. (b) Hollow tubes are fit around the trap rods with a suitable insulator between them. This method was used in this work and in [57]. (c) Here, the trap rods are made of multiple electrically isolated segments. The RF drive is applied to all rod segments; an additional DC bias is applied to the dark colored segments [64]. (d) Similar to (c). Examples in literature include [53, 65–67]. (e) The lens style electrodes shown here are commonly used if the ions to be confined are created outside of the trapping region or if trapped ions are to be axially ejected to electronic detectors. This electrode configuration was also used in this work, and in [58–63].

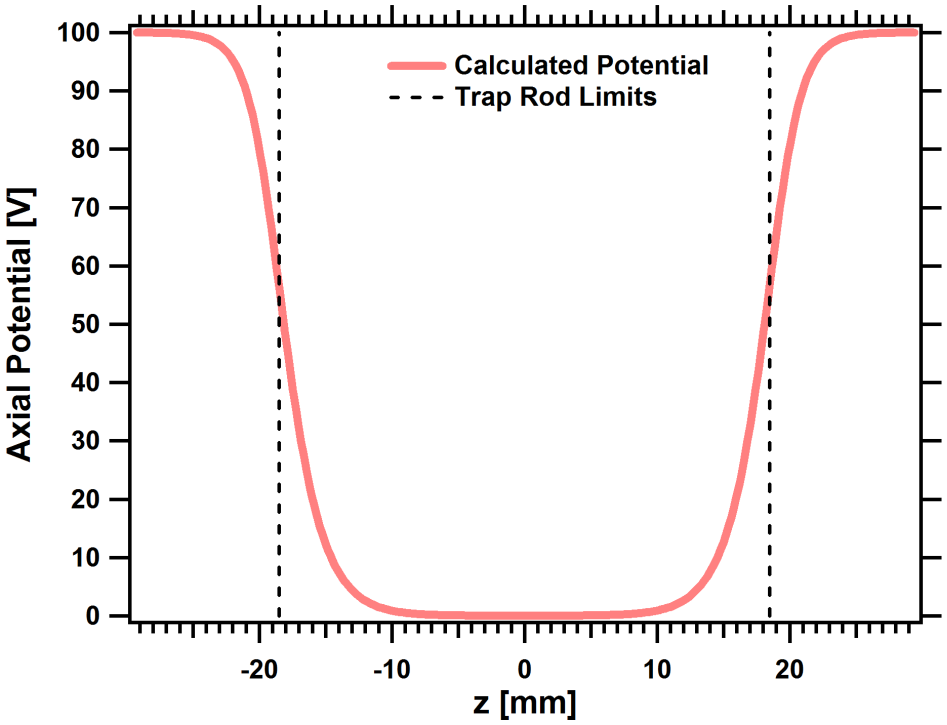

Figure 10: Axial potential of a linear ion trap. The configuration of the trap is shown in Figure 9(e). The trap rods are 37 mm long and 3/8″ (9.53 mm) in diameter. The trap radius is r_0 = 4.13 mm. There is a 1/32″ (0.79 mm). The endcaps are 3/8″ (9.53 mm) wide and 25 mm in diameter. Each has an aperture 6.25 mm in diameter. The endcaps are held at 100 V. The potential was calculated using Simion 8.0 [68].

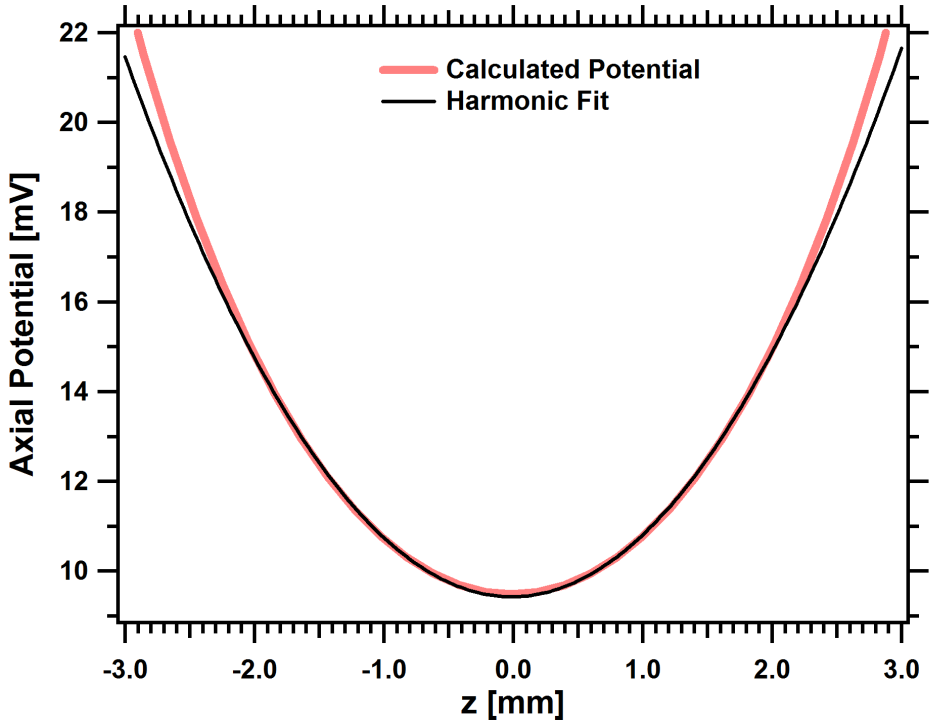

Figure 11: Axial potential near the trap center. Trap parameters and dimensions here are the same as in Figure 10. The potential is approximately harmonic in the center.

trap described earlier in this section (also of Figures 10 and 11), the axial potential was calculated for a number of different values of the endcap bias. The center region, $-2\,\text{mm} \leq z \leq 2\,\text{mm}$, of each calculated potential was subsequently fit to a harmonic potential in the form of Eq. (33), and the axial secular frequency for $^{232}\text{Th}^{3+}$ was determined. These frequencies were plotted and shown to obey the relation $\omega_z \propto \sqrt{U_{\text{end}}}$ implied by Eq. (34). The geometric constant κ was determined from a corresponding fit. This same procedure was carried out on a series of traps scaled either lengthwise or radially from the original. The results are shown in Figures 12 and 13.

One inherent limitation to the use of a DC field for axial confinement is that ions of different polarities cannot be trapped simultaneously. One way to overcome this limitation in linear traps is to apply RF voltages to the endcap electrodes. In [73], interactions between cations and anions were studied by modifying a commercial linear quadrupole mass spectrometer so an RF potential could be applied directly to the endcap electrodes. The

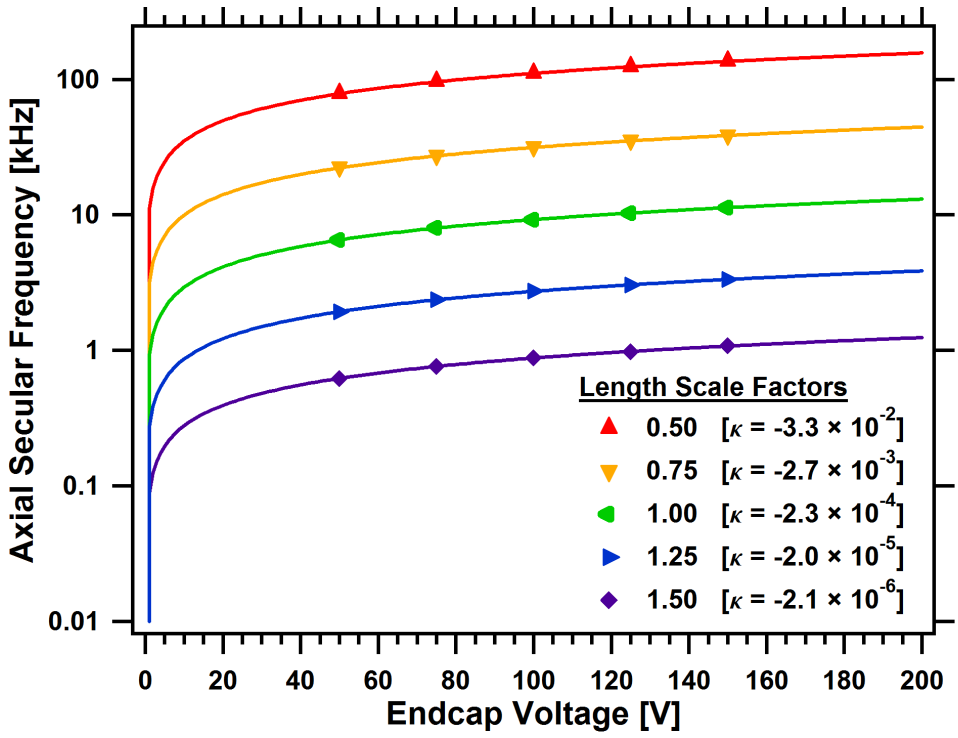

Figure 12: Axial secular frequencies of $^{232}Th^{3+}$ vs. endcap voltage for various trap lengths. Each trap is scaled lengthwise from the original trap described in Figure 10 according to the given scale factor. The fits shown are of the form of Eq. (34).

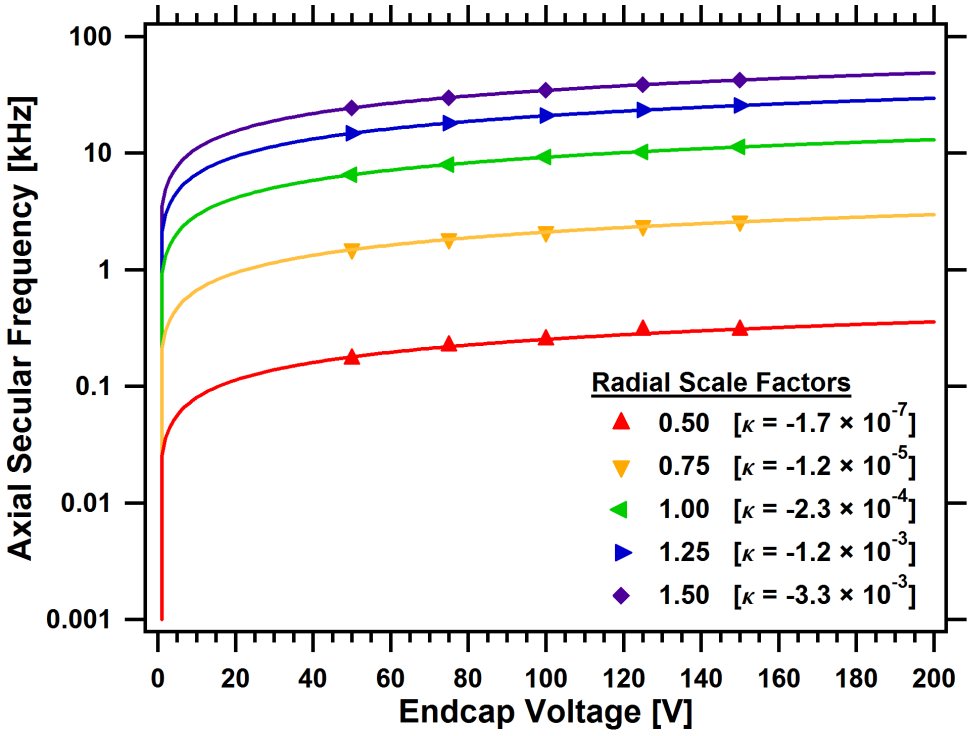

Figure 13: Axial secular frequencies of $^{232}Th^{3+}$ vs. endcap voltage for various trap radii. Each trap is scaled radially from the original trap described in Figure 10 according to the given scale factor. The fits shown are of the form of Eq. (34).

same effect can be accomplished by unbalancing the amplitude of the RF voltage on the trapping rods [74]. This creates an effective RF potential on the endcap electrodes.

2.2 The Physically Realized Ion Trap

In the preceding sections, we developed the basic theory underlying the operation of the linear Paul trap. This section is devoted to comparing the theoretical model to the physically realized trap.

One of the most common and fundamental differences between a real linear Paul trap and the theoretical ideal is the shape of the electrodes. We originally formulated the equations of motion in the x and y dimensions by considering hyperbolic electrodes, but due to the cost and complexity of machining hyperbolic electrodes, most real ion traps are built using cylindrical rods, which are relatively inexpensive and easy to machine to high precision. Typically, the trap rods will all have the same radius, and they will be placed so that their centers lie on the corners of a square (see Figure 14).

The use of cylindrical rods in lieu of hyperbolic electrodes complicates the calculation of the potential in the radial dimensions. However, if we continue to assume the trap is infinitely long and invariant in the z-dimension, the potential can be written as an infinite series of cylindrical multipole moments [75],

$$\Phi(\mathbf{r}, t) = \varphi(t) \sum_{m=0}^{\infty} C_m \left(\frac{r}{r_0}\right)^m \cos m\theta. \tag{35}$$

If the cylinders have the same radius, and they are arranged as in Figure 14, the boundary conditions require that the sign of Φ change if θ changes by $\pi/2$. Thus,

$$\cos\left(\frac{m\pi}{2}\right) = -1 \quad \Longrightarrow \quad m = 2\,(2n+1)\,, \;\; n = 0, 1, 2, \ldots \tag{36}$$

The first multipole term, corresponding to $n = 0$ is the quadrupole term. The next two largest terms, corresponding to $n = 1$ and $n = 2$, are the 12-pole term and the 20-pole term, respectively.

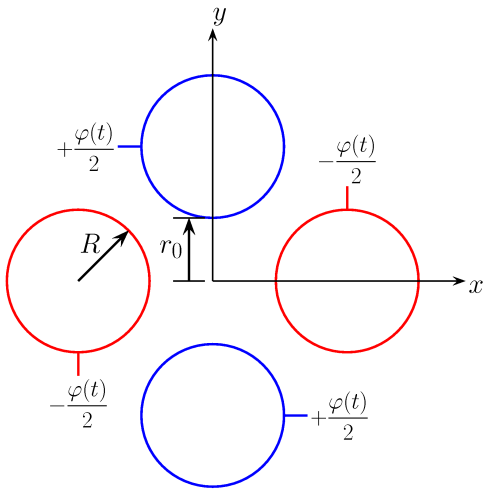

Figure 14: Cross-section of linear Paul trap with cylindrical rods. The cylindrical rods all have radius R and are placed such that their centers lie on the corners of a square. The distance from the trap center to the nearest point on the surface of any rod is r_0.

To achieve the closest approximation to a pure quadrupole field, one must limit the contributions of the higher order terms of the multipole expansion. This can be done by maintaining an optimal ratio between the radius of the trap rods and the radius of the trap itself. Denison [75] showed that if the cylinder radius was $R \approx 1.146 r_0$, the contribution of the 12-pole term could be made zero. Douglas and Konenkov, however, argued that the real potential most resembled a quadrupole potential when the contributions from the 12-pole term and 20-pole term were both small and of opposite sign. They found that a cylinder of radius $R \approx 1.13 r_0$ was optimal [76].

If the radii of the rods are made unequal, or if they are not placed as shown in Figure 14, additional multipole moments may arise beyond the limited set defined by Eq. (36). Means of producing hexapoles and octopoles and the effects of these fields on ion motion and stability are discussed in [77] and [78], respectively. The hexapole fields of [77] were introduced by rotating one pair of diametrically opposed rods[5] toward one of the other rods, while in [78], it was shown that octopole fields could be created by changing the

[5] In the ion trap vernacular, a *pair* or *set* of rods typically refers to two diametrically opposed rods that share the same electric potential.

radius of one set of rods or by moving one set of rods nearer or further from the trap axis.

One of the primary challenges in implementing a linear RF trap is the production of the high voltage RF drive. The ideal design calls for two signals of equal amplitude and opposite sign. Circuits designed to provide these signals can be found in the literature [79–82]. Our collaborators in the lab of Alex Kuzmich designed and built a similar circuit based upon the one that drives the RGA 300, a commercial residual gas analyzer from Stanford Research Systems [83]. These circuits typically operate at frequencies from 100s of kHz to a few MHz.

There are applications, such as resolved-sideband cooling [84], where higher trap frequencies are desirable. These high voltage, high frequency signals are commonly produced by using a coaxial resonator to amplify a small waveform from a signal generator [55]. These coaxial resonators feature a helical electrode inside a closed conducting cylinder. One end of the helical electrode is grounded to the conducting cylinder; the other end supplies the high voltage. The original small signal is introduced to the resonator via a small antenna.

Coaxial resonators are often built by hand according to the design parameters discussed by Macalpine [85]. The quality and frequency of the resonance depend strongly on a number of variables including the dimensions of the helix and conducting cylinder, the cleanliness of the internal surfaces, and the electrical properties of the load to which it's connected. Because of this, there can be significant variation between where a hand-built resonator is designed to resonate and where it actually resonates.

Building two resonators to oscillate at the same frequency 180° out-of-phase from one another poses an extreme challenge. However, a trapping field can be produced by using a single resonator to apply an RF signal to a single set of rods while RF grounding the other pair. If the rods lying on the x-axis are RF grounded, the instantaneous potential near the axis of the trap is approximately [64]

$$\Phi(\mathbf{r}, t) = \frac{1}{2}\left(V_{\mathrm{rf}} \cos \Omega t \pm U_{\mathrm{dc}}\right)\left[1 + \frac{y^2 - x^2}{r_0^2}\right]\cos \Omega t. \tag{37}$$

Here, the positive (negative) sign corresponds to the case when U_{dc} is applied to the same (opposite) pair of rods as V_{rf}. It can be easily verified that the x and y equations of motion of a charged particle in this potential are functionally the same as those in Eqs. 4 and 5. When operated in this way, an ion trap is said to be in *unbalanced mode*.

The electrodes responsible for axial confinement add another perturbation to the radial trapping fields. The presence of the endcap electrodes introduces a small z-component to the RF electric field [86]. As a result, the ion can experience micromotion in the axial dimension as well as the radial dimensions. Furthermore, the DC bias on the endcaps shifts the potential on the axis of the trap away from zero (see Figure 11). To account for this latter change, the correction factor a_{end}, defined in Eq. (34), must be added to the parameters a_x and a_y. Since a_x and a_y have opposite signs, this correction causes a shift in the position of the apex of the lowest stability region shown in Figure 7. However, the correction factor is normally very small and can usually be neglected.

2.3 Mass Spectrometry

The capability of the linear Paul trap to selectively confine ions according to their mass-to-charge ratios makes it a commonly utilized device in commercial mass spectrometers and residual gas analyzers. In this section, the physics underlying this capability is explained.

Recall the definitions of the stability parameters in Eqs. 6 and 7. For convenience, they are repeated here:

$$q = \frac{2ZeV_{\mathrm{rf}}}{mr_0^2\Omega^2}, \qquad a = \frac{4ZeU_{\mathrm{dc}}}{mr_0^2\Omega^2}. \tag{38}$$

The factors in these expressions can be separated into two categories, *trap parameters* and *ion parameters*. *Trap parameters* include the trap radius, r_0, the applied DC potential, U_{dc}, and the RF amplitude and frequency, V_{rf} and Ω. *Ion parameters* include the charge state, Ze, and the mass, m.

Note that for a fixed set of trap parameters, q and a depend inversely on the mass-to-charge ratio of the ion. Once the trap parameters are set, every possible mass-to-charge

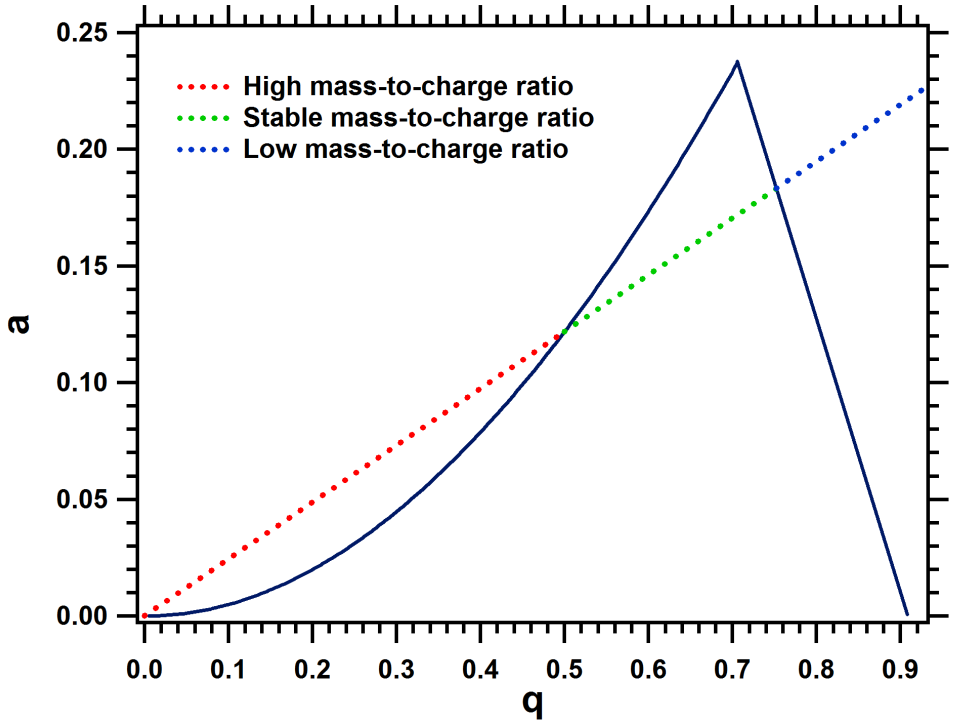

Figure 15: The operational line of an ion trap. The line passes through the origin and has slope $2U_{\mathrm{dc}}/V_{\mathrm{rf}}$. Every possible mass-to-charge ratio occupies a specific point on the line. Mass-to-charge ratios increase as the line approaches the origin and decrease as the line goes away from the origin.

ratio has a unique mapping to a single point in qa-space. The ion trap is constrained to operate on the line that is the locus of these points. This operational line passes through the origin and has slope $2U_{\mathrm{dc}}/V_{\mathrm{rf}}$. This is shown in Figure 15. The section of the line that lies within the region of stability represents ions that are stable in the given configuration of trap parameters. All other ions are unstable.

The expressions of Eq. (38) can be rearranged, and using the polynomial coefficients given in Table 1, one can plot the region of stability of an ion with a given mass-to-charge ratio in the space of the voltages V_{rf} and U_{dc}. Figure 16 shows the regions of stability for a few common molecules in their singly-charged state. For this example, the radius of the trap is $r_0 = 4.13\,\mathrm{mm}$ and the RF frequency is $\Omega = 2\pi \times 2.04\,\mathrm{MHz}$.

Examining Figures 15 and 16, a clear strategy emerges for isolating ions within an arbitrarily small mass-to-charge range. If the voltages V_{rf} and U_{dc} occupy a point near the

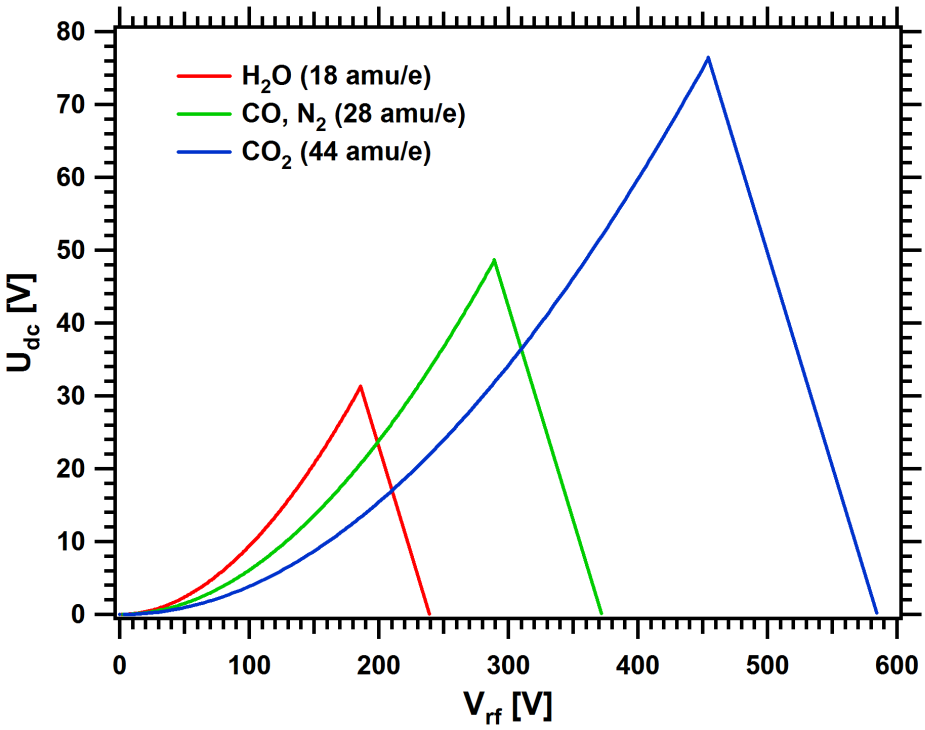

Figure 16: The stability regions of common molecules in their singly-charged state. For this example, the radius of the trap is $r_0 = 4.13\,\text{mm}$ and the RF frequency is $\Omega = 2\pi \times 2.04\,\text{MHz}$.

Figure 17: The RGA 100 from Stanford Research Systems [83]. Gas molecules are ionized via electron bombardment in the region enclosed in wire mesh on the right. The linear quadrupole filter occupies the space between the two white ceramic pieces. Detection electronics are located between the second ceramic piece and the 2.75" CF feedthrough flange. The control electronics are located in the box on the left.

apex of the region of stability of a particular ion, only that ion will be stable in the trap. By operating near the apex of the region of stability, commercial devices are often able to achieve better than 1 amu/e resolution [83]. This makes it possible to distinguish different isotopes of an atom from one another.

An example of a commercial device utilizing a linear Paul trap and epitomizing its usefulness in mass spectrometry is the RGA 100 from Stanford Research Systems, shown in Figure 17 [83]. The RGA 100 features a linear RF trap bracketed by an ionization region and detection electronics. Gas molecules are ionized on one end of the RF trap via electron bombardment, and are accelerated along the trap axis with a DC field. On the opposite side of the trap, the ions are detected via a Faraday cup or a channel electron multiplier. The ionizer and detection electronics run continuously. The DC and RF voltages of the trap are held at a constant ratio placing the operational line near the apex of the stability region. The voltages are ramped together, allowing each mass-to-charge ratio in turn to be stable in the trap region. Stable ions pass through the RF trap from the ionization region to the detectors, where they register a current. A mass spectrum is obtained by recording the detector current versus the series of stable mass-to-charge ratios of the trap.

Ion trap mass spectrometers like the RGA 100 are designed to produce and analyze singly-charged molecules. It is common in this context to overlook the difference between

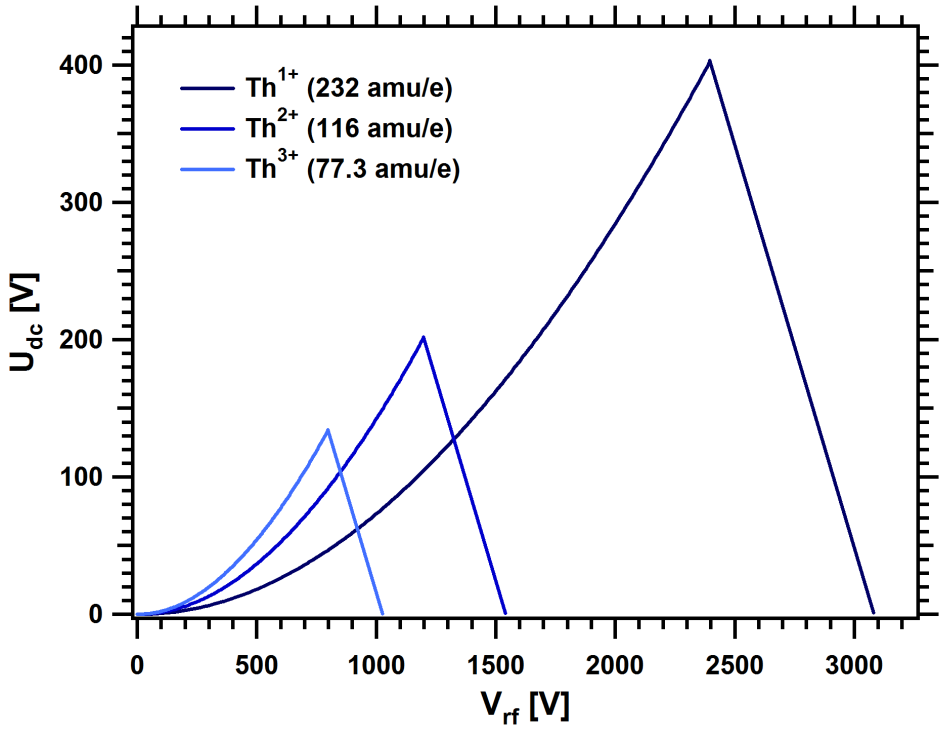

Figure 18: Stability regions of $^{232}Th^{+}$, $^{232}Th^{2+}$, and $^{232}Th^{3+}$. The radius and RF frequency of the trap are taken to be $r_0 = 4.13$ mm and $\Omega = 2\pi \times 2.04$ MHz, respectively.

the mass of an ion and its mass-to-charge ratio. In fact, the charge state factor Z is frequently omitted from the definitions of the stability parameters (Eq. (38)) in much of the ion trap literature. However, the distinction between the mass and the mass-to-charge ratio of an ion is critical. Figure 18 shows the stability regions in voltage space of $^{232}Th^{+}$, $^{232}Th^{2+}$, and $^{232}Th^{3+}$. The difference in the number of electrons in each of these ions represents less than a 0.1% difference in mass. Even so, the difference in their charge states makes their behavior in the ion trap significantly different.

Isolating the various charge states of thorium in an ion trap does not require the high resolution that can be obtained by operating near the apex of the stability region. Consider again Figure 18. Suppose the trap was being operated at $V_{rf} = 600$ V and $U_{dc} = 0$ V, and all three charge states were represented in the trap. If U_{dc} was then raised to just above 53 V, the singly and doubly-ionized thorium would become unstable, and only Th^{3+} would be left in the trap. On the other hand, if U_{dc} was held at zero, and V_{rf} was increased to 1600 V, the

singly ionized thorium would remain in the trap while the two higher charge states would be expelled. In general, to isolate an ion from those with a *higher* (*lower*) mass-to-charge ratio, U_{dc} (V_{rf}) must be raised to a point beyond the stability regions of the unwanted ions.

CHAPTER III

BARIUM ION TRAPPING

This chapter begins with a brief overview of our efforts toward the strong coupling of barium ions with a high finesse optical cavity. The details of this experiment are covered in the Ph.D thesis of Adam Steele [55]. The review presented here provides context for Section 3.2, which describes the primary contribution of the present author, the construction of a high temperature vapor cell for neutral barium spectroscopy. The construction of the vapor cell was motivated by our interest in photoionizing barium for loading in an ion trap. Although our vapor cell was made specifically for neutral barium, the design is suitable for spectroscopy of any alkaline-earth metal.

3.1 Experimental Overview

The original barium ion trap is shown in Figure 19. The trap consists of four stainless steel wires with a diameter of 0.84 mm, arranged to form a trap of radius 0.89 mm. Each rod in one diametrically opposed pair has a set of two endcaps on it. The endcaps are in the form of stainless steel tubes, which are insulated from the trap rods by polyimide tubing. The endcaps are arranged such that the length of the trap is 8 mm. The rods are held in place by alumina spacers at either end of the apparatus. The RF voltage for the trap is produced using a coaxial resonator as described in Section 2.2.

Laser cooling of Ba^+ is accomplished using the Λ-system shown in Figure 21(a). The $S_{1/2} \rightarrow P_{1/2}$ transition at 493 nm is driven by a frequency doubled diode laser system from Toptica Photonics (model #SHG-100). The $P_{1/2}$ state decays to the $S_{1/2}$ and $D_{3/2}$ states with a lifetime of 8 ns and a branching ratio of $2.8:1$ [87]. Another commercial laser from Toptica (model #DL100) at 650 nm is used to repump the population out of this state. The lasers copropogate through the trap at a 45° angle relative to the trap axis. The lasers are

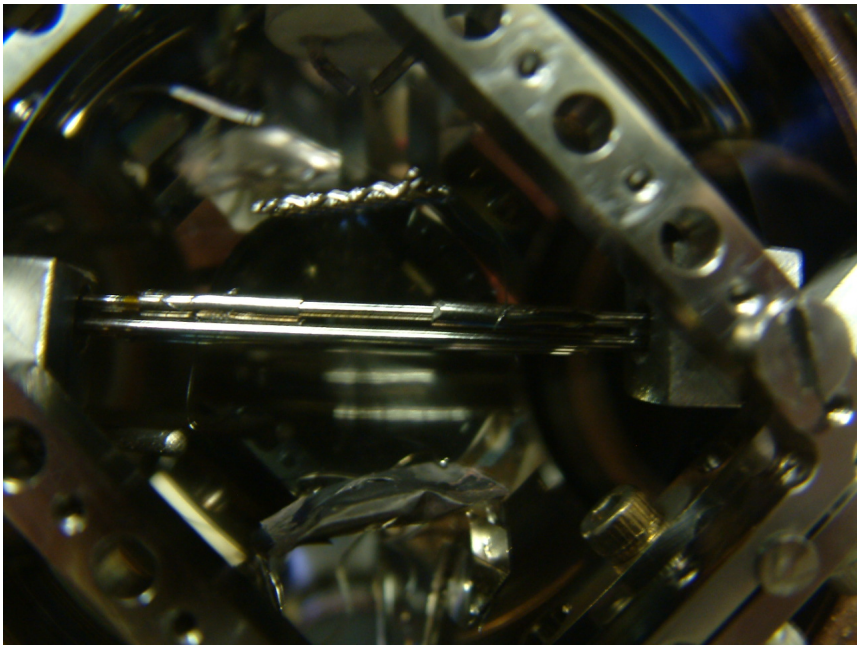

Figure 19: Original barium ion trap apparatus. The trap has a radius of 0.89 mm. The distance between the axial endcaps is 8 mm. The ion trap is assembled inside a Magdeberg Hemisphere from Kimball Physics (part #MCF450-MH10204/8-A). The trap is supported by groove grabbers, which were also purchased from Kimball Physics. Above the trap is the filament and bias plate utilized for electron bombardment ionization of barium. Below the trap is the tantalum foil oven that is used to create an atomic beam of neutral barium. Picture taken by A. Steele.

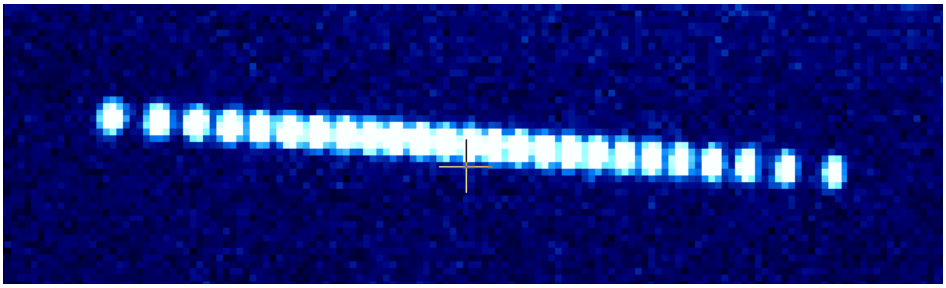

Figure 20: Barium Coulomb crystal.

shaped with cylindrical lenses to maximize the amount of the trapping volume illuminated. A weak magnetic field is applied to destabilize dark states in the $D_{3/2}$ Zeeman manifold [88]. Coulomb crystals, like the one shown in Figure 20, were commonly obtained.

An atomic beam of neutral barium is created using a resistively-heated oven made of tantalum foil. The oven is situated ~ 1 cm below the ion trap. It can be seen in Figure 19. Upon initial assembly of the system, the oven was filled with several small pieces of barium metal that were cut from a solid sample purchased from Alfa-Aesar. Barium oxidizes rapidly in air forming a hard white crust on the metal. Barium that is completely encrusted with oxide cannot be used to produce a vapor until the outer shell is broken.

To prevent oxidation, samples of barium used in the ion trap and vapor cell systems are prepared in a nitrogen environment. The general procedure is as follows. First, the vacuum chamber is completely assembled except for the single port through which the barium sample is to be inserted. The vacuum chamber is connected to the pumping system that will be used to evacuate it. A glove bag is sealed around the open port of the vacuum system using duct tape and/or cable ties. Everything necessary to prepare the barium sample and seal the vacuum system is placed inside the glove bag. This includes the container with the solid barium source, several razor blades, and a cutting surface. The pumping system and vacuum chamber are backfilled with pure nitrogen gas. This inflates the glove bag. While the nitrogen continues to flow, the glove bag is forcefully evacuated and then resealed. This is done several times to remove any residual air in the bag.

The barium sample is prepared by first chipping away the oxide layer on the solid

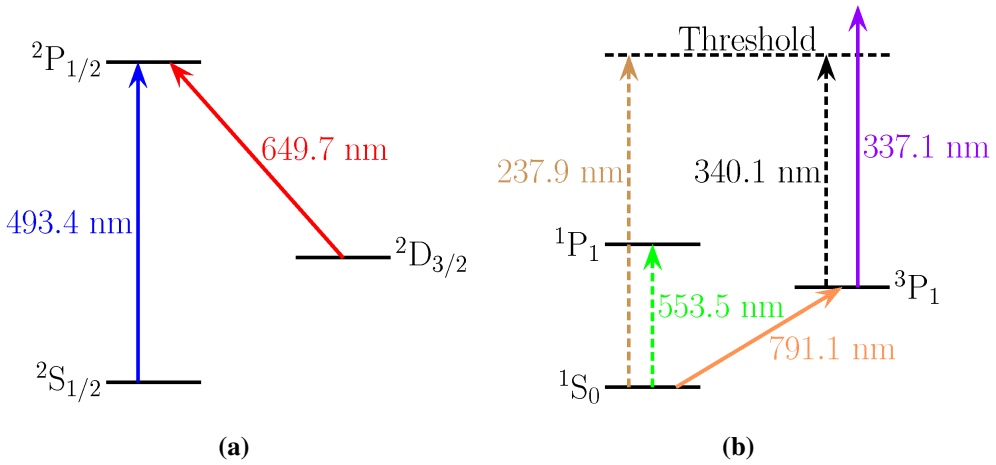

Figure 21: Electronic transitions in (a) singly-ionized and (b) neutral barium. Transitions represented by solid lines are used in this experiment. In (b), the two-photon photoionization scheme for neutral barium is shown. A laser at 791 nm excites the $^1S_0 \rightarrow {}^3P_1$ transition. The electron is subsequently driven to the continuum by light at 337 nm supplied by a nitrogen pulse laser.

barium source. This is done with a razor blade. Once an area is cleared of oxide, the razor blade can be used to cut a thin flake from the surface of the metal. The razor blade is held at a shallow angle relative to the surface of the metal, and the corner of the blade is pressed into the metal a short way. By working the blade back and forth under the surface, a small piece can be cut off. This process is repeated until the oven or crucible is filled with a sufficient quantity of barium. After the barium is inserted in the vacuum system, the port is sealed and the system is evacuated.

Two methods of electron bombardment were used to produce barium ions. The first method involved a simple electron beam produced by a tungsten filament and a bias plate. The filament and bias plate can be seen above the trap in Figure 19. In the second method, the light from a UV lamp is directed at the trap electrodes. This light causes photoemission of electrons from surfaces that have been coated with barium from the atomic beam. The electrons are accelerated in the RF trapping field and ionize barium in subsequent collisions [23].

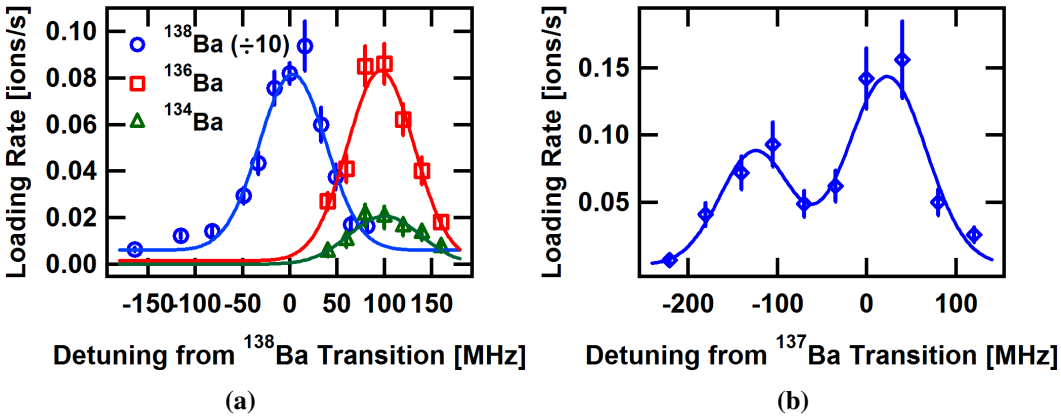

Figure 22: Barium photoionization loading rates. These results were reported by Adam Steele [23, 55]. (a) The loading rates of the even isotopes of barium, ^{138}Ba, ^{136}Ba, and ^{134}Ba. (b) The loading rates of the odd isotopes of barium, ^{137}Ba and ^{135}Ba.

Free electrons from an electron beam or photoemission can collect on insulating surfaces near the ion trap. The fields created by these electrons can potentially destabilize the trap. The accumulation of stray electrons is a particular concern when dielectric mirrors constituting an optical cavity are placed in close proximity with the ion trap. This motivated our search for a method of barium photoionization.

We developed a two-photon photoionization scheme for loading barium in the ion trap. The first step in this technique involves the resonant excitation of neutral barium atoms on an intercombination transition between the $^1S_0$ ground state and the $^3P_1$ state. This is done with an ECDL laser at 791 nm. From the $^3P_1$ state, the atoms are ionized with 337 nm light from a nitrogen pulse laser (model #NL100 from Stanford Research Systems). These transitions are depicted in the Grotrian diagram of Figure 21(b). The lasers counterpropogate through the trap at a 45° angle with respect to the trap axis. The 791 nm laser is focused to a 100 μm waist at the trap center. The waist of the nitrogen laser at the center of the trap is 900 μm.

The natural linewidth of the $^1S_0 \rightarrow {}^3P_1$ transition is 50 kHz [89], while the frequency shifts between the various isotopes are all $>$ 10 MHz. By tuning the 791 nm laser to the transition frequency of a specific isotope, that isotope can be loaded in the ion trap to the

exclusion of all others. The ability to do this within our apparatus was mitigated somewhat by Doppler broadening, which was a result of the atomic beam being uncollimated. However, this only limited isotope selection between the ^{136}Ba and ^{134}Ba isotopes. The experimental results are shown in Figure 22.

The photoionization method described here requires an absolute frequency reference for the 791 nm $^1S_0 \rightarrow {}^3P_1$ transition. In our experiment, this was provided by a novel, high-temperature vapor cell, which is the subject of the next section.

3.2 Barium vapor cell

Several significant technical challenges must be overcome to perform spectroscopy on an alkaline-earth metal. First, to produce a vapor that is of sufficient optical density for spectroscopy, the sample must be heated to temperatures that are incompatible with standard CF vacuum seals. Accordingly, the heating mechanism must be adequately removed from such seals, or an active cooling mechanism must be employed. Matters are further complicated by the corrosive nature of the alkaline-earths and the ease with which they react with silicate based viewport windows. Windows in contact with the vapor must be made of a non-reactive material, and they must be maintained at a higher temperature than all the other surfaces in contact with the vapor to inhibit the formation of a coating on the window [90–92]. Alternatively, the windows must be isolated from the vapor entirely.

Several techniques that overcome the difficulties of performing alkaline-earth spectroscopy have been proposed and implemented by other groups. Traditionally, heat pipes have been used to create metal vapors for spectroscopic studies [93]. Heat pipes are typically designed with a large separation between the vacuum viewports and the heated vapor region, and, to further reduce interaction between the windows and vapor, they are filled with an inert buffer gas. The additional length, however, makes the heat pipe rather bulky, while the presence of a buffer gas leads to collisional broadening of the atomic resonances in the sample. Optogalvanic techniques are typically implemented in similar apparatuses,

and thus also produce pressure-broadened resonances [94, 95]

Using an atomic beam to supply the vapor for spectroscopy eliminates the danger of contaminating optical windows; however, the collimation process reduces the overall density of the vapor and, hence, the strength of the spectroscopic signal, necessitating more sensitive – and expensive – optical detectors. For example, Ferrari et al. [96] used a photomultiplier tube to detect fluorescence from an atomic beam with a density of $10^8\,\mathrm{cm}^{-3}$, four orders of magnitude less than the densities we achieve.

Dual chamber designs, which use non-reactive windows to confine the vapor to only a portion of the total chamber, have been developed [90, 91]. Since the entire chamber is evacuated, the seals holding the inner windows in place do not need to hold vacuum; they need only slow the diffusion of the vapor into the outer regions of the chamber. Therefore, the windows can be safely held at temperatures greater than the rest of the surfaces in the vapor region. However, these windows represent an additional cost in building the chamber, and having separate chambers also complicates the evacuation process, as each section must be pumped down simultaneously.

Over the course of the barium experiment, two vapor cells for neutral barium spectroscopy were built. These cells are remarkably simple. After initial evacuation down to $< 10^{-5}$ torr and sealing with an all-metal valve, the vapor cells do not require any further pumping. Furthermore, the vapor cells do not require a buffer gas, an active cooling mechanism, collimation of an atomic beam, or special windows or viewports. Both are constructed almost exclusively from standard, commercially available vacuum components.

The original vapor cell is shown in Figure 23. The cell is built using 1.33” CF components and sealed with an all-metal valve. The all-metal valve is connected to the cell via a 90° elbow, which thermally isolates the valve from the heated region.

Baffles with small apertures are used to eliminate all direct lines of sight between the viewports and the heated surfaces in the vapor region. These barriers are located outside of the heating region, so their temperatures are considerably less than those of the directly

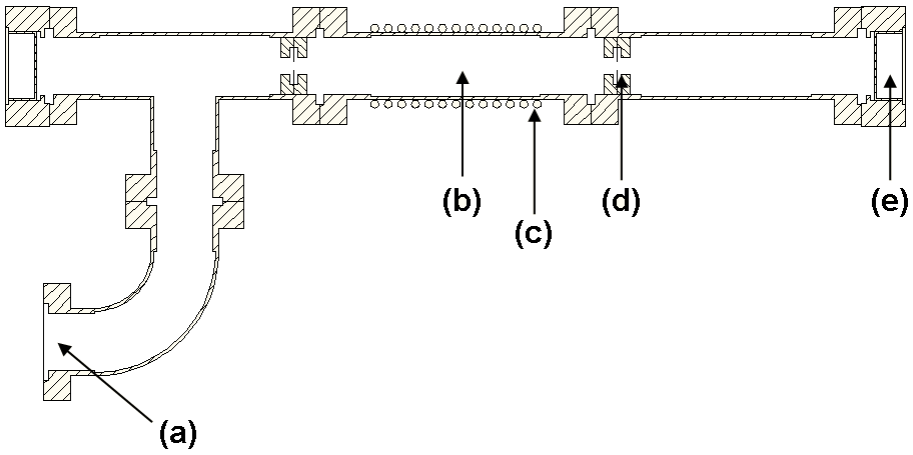

Figure 23: Original barium vapor cell. Noted in the diagram are the (a) connection to pump via all-metal valve, (b) vapor region, (c) coaxial heater, (d) aperture and washer assembly, and (e) viewport.

heated surfaces. The presence of these baffles has proven sufficient to prevent the contamination of the vacuum viewports. This fact indicates that the gaseous barium atoms in the center nipple do not take the form of a conventional vapor, as the velocity classes with vectors directed through the apertures are unrepresented in the sample.

This condition can be explained if the barium deposited on the heated surfaces of the cells is considered as a collection of atomic sources. Since there is no line of sight between the heated surfaces and the viewports, an emitted atom cannot follow a straight trajectory to the viewport. A barium atom could be directed toward the viewports via a collision with another atom; however, for atomic densities on the order of $10^{13}\,\mathrm{cm}^{-3}$ or less, which we measure in these cells, the mean free path of a Bohr atom is orders of magnitude larger than any linear dimension in the cell, which indicates such velocity-changing collisions are vanishingly rare.

The baffles of the original cell are composed of stainless steel in the form of .003" shim and washers $5/8$" in diameter and $3/16$" thick. These washers are designed to fit snugly inside the vacuum components, and they represent the only custom machined pieces in the original vapor cell. For each baffle, a piece of shim is glued between two washers using

high temperature cement (Sauereisen Electrotemp Cement No. 8). An aperture, 3/32" in diameter is drilled in the shim, and the assembly is secured inside the cell using the same high temperature cement.

The original cell is heated by a resistive coaxial heater (ARi Industries, BXX09B-29-4T), which is wrapped tightly around the center nipple and secured with stainless steel hose clamps. It was found that using a non-coaxial heater resulted in an oscillation in the signals at the line frequency (60 Hz). This oscillation was not present when the current supply for the non-coaxial heater was off, nor was it present when the coaxial heater was used, indicating that the oscillation was due to an AC Zeeman effect.

The heater and hose clamps were covered with several layers of UHV quality aluminum foil. UHV foil is used as it is free of oils found on other grades of aluminum foil that cause smoking during operation. Care was taken to ensure that the flanges immediately adjacent to the heater were left completely uncovered by the insulating foil. Passive air cooling was found to be sufficient in limiting the temperature at the flanges to below 550°C when the cell was operated at temperatures sufficient to obtain 100% absorption on the ^{138}Ba resonance. Although this temperature is higher than the specification for CF seals, no loss of vacuum was observed.

Over the lifetime of the cell, which totaled over 1000 hr, the heater was replaced three times. The failure rate of the heaters varied widely. In each instance of failure, it was found that the insulating sheath of the heater, which was composed of Inconel 600, had been compromised, thus creating a potentially dangerous situation where the internal wire of the heater was shorted against the vapor cell.

This notable shortcoming motivated the design of the improved vapor cell shown in Figure 24. This cell features an 8" long center nipple, which accommodates two 4" long helically wound, semi-cylindrical ceramic heaters from Thermcraft, Inc. The heaters have an inner radius of 0.5", while the outer radius of the nipple is 0.375". The heaters are offset from the chamber by small ceramic shims. This eliminates the possibility of an exposed

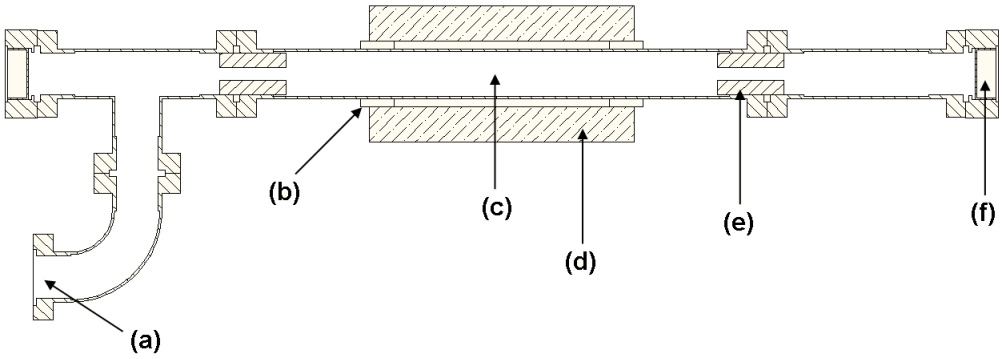

Figure 24: Improved barium vapor cell. Noted in the diagram are the (a) connection to pump via all-metal valve, (b) ceramic shim, (c) vapor region, (d) helically wound ceramic heater, (e) aperture rod, (f) viewport.

wire in the heater shorting to the cell.

This design has several other advantages over its predecessor. The additional relief between the heater and the flanges of the center nipple allow passive air cooling to keep the latter from reaching temperatures above their nominal rating. Furthermore, the longer vapor region reduces the density of vapor required to achieve a given level of absorption. Therefore, lower overall temperatures can be used. This, combined with the durability of the ceramic heater, has allowed for uninterrupted operation of the cell for over a year.

The baffles in the improved cell are in the form of stainless steel cylinders, 1" long, with 3/16" and 5/8" inner and outer diameters, respectively. By using a longer baffle, a sufficient barrier between the vapor and viewports can be maintained while increasing the diameter of the aperture. The larger diameter aperture simplifies the initial alignment of the laser through the cell.

Upon initial construction of each of the cells, a small crucible was filled with a few grams of barium metal and placed in the center nipple. The crucible was made of stainless steel foil, which had been rolled into a small tube approximately 1.5" in length and 3/16" in diameter. The ends of the tube were folded over and spot welded, and a long slit approximately 1/16" wide was cut in its top.

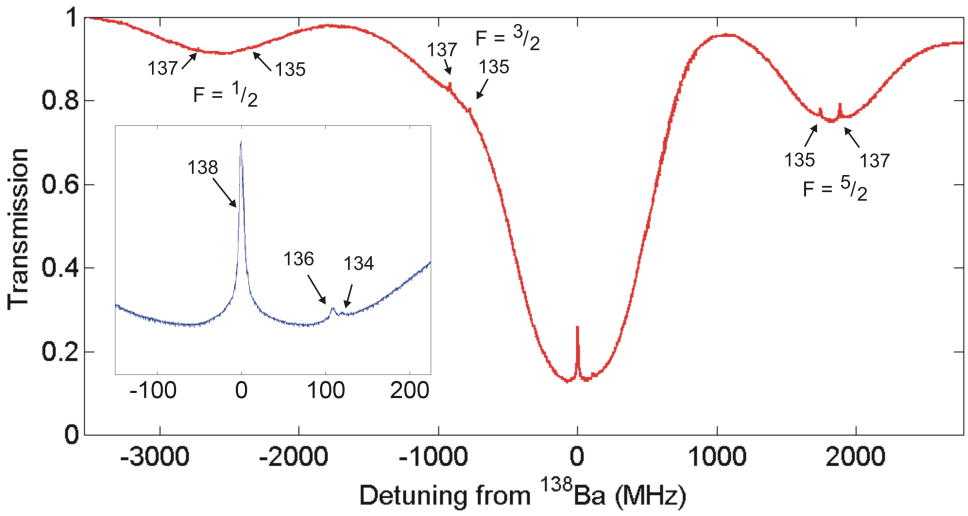

Figure 25: Saturated absorption spectra for the $^1S_0 \rightarrow {}^3P_1$ transition in neutral barium. The original vapor cell was used to obtain the data presented here. The spectra shown were compiled from five scans taken over smaller frequency ranges. All offsets are given relative to the ^{138}Ba feature. The isotopes were identified by comparison to [97]. (Inset) A zoomed image of the even isotope features.

An example of the spectra obtained from the barium cell is shown in Figure 25. Saturated absorption spectroscopy, with pump and probe beams derived from the same laser was used for all spectra presented. The light was provided by a grating stabilized diode, mounted in a standard, temperature stabilized, extended cavity diode laser (ECDL) configuration. A Fabry-Perot cavity with a free spectral range of 536 ± 4 MHz was used as a frequency reference. The saturated absorption signal and the cavity transmission signal were detected with photodiodes. Sub-Doppler features were identified for all isotopes with relative abundances greater than 1%, including features for each of the hyperfine states of ^{137}Ba and ^{135}Ba. All features were clearly visible without lock-in amplification or oscilloscope averaging.

The FWHM linewidth of the sub-Doppler features was found to be less than 10 MHz for a probe intensity of $I = 100 I_{\text{sat}}$. Decreasing the intensity of the probe did not have an appreciable effect on the width of the features, suggesting that the linewidth was limited by another broadening mechanism.

The relative transmission through the cell can be adjusted by varying the temperature of

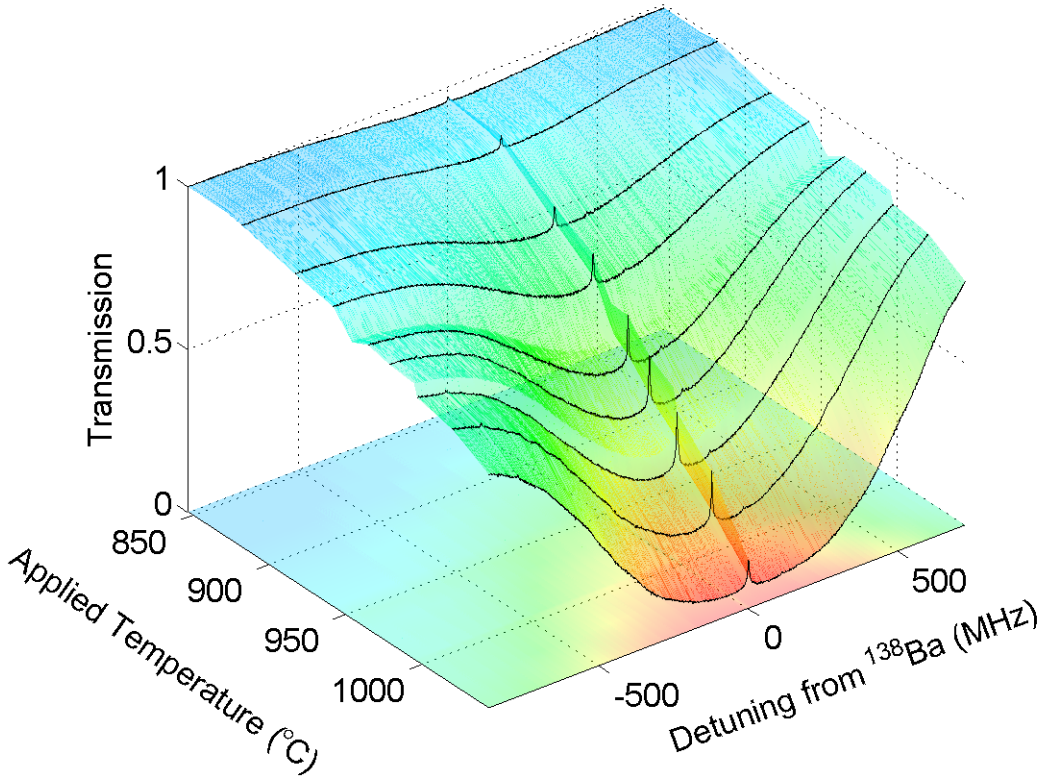

Figure 26: Absorption spectra near the ^{138}Ba resonance as a function of temperature.

the cell as shown in Figure 26. The relative absorption in the vicinity of the ^{138}Ba resonance varies from less than 10% to nearly 100% over a temperature range of 200°C up to 1050°C.

The atomic number density, n, was estimated from the Beer-Lambert law,

$$n = -\frac{\ln(\tau)}{\sigma_{\text{eff}}\ell}, \tag{39}$$

where τ is the transmission, σ_{eff} is the effective absorption cross-section, and ℓ is the interaction length. The effective cross-section is obtained by multiplying the natural absorption cross-section, $\sigma_0 = 3\lambda^2/2\pi$, by the ratio of the natural linewidth to the Doppler-broadened linewidth [90]. Therefore, the effective absorption cross-section is temperature dependent. The average temperature of the atomic ensemble is not easily extracted; however it must be less than or equal to the hottest measured temperature along the cell. From our data, we conclude that for an applied temperature corresponding to 50% absorption, an atom density

greater than $10^{12}\,\mathrm{cm}^{-3}$ was attained.

CHAPTER IV

THORIUM ION TRAPPING

In the next two chapters, we review the progress of our triply-ionized thorium ion trapping experiment. This chapter begins with a discussion of the experimental apparatus. The characteristics of the two linear ion traps used in the experiments are detailed in Section 4.1.1. This is followed in Section 4.1.2 by a discussion of the UHV system, and the two means of ion detection used in the experiments, observation of optical fluorescence and mass-selective CEM detection, are discussed in Section 4.1.3 and Section 4.1.4. This is followed by a discussion of Th^{3+} ablation loading methods. Spectroscopy of the ground state Λ-system is demonstrated, and a technique for producing ablation targets from trace quantities of thorium nitrate is discussed.

In the chapter that follows, we discuss the primary mechanisms by which Th^{3+} ions are lost from the trap, charge exchange and chemical reactions. Experiments that were performed to determine rate coefficients for reactions between Th^{3+} and various gases are discussed. The chemical evolution of trapped Th^{3+} in the presence of carbon dioxide, methane, and oxygen is presented.

4.1 Overview of Apparatus

Two different linear Paul traps were used over the course of the experimental program described in this chapter. The first was originally constructed by Adam Steele and described in his Ph.D thesis [55]. The trap was created by adding endcap electrodes to a commercial linear mass filter, the RGA 100 [83]. The second trap was originally designed by Corey Campbell. This trap has also been described previously [35]. Before being used in these experiments, the latter trap was modified by the present author to incorporate a channel electron multiplier (CEM) for electronic detection of ions. For the sake of brevity, we will

refer to these traps as the *modified RGA trap* and the *modified Campbell trap* in the text that follows.

The remainder of this section will discuss these traps and the additional experimental apparatus that was used to perform the experiments presented later in the chapter. Details of the traps' design and construction are examined in Section 4.1.1. Section 4.1.2 describes the ultra-high vacuum UHV systems in which the traps were operated. Sections 4.1.3 and 4.1.4 are dedicated to the two methods of ion detection used in these experiments.

4.1.1 Trap Characteristics

The modified RGA trap is shown in Figure 27. The quadrupole probe of the commercially available SRS RGA 100 constitutes the underlying mechanical structure of this trap. The RGA linear quadrupole mass filter comes mounted to a 2.75" CF electrical feedthrough. The quadrupole filter rods are $1/4$" in diameter and 4" long. They are held parallel by two precisely ground alumina pieces, forming a trap radius of 0.109". The ratio of the trap rod radius to the trap radius is chosen to minimize the contribution of the largest non-quadrupole term to the field as discussed in Section 2.2. The ratio used here is equivalent to the optimal ratio found by Denison [75] for such a trap. A brief description of the normal intended operation of the RGA 100 can be found in Section 2.3.

Endcap electrodes were added to the RGA mass filter to provide axial confinement. The electrodes were made from 0.001" stainless steel shim. At each end of the trapping region, a narrow piece of shim was wrapped around each rod of a diametrically opposed pair. The shim was spot welded to form a tight loop on the rod. These loops were placed to form a trapping region $\sim 25\,\text{mm}$ in length. This distance is only about $1/4$ the total length of the trap rods. The shim is insulated from the trap rod with $1/4$" wide Kapton tape purchased from Accu-Glass, Inc. This tape uses a UHV compatible silicon adhesive that can withstand baking at up to 260°C. The two endcaps on either side of the trapping region share a common electrical connection.

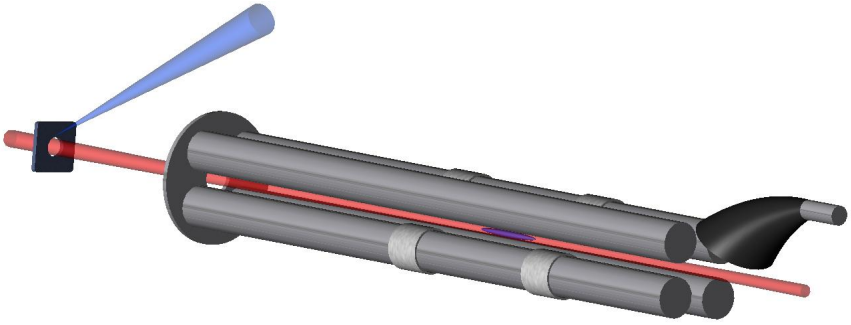

(a)

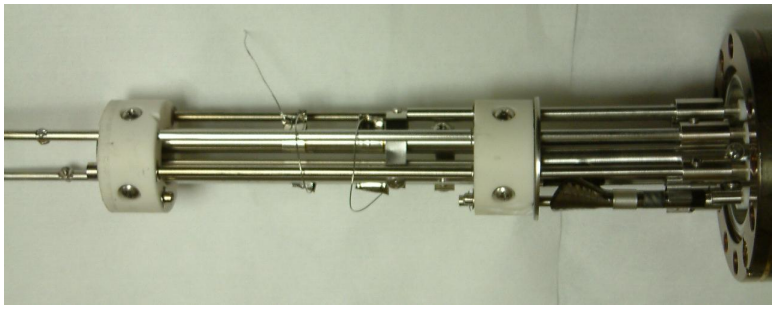

(b)

Figure 27: The modified RGA trap. (a) Conceptual drawing by C. Campbell [55]. A square thorium ablation target is shown at the extreme left. The third harmonic of a pulsed Nd:YAG laser is focused onto the target. The incident light creates a plasma consisting of neutral and ionized thorium and electrons. The contents of this plasma move at high velocity (10s of km/s [54, 55]) toward the ion trap. A large negative bias applied to the focus plate at the end of the rods focuses the ions into the trapping region. The added endcap electrodes confine the ions axially until they are dumped into the CEM (located at the extreme right) for electronic detection. Lasers used for optical excitation are directed down the axis of the trap from left to right. (b) Photograph of the trap. The RGA ionizer had been removed prior to this photograph.

Both the modified RGA trap and the modified Campbell trap are loaded by ablating targets of thorium metal or thorium nitrate ($Th(NO_3)_4$). In the case of the RGA trap, the ablation targets are placed within a few inches of the end of the trap rods. A high negative bias is applied to a focusing plate at the end of the rods. The resulting potential focuses the ions through an aperture at the center of the plate and into the trapping region. The ablation loading process is discussed in detail in Section 4.2.

Under normal operating circumstances, the RGA 100 utilizes electron bombardment ionization to produce the ions it subsequently mass analyzes. The ionization system (or ionizer) consists of a thoriated iridium filament that circumscribes a wire mesh cylinder called the anode grid. Both the filament and the anode grid are enclosed by another wire mesh cylinder called the repeller. This ionizer was not used in any of the experiments presented here. The components of the ionizer were ultimately removed so ablation targets could be placed in closer proximity to the trap.

The modified Campbell trap is shown in Figure 28. This trap features 3/8" (9.525 mm) diameter trap rods held to form a trap radius of 4 mm. The rods are 37 mm in length. The endcap electrodes are in the form of 1/16" thick plates with apertures 6.25 mm in diameter at their centers. The dimensions of this trap were used in preparing several of the graphs in Chapter 2.

The trap rods and endcaps are held together by compression between two stainless steel endplates. The endplates are aligned on two #4-40 threaded rods and held in place by nuts. Another set of stainless steel plates holds the #4-40 threaded rods. The entire assembly is mounted inside a Kimball Physics model MCF800-SO2000800 spherical octagon by securing this last set of plates to Kimball Physics model MCF800-GG-CA07 groove grabbers with #4-40 screws. Alignment of the endcaps and trap rods is done with small lengths of 1/16" diameter ceramic rod. The endplates, endcaps, and rods are electrically isolated from each other by ceramic washers 1/32" in thickness.

Several ablation targets are placed ~ 10 mm from the front endcap of the modified

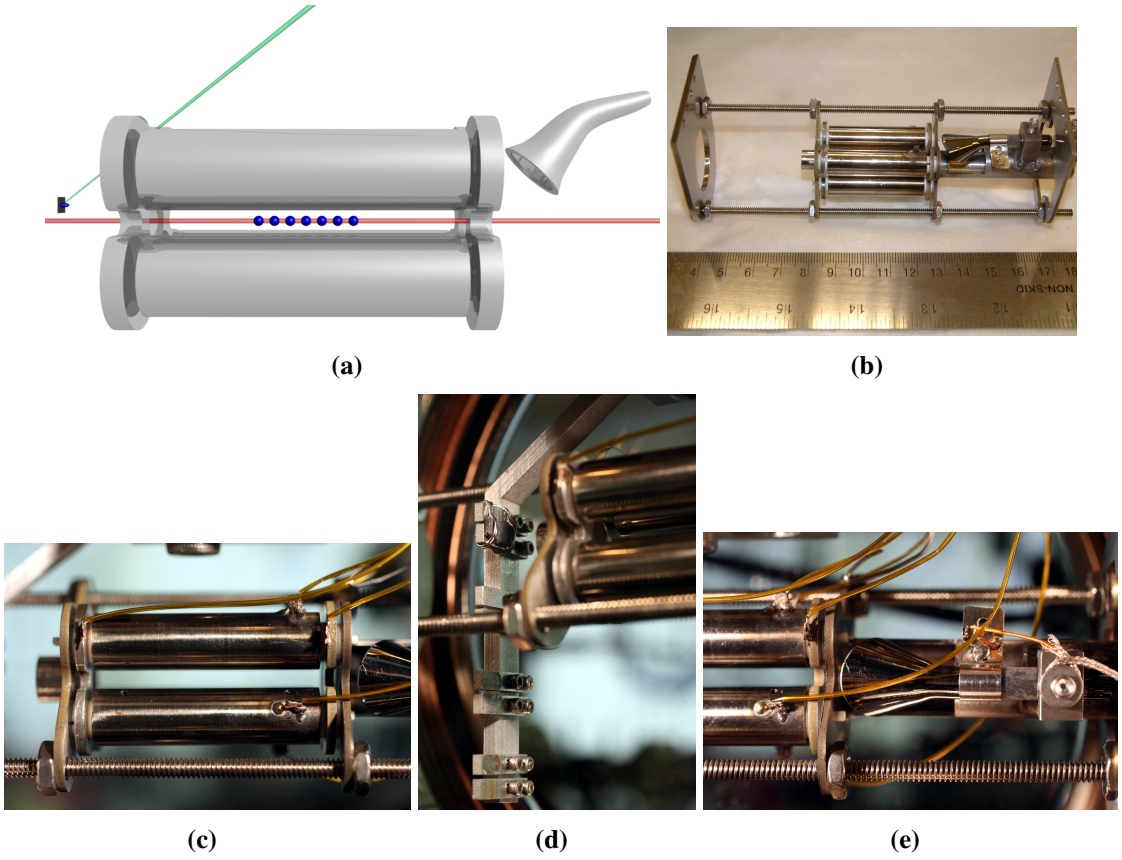

Figure 28: The modified Campbell trap. (a) Conceptual drawing by M. DePalatis. A target to the left of the ion trap is ablated using the third harmonic of a pulsed Nd:YAG laser. The ions produced during ablation are subsequently trapped. Lasers used for optical excitation are aligned along the trap axis. The CEM to the right of the trap is used for electronic detection. The CEM is mounted off-axis to allow clear optical access. (b) Photograph of the trap prior to installation in vacuum chamber. (c) Photograph of the trap inside the vacuum chamber. (d) The ablation targets are mounted to a linear translator, which allows each target to be moved into position for loading. The targets are, from top to bottom, ^{232}Th metal, two samples of 100 μg of ^{232}Th from nitrate solution, two samples of 10 μg of ^{232}Th from nitrate solution, and two samples of 10 μg ^{229}Th from nitrate solution. (e) The CEM. Photographs (c), (d), and (e) taken by M. DePalatis.

Campbell trap. The targets are attached to a linear translator, which allows each target to be moved into position for loading. The targets can also be moved to allow complete optical access through the endcap apertures. The target mounting system and target substrates are fabricated from grade 6061 aluminum. A piece of thorium metal is strapped to the uppermost substrate with stainless steel wire. The remaining substrates carry small samples of thorium nitrate. The method for creating thorium nitrate samples is discussed in Section 4.4.

The high voltage RF for the traps is provided by a power supply (model PSRF-100) purchased from Ardara Technologies. This power supply produces two RF signals that are 180° out-of-phase and up to 1000 V in amplitude. The amplitude of the signals is controlled by a $0 - 5$ V DC control voltage. The unit automatically adjusts the frequency at which it oscillates according to the electrical characteristics of the load to which it is attached. It generally oscillates at ~ 2 MHz. When attached to the modified Campbell trap, its frequency is 2.04 MHz.

4.1.2 Vacuum System

An ion trap is housed within a UHV chamber while it is in use. Prior to being assembled in the UHV chamber, the components of an ion trap are cleaned with methanol or acetone. The cleaning is done either by hand or in an ultrasonic cleaner. Assembly of the trap and the vacuum chamber is done in a clean environment. Latex or nitrile gloves are worn whenever handling elements of the trap or vacuum chamber.

The UHV system features a dedicated turbomolecular pump, an ion pump, and a titanium sublimation pump. The turbo pump is a model TMU 071 P from Pfeiffer Vacuum, Inc., and it is backed by a Varian IDP series dry scroll pump. The turbo pump is connected to the rest of the vacuum system via a Varian all-metal right angle valve. This significantly reduces the effective pumping speed of the turbo pump, but it allows the turbo pump and scroll pump to be powered off for maintenance while preserving the quality of the vacuum

in the rest of the system.

The pressure inside the vacuum system is monitored with a Varian model UHV-24 Bayard-Alpert style ion gague. Ion gauges do not measure pressure directly. They employ a hot filament to ionize residual gas molecules via electron impact. These ions are collected on an electrode, and the resulting current is converted into a pressure measurement. The specific sensitivity of the ion gauge depends on the gas being measured. Ion gauges are calibrated with respect to nitrogen. Correction factors for other gases can be found in the Varian manual for the UHV-24 gauge [98]. Values in the text are given as read without correction unless otherwise noted. When corrected, the correction factor will be explicitly stated.

One of two precision leak valves is used when introducing a gas into the system. The flow of helium into the system is controlled by a Granville-Phillips model 203 variable leak valve. Other test gases are introduced via an LVM series leak valve from Kurt J. Lesker, Inc. Both leak valves have 2.75" CF flanges on both their UHV and high pressure sides. The inlet ports of the leak valves are connected to the pressure regulators on their respective gas cylinders using 2.75" CF to 1/4" Swagelok adapters and 1/4" copper tubing.

Whenever gases are leaked into the system, the ion pump is powered off. The getter surfaces of the ion pump can become saturated if the pump is operated while large quantities of gas are present. Once saturated, these surfaces begin to outgas, resulting in a continuous leak into the system. The only remedy in this situation is a thorough bakeout of the ion pump.

After the ion trap and the UHV chamber are first assembled, the entire system is baked at up to 300°C for a period of several days to a few weeks. The turbo pump operates during this time. The high temperature accelerates outgassing rates, allowing gas molecules adsorbed to surfaces to be more rapidly removed from the system. In most cases, the ion pump is powered off and its magnets removed during the bakeout.

During bakeout, both the UHV and high pressure sides of the leak valves must be

under vacuum to prevent oxidation of the sealing surfaces. Evacuation of the gas handling apparatus on the high pressure side of a leak valve is done in one of two ways. The first method is to simply open the leak valve to its maximum conductance and allow the volume to be pumped through the valve. However, even with the valve open to its maximum conductance, the pumping rate through it is extremely small. The gases that remain in the volume or adsorbed to the surfaces inside it can potentially contaminate the pure gases that are ultimately administered into the system.

The second method of evacuation involves attaching a separate pumping system directly to the gas handling apparatus via a large conductance connection. The pumping system consists of a turbomolecular pump and roughing pump. It is connected to the gas handling apparatus through a Varian model 9515017 all-metal tee valve fixed between the input port of the leak valve and the 2.75" CF to 1/4" Swagelok adapter. When the valve is closed, the gas handling apparatus is isolated from the pumping system, but gas is still free to flow from the gas cylinder to the input port of the leak valve around the valve bellows. Gas introduced to the system from an apparatus evacuated using this method was found to have less impurities than gas introduced to the system from an apparatus evacuated using the first prescribed method.

Regardless of the evacuation method used, it is general practice to keep the copper tubing section of the gas handling apparatus as short as possible to limit the amount of volume to be pumped. A Swagelok model SS-4BG stainless steel bellows-sealed valve is located along the tubing immediately adjacent to the CF-to-Swagelok adapter. Whenever a cylinder is changed, this valve is closed to limit the exposure of the leak valve to atmosphere.

4.1.3 Optical Excitation and Observation

Since it has only one optically active electron, the level structure of $Th^{3+}$is relatively simple. The four lowest electronic energy levels in $Th^{3+}$are shown in Figure 29. Two strategies for optical excitation are apparent. A cycling transition at 1087 nm exists between the $5^2F_{5/2}$

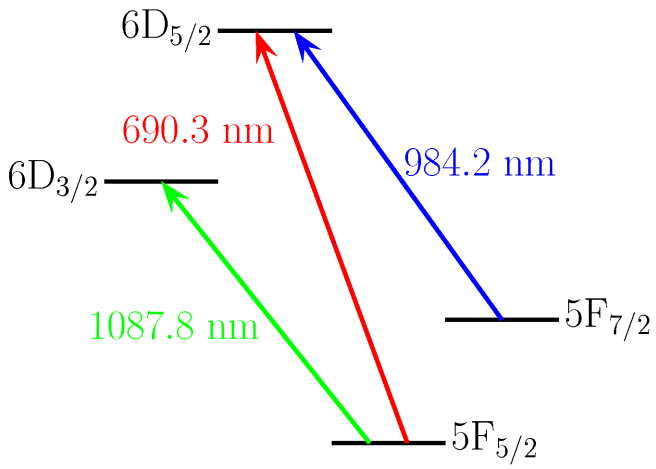

Figure 29: Th^{3+}energy levels and optical transitions.

ground state and the $6^2D_{3/2}$ state, while a Λ-system with transitions at 690 nm and 984 nm connects the $5^2F_{5/2}$, $6^2D_{5/2}$, and $7^2F_{7/2}$ states.

To date, the most accurate measurements of the transition frequencies between the states shown in Figure 29 were performed by our group [35]. Prior to our work, the spectral structure of Th^{3+}had been studied extensively by Klinkenberg [36]. The spectrographic data he analyzed was produced in a series of experiments involving the high voltage discharge of a thorium electrode in vacuum. In addition to the spectral lines arising from excitation of Th^{3+}, the data included spectra from all lower charge states and several higher charge states. Only by carefully eliminating those lines due to other charge states and by application of state-of-the-art atomic theory was he able to identify the three lines shown in Figure 29. The accuracy of the experimental data was limited by Doppler and collisional broadening in the vacuum discharges to ~ 500 MHz.

The values reported by Klinkenberg provided a starting point for our own search for these optical transitions [55]. Ultimately, our group found that the values for the $5F_{5/2} \leftrightarrow 6D_{3/2}$ (1087 nm) and $5F_{7/2} \leftrightarrow 6D_{5/2}$ (984 nm) transitions were within experimental error of the values published by Klinkenberg. The $5F_{5/2} \leftrightarrow 6D_{5/2}$ (690 nm) transition, however, was found to be ~ 1.9 GHz above the previous value. Both sets of values are shown in Table 2.

Table 2: Frequencies of relevant $^{232}Th^{3+}$ electronic transitions. The most accurate measurement of the frequencies to date was done by our group [35]. The previously accepted values of the frequencies were reported by Klinkenberg [36].

Transition	ν **[THz] (previous)**	ν **[THz] (current)**
$5F_{5/2} \leftrightarrow 6D_{3/2}$	275.6065(5)	275.606583(26)
$5F_{5/2} \leftrightarrow 6D_{5/2}$	434.2895(5)	434.291397(26)
$5F_{7/2} \leftrightarrow 6D_{5/2}$	304.6193(5)	304.619344(26)

The lifetimes of the $6D_{3/2}$ and $6D_{5/2}$ excited states were calculated by Safronova [99] to be 1090.0 ns and 676.0 ns, respectively. The lifetime of the $6D_{3/2}$ state implies a linewidth of 146 kHz for the 1087 nm transition. The linewidths of the 690 nm and 984 nm transitions are related to the $D_{5/2}$ lifetime according to

$$\frac{1}{\tau_2} = 2\pi \left(\Gamma_{21} + \Gamma_{23}\right), \tag{40}$$

where the subscripts 1, 2, and 3 denote the states $5F_{5/2}$, $6D_{5/2}$, and $5F_{7/2}$, respectively. Combining this expression with [100]

$$\Gamma_{ij} \propto \frac{\omega_{ij}^3 g_j D_{ij}^2}{g_i} \tag{41}$$

yields the equations

$$\Gamma_{21} = \frac{1}{2\pi\tau_2}\left[1 + \frac{\omega_{23}^3 g_3 D_{23}^2}{\omega_{21}^3 g_1 D_{21}^2}\right]^{-1} \tag{42}$$

$$\Gamma_{23} = \frac{1}{2\pi\tau_2}\left[1 + \frac{\omega_{21}^3 g_1 D_{21}^2}{\omega_{23}^3 g_3 D_{23}^2}\right]^{-1}. \tag{43}$$

Here, ω_{ij} is the transition frequency between states i and j, g_i is the degeneracy of state i, and D_{ij} is the dipole matrix element between states i and j. The dipole matrix elements are given by Safronova [99] as $D_{21} = 0.4116\, ea_0$ and $D_{23} = 1.9190\, ea_0$, while the degeneracies are $g_1 = 6$ and $g_3 = 8$. Putting everything together, we find that the linewidths of the 690 nm and 984 nm transitions are 21 kHz and 214 kHz, respectively. This implies a branching ratio from the $6D_{5/2}$ state of $\sim 10:1$ in favor of the $5F_{7/2}$ state. Our own measurement of the branching ratio [55] is consistent with this value.

Extended cavity diode lasers in the standard Littrow configuration supply the light for optical excitation of Th^{3+}. In each laser setup, the grating is mounted to a New Focus model 9807 mirror mount. Fine control of the grating angle in each laser is accomplished with a piezoelectric transducer (PZT) and a Thor Labs PZT driver. The rest of the laser assembly and all other electronics used to operate the laser are home-built. Laser diodes at 690 nm and 1087 nm transitions were purchased from Power Technology, Inc. Over the course of the experiment, laser diodes purchased from Lasermate, Inc., Thor Labs, Inc., and Power Technology, Inc. have all been used to supply light for the 984 nm transition. Lasers are tuned to resonance by referencing a High Finesse WS-7 wavemeter purchased from Toptica, Inc.

The lasers are set up to propagate along the axis of the ion trap. In the case of the modified Campbell trap, there is clear optical access axially. In the modified RGA trap, however, axial optical access is obstructed at one end of the trap by a Faraday cup. The Faraday cup is used in the normal operation of the RGA to detect an ion current at the outlet of the mass filter. Incident laser light that is not absorbed by the Th^{3+}ions ultimately scatters off the Faraday cup. The noise thus added to the fluorescence signal of the ions is mitigated somewhat by the presence of a ground shield enclosing the Faraday cup. However, this remains a distinct disadvantage of the modified RGA trap.

An Andor iXon model DV887ECS-UVB camera is used to collect fluorescence from the trapped Th^{3+} ions. The camera features an 8.2 mm $\times$ 8.2 mm back-illuminated CCD sensor with 16 μm square pixels. A thermoelectric cooler maintains the temperature of the CCD at $\leq -50°$C. The quantum efficiencies of the CCD at the wavelengths of the Th^{3+}transitions are $> 90\%$ at 690 nm, $\sim 20\%$ at 984 nm, and $< 1\%$ at 1087 nm. The combination of linewidth and quantum efficiency make optical excitation with the Λ-system and detection of 984 nm fluorescence a favorable strategy.

The iXon has an additional feature that was always used for thorium observation. The pixels on the CCD can be grouped into square, multipixel arrays called *superpixels*. Unlike

binning done in software, this process occurs at device level. The multiple pixels in the superpixel are physically read simultaneously, thereby reducing the number of pixel readouts. This reduces the overall readout noise associated with transferring the image from the CCD. This process can greatly boost the SNR of fluorescence measurements. Typically, the pixels are binned 4×4 into superpixels for observation of thorium.

The Th^{3+}ions are imaged onto the camera using 50 mm diameter achromatic lenses purchased from Edmund Optics. A 75 mm focal length objective and 100 mm focal length imaging lens is used when viewing ions in the modified Campbell trap. In the case of the modified RGA trap, the arrangement of the trap and vacuum system made necessary a slightly longer focal length objective. In all cases, a 984 nm filter is used to limit the light incident on the CCD.

A CCD image of a thermal cloud of $^{232}Th^{3+}$ is shown in Figure 30. For each such image, two camera exposures are taken. The first exposure is taken with the 690 nm light shuttered. Without 690 nm light, ions in the Λ-system manifold are optically pumped back to the $5F_{5/2}$ ground state where they remain without fluorescing. This first exposure, in which fluorescence from ions is absent and only 984 nm scatter remains, is subtracted from the second exposure, which is taken with both 690 nm and 984 nm light incident on the ions. The use of the 984 nm filter in the imaging setup eliminates both 690 nm scatter and fluorescence, so background light levels seen by the CCD remain unchanged whether this laser is on or off. Measurements of total fluorescence are done by summing the counts of each pixel in the region of interest (ROI) shown in Figure 30(b).

Our group demonstrated laser cooling of $^{232}Th^{3+}$ using these optical transitions [35]. However, the experiments described in this chapter did not utilize this technique. Details regarding the laser cooling of Th^{3+} will be presented in the Ph.D thesis of Corey Campbell.

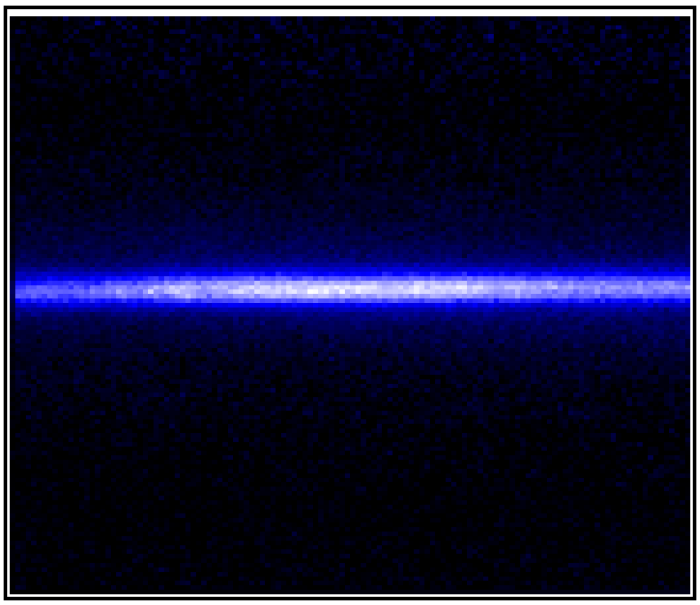

(a)

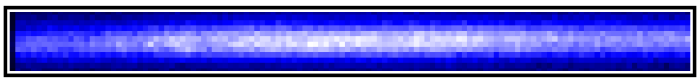

(b)

Figure 30: CCD image of thermal $^{232}Th^{3+}$ ion cloud in the modified Campbell trap. The light collected is from the 984 nm transition. The image was taken with a 1 s exposure. Background scatter from the trap electrodes has been subtracted. Pixels are binned 4×4 into superpixels. (a) The full CCD image. (b) The reduced ROI used when determining total fluorescence.

4.1.4 Channel Electron Multiplier and Mass Selective Detection

Both the modified RGA trap and the modified Campbell trap feature a channel electron multiplier (CEM), which provides a second means of determining whether ions have been trapped. The CEM features a continuous dynode fabricated from a resistive material with high secondary electron emissivity. The dynode is tubular with a hollow cone at its front end [83]. A large voltage is maintained across the length of the dynode with the back end held at ground potential and the front biased at $\sim -2.8\,\mathrm{kV}$. The high negative bias accelerates nearby positive ions toward the entrance of the dynode where they strike the surface and cause the emission of electrons. The field gradient inside the dynode accelerates the emitted electrons through its channel. As these electrons strike the surface of the dynode, they cause the emission of more electrons. The cascade continues, adding more and more electrons, until the electrons finally leave the channel. The electrons are ultimately collected on an anode positioned $\sim 1\,\mathrm{mm}$ from the end of the dynode.

The Burle model 4220 CEM is used in both traps. This model is manufactured specifically for use in Stanford Research Systems' line of residual gas analyzers. The CEM used with the modified RGA trap was the same unit that came pre-installed on the original device. In the case of the modified Campbell trap, a suitable mount was designed and welded to an endplate on the existing trap. A stainless steel cylinder, 0.19" in diameter and $1/2$" long is used as the anode. The CEM and anode are held in the mount with #2-56 set screws. The anode is insulated from the mount and the set screw with Kapton tape.

In both traps, the CEM is located off-axis at one end of the trap. Ions are delivered to the CEM by lowering the voltage of the endcap nearest the CEM to zero. Ions are ejected from the trap by the voltage on the remaining endcap. The high negative bias on the front of the dynode turns the ions toward the CEM where they are detected.

Used in combination with the mass selection techniques outlined in Section 2.3, the CEM can be used to determine if a specific species of ion is present in the trap. The procedure is straightforward. The RF amplitude, V_{rf}, is raised over a period of 100 ms from

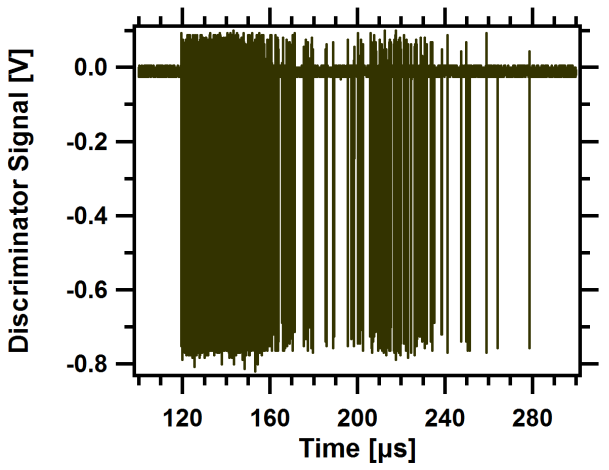

(a)

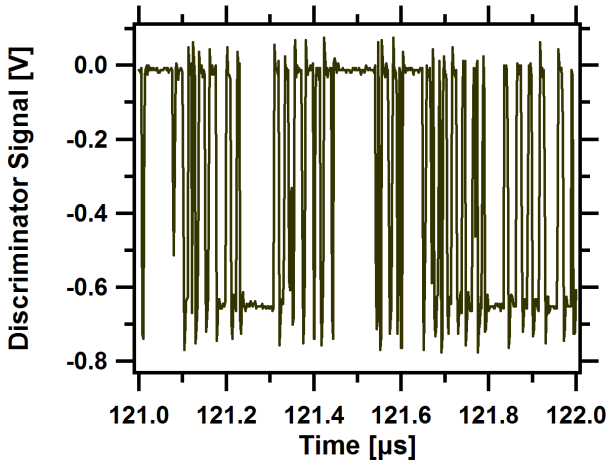

(b)

Figure 31: Discrete CEM signal from ions ejected from modified RGA trap. The anode line of the CEM is connected to the input of an SRS model SR400 photon counter. The discriminator output of the photon counter is then connected to the Agilent DSO6052A oscilloscope from which this data was taken. (a) The complete signal. (b) A zoomed view of part of the signal. The elongated pulses indicate that the ion incidence rate was greater than the bandwidth of the detector.

its normal operating point to a value directly beneath the apex of stability for the ion in question. The value of U_{dc} is then raised to just beneath the apex of stability for a period of 3 ms – which is equivalent to several thousand cycles of the RF trapping field – so that only the species of interest remains stable. The V_{rf} is then returned to its normal operating point, and the contents of the trap are delivered to the CEM. A non-zero signal indicates the presence of the ion species.

A CEM can be operated in either analog or pulse counting mode. Generally, the cascade of electrons arising from an incident ion arrives as a current pulse on the anode line. When operating in pulse counting mode, the output of the CEM anode is connected to a pulse counter, in our case the SR400 from Stanford Research Systems. The SR400 amplifies and shapes the pulses, and then counts them. The discriminator output of the SR400 is then monitored on an Agilent DSO6052A oscilloscope.

Monitoring the discriminator output of the pulse counter is helpful in diagnosing problems with the process. There is a distinct time signature left by pulses caused by ions dumped from the trap. The first pulses arrive $\sim 100\,\mu$s after the voltage on the endcap near the CEM is lowered. As can be seen in Figure 31(a), the bulk of the pulses are tightly grouped and arrive within a short time window. Pulses arising from noise on the anode line or incident background gas molecules, for example, do not leave such a distinguishable pattern.

The CEM is a very sensitive detector. Gains of 10^6 to 10^9 are commonly achieved [101]. However, the CEM does suffer from a limited bandwidth. The width of a single current pulse from the Burle 4220 as observed directly from the anode is ~ 10 ns. If multiple ions arrive within a time interval shorter than the length of a single pulse, individual pulses will not be observed. A rapid succession of ion arrivals can result in a single elongated pulse, which the SR400 records as a single event (see Figure 31(b)).

With the modified RGA trap, these elongated pulses happen infrequently enough so as to have little effect on measurements. They are prevalent, however, when the contents

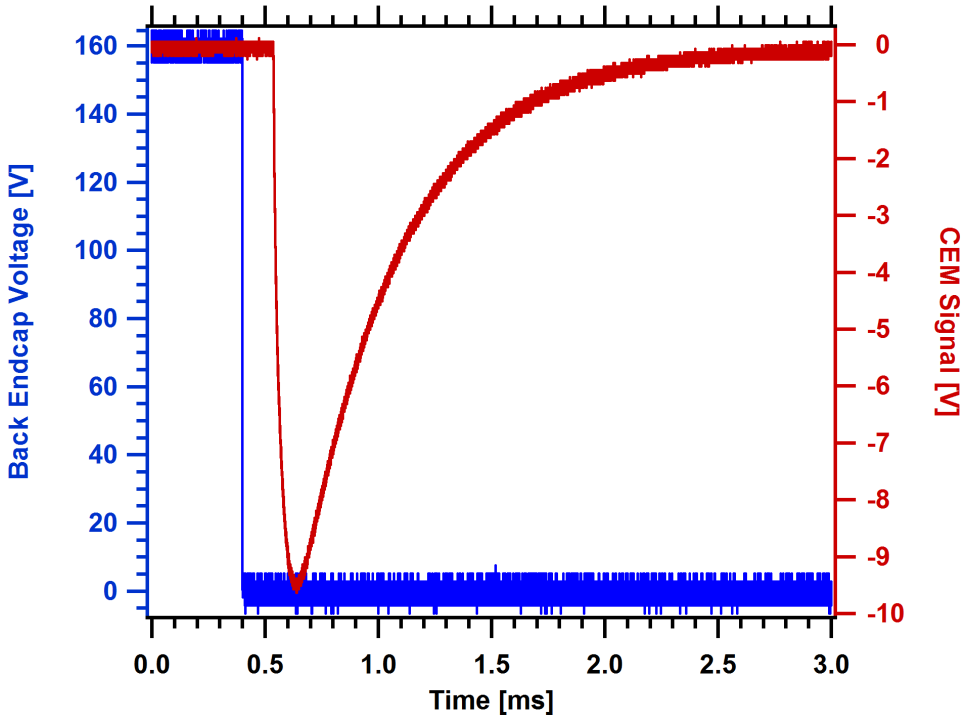

Figure 32: Analog CEM signal from ions ejected from the modifeid Campbell trap. The voltage is measured across a 1 MΩ impedance.

of the modified Campbell trap are counted. This is likely because the substantially larger trapping volume of the Campbell trap is able to hold much higher quantities of ions. For this reason, the analog mode of CEM operation is used with the modified Campbell trap. Figure 32. An example of the analog signal from the modified Campbell trap is shown in Figure 32. The voltage is measured over a 1 MΩ impedance.

The gain of a CEM can vary from ion to ion. Ions with higher charge states experience a greater acceleration in the field created by the high negative bias at the entrance of the dynode. These ions strike the dynode surface with greater energy, resulting in a higher initial emission of electrons [102]. The CEM gain also depends on mass, as lighter ions tend to cause a larger response than more massive ones [83]. The chemical nature of the ion also plays a role [103,104]. For these reasons, the SRS RGA 100 performs a calibration prior to using its CEM for quantitative measurement. The calibration is done for a specific ion by comparing the signal from the CEM to the ion current detected on the Faraday

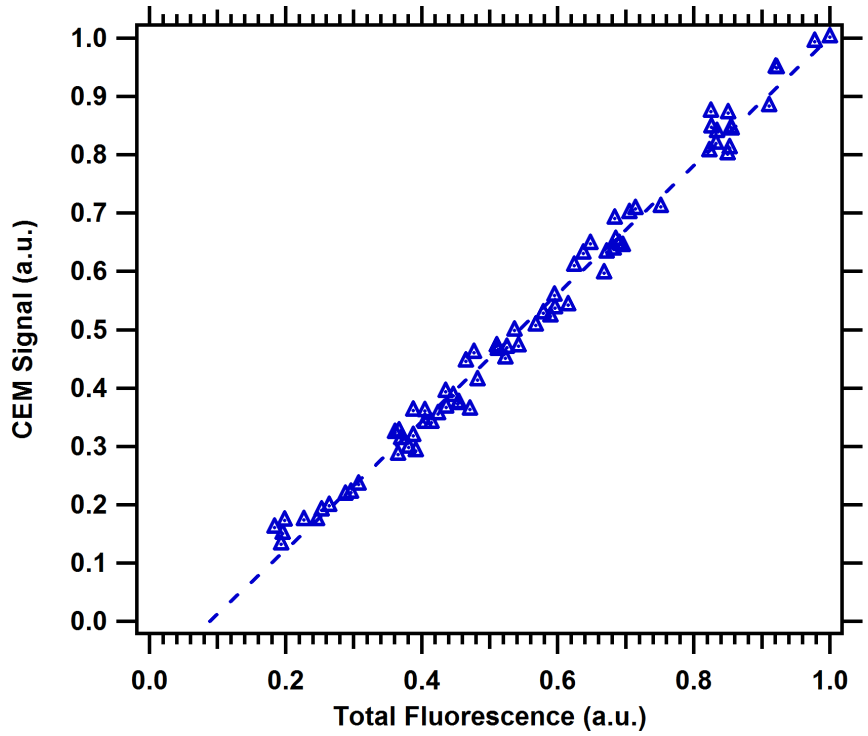

Figure 33: $^{232}Th^{3+}$ CEM signal vs. total fluorescence. The relationship between the two signals is linear over the range of observation. The R^2 value for the linear fit is 0.98892.

cup [83].

In addition, the instantaneous gain of a CEM can be effected by previous ion events. When electrons are emitted from the resistive wall of the dynode, the field inside the channel changes. If two ions impact the CEM in rapid succession, the electrons emitted in the second event will experience a smaller voltage drop in the dynode, leading to lower secondary electron emission.

Despite these limitations, the Th^{3+}CEM signal showed a linear relationship with measurements of total fluorescence from the modified Campbell trap. This relationship was measured several times over a period of days. An example of one such measurement is shown in Figure 33.

4.2 Thorium Ion Generation and Trapping

Both the modified RGA trap and the modified Campbell trap are loaded via laser ablation of a thorium target. Laser ablation has been used in many ion trap experiments [63, 105, 106], as far back as 1981 [107]. The physical mechanisms underlying the ablation process are not completely understood; however, it has proven in many experiments to be an effective means of producing copious quantities of ionized matter from solid targets. The experimental path that led us to laser ablation is covered thoroughly in the Ph.D thesis of Adam Steele [55].

In our experiment, laser ablation proceeds as follows. The third harmonic of a pulsed Nd:YAG laser ($\lambda = 355$ nm) is focused onto a thorium target just outside the trap. The target is located near the trap axis and oriented perpendicular to it. The incident light creates a plasma plume consisting of neutral and ionized thorium and electrons. This plume moves at high velocity (10s of km/s [54, 55]) toward the ion trap. In the case of the modified RGA trap, a large negative bias applied to the focus plate at the end of the trap rods focuses the ions into the trapping region.

In both traps, the endcap nearest the ablation target is gated with the ablation pulse. The voltage on the endcap is lowered to ground to allow ions to enter the trap, and subsequently raised to trap them. The gating process for the modified Campbell trap is shown in Figure 34(a). In this case the voltage on the endcap is gated using a simple transistor circuit. The gate timing is controlled by a model 500 pulse generator from Berkeley Nucleonics Corporation. To minimize jitter between the time of the pulse and the gating of the endcap, the same unit also controls the Nd:YAG laser flashlamps and Q-switch.

The number of ions loaded via laser ablation can vary significantly from shot to shot. The effect of this variation on measurements can be mitigated somewhat by loading with several ablative pulses. Since the duration of the endcap gate is much shorter than a period of axial oscillation in the ion trap, ions already in the trap have insufficient time to escape while the endcap is grounded. Therefore, ions can be accumulated in the trap over multiple

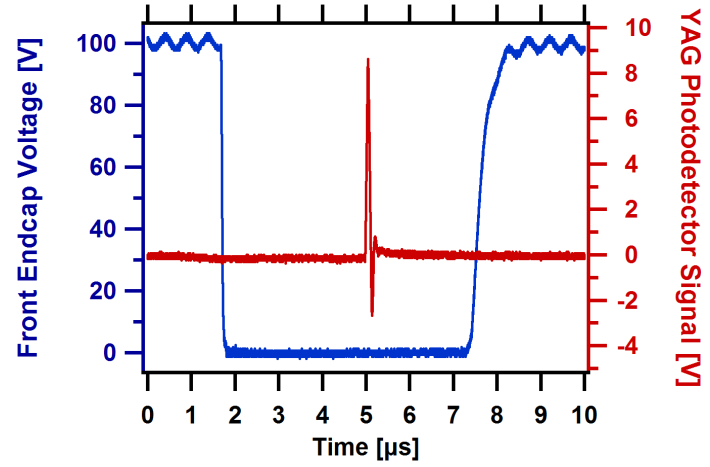

(a)

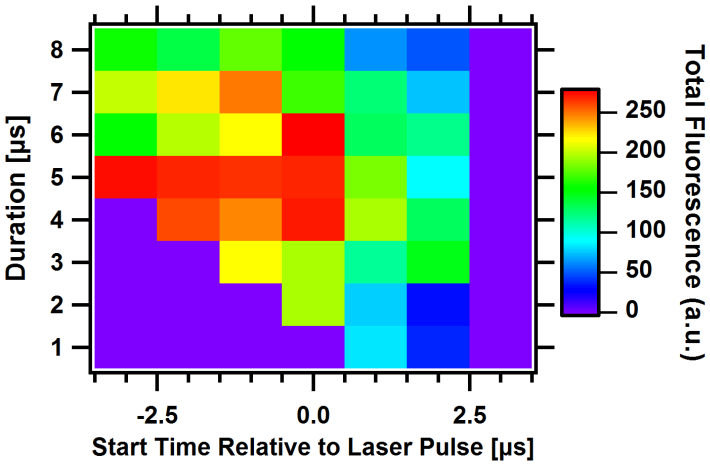

(b)

Figure 34: Front endcap gating for loading ion trap. (a) The endcap voltage and timing sequence represented here was used for loading the modified Campbell trap. (b) Loading of modified Campbell trap as a function of gate time and duration.

cycles of the loading process. However, even when multiple ablative pulses are used, the number of ions loaded can vary significantly. A variance of 20% to 30% between loads is normal.

Helium buffer gas is present in the system throughout the loading process. When the hot Th^{3+} ions collide with room temperature helium atoms, they lose some of their thermal energy. This process serves two critical purposes. First, it reduces the energy of some ablated Th^{3+} ions as they traverse the length of the ion trap, thereby increasing the likelihood they will be trapped. Secondly, it damps the motion of trapped Th^{3+} ions allowing them to come to thermal equilibrium at some fraction of the trap depth. The helium pressure is commonly held between 10^{-5} and 10^{-4} torr in these experiments. Generally, with higher buffer gas pressure, the number of ions loaded increases, and the equilibrium temperature of the trapped ions decreases.

The ablation targets are in the form of thorium metal or thorium nitrate solution dried on a metal substrate. Most of our work has been done using thorium metal as an ablation target. Metal ablation targets are created by cutting small pieces from a thin piece of thorium using tin shears. The thorium metal is in the form of a small square, 25 mm on a side and 1 mm thick, and was purchased from Goodfellow Corporation. Thorium nitrate targets are discussed in detail in Section 4.4.

Our initial work with laser ablation was done with a Thompson-CSF 5000 series Nd:YAG laser generously lent to us by Dr. Walter DeHeer. We subsequently purchased a Minilite II from Continuum, Inc. In each case, the beam out of the laser is resized using a telescope so that it fills a 25 mm diameter lens. The beam is then focused with a short focal length lens (between 75 mm and 150 mm) onto the ablation target. Thor Labs model PF10-03-G01 mirrors are used in the optical setup. These mirrors have a higher damage threshold than the normal dielectric coated mirrors from Thor Labs. However, their reflectivity at 355 nm is only $\sim 80\%$.

The ablation process results in a large plume of charged particles that can short the RF

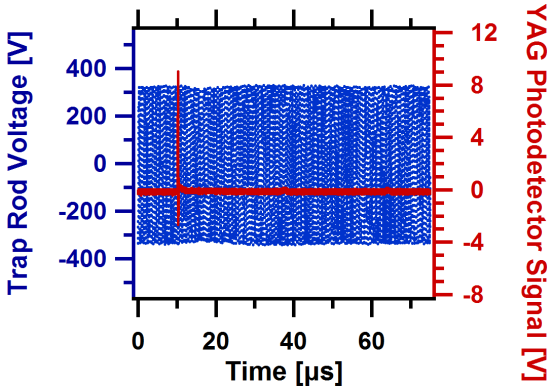

(a)

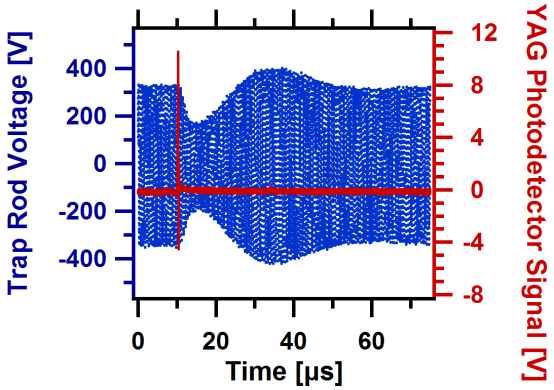

(b)

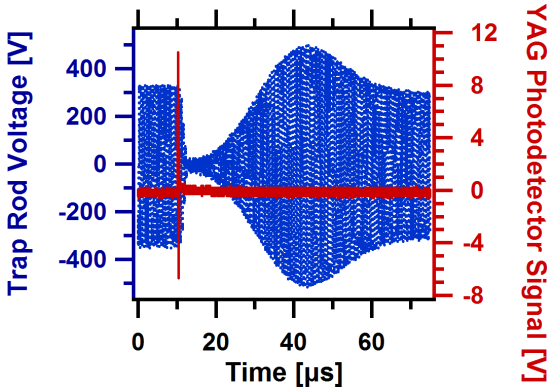

(c)

Figure 35: Shorting of RF trap voltage after ablative pulse. Of (a), (b), and (c), only the shorting in (a) is consistent with Th^{3+}loading in the modified Campbell trap configuration. Optimal loading of the modified RGA trap occurred with shorting levels similar to (b).

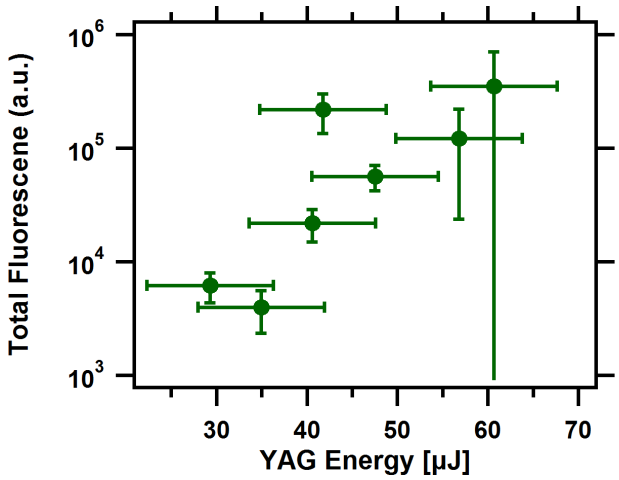

Figure 36: $^{232}Th^{3+}$ loading as a function of pulse energy for the modified Campbell trap. The loading drops swiftly to zero above the optimal loading pulse energy. The pulse energy is measured immediately after the final focusing lens.

potential on the rods of the trap. This is shown in Figure 35. The focusing lens of the Nd:YAG beam is initially optimized by maximizing the amount of shorting observed for a given pulse energy. Once the lens is in position, the pulse energy of the laser is adjusted to maximize Th^{3+} loading. Subsequent adjustments of the laser pulse energy are done by recreating the amount of shorting observed when Th^{3+} loading is maximized.

With the modified Campbell trap, the maximum Th^{3+} loading occurs where trap shorting is visible, but at a minimum, as in Figure 35(a). At higher laser pulse energies, Th^{3+} loading drops steeply to zero (see Figure 36). Since there is no radial trapping field when the RF is shorted, it would be reasonable to expect that RF shorting must always be kept to a minimum for effective trapping. However, optimal loading in the RGA trap is accompanied by a moderate amount of shorting, like that of Figure 35(b). Generally, the optimal level of RF shorting for loading Th^{3+} depends on the specific trap and target configuration.

For loading the modified RGA trap, the RF amplitude of the trapping potential is set so that $q = 0.705$ for Th^{3+}. The quality of loading in the modified Campbell trap depends strongly on the RF amplitude. This can be seen in Figure 37. Loading of the Campbell trap is typically done with $q = 0.591$.

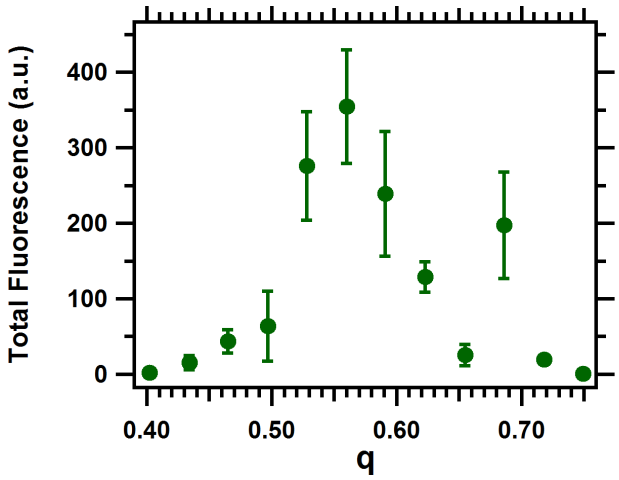

Figure 37: $^{232}Th^{3+}$ loading as a function of trap RF amplitude for the modified Campbell trap. The q value represented on the horizontal axis is that of $^{232}Th^{3+}$.

4.3 Spectroscopy of $^{232}Th^{3+}$

Observation of fluorescence from trapped Th^{3+} ions was first accomplished in the modified RGA trap. The resonant frequencies for the 690 nm and 984 nm transitions were found by conducting a two-dimensional search. Several spectra, similar to the one shown in Figure 38, were taken [55].

The process of taking spectra is automated using LabView. The program tunes the lasers stepwise through user-defined frequency ranges by controlling the voltage applied to the PZTs of the laser gratings. The wavemeter mentioned in Section 4.1.3 is used as a frequency reference in the tuning process. At each step, the program determines an error offset for the wavemeter by referencing it to a frequency-locked rubidium laser.

At each point in the frequency space, the program performs a number of operations. First, it loads the ion trap by firing the ablation laser between 10 and 20 times. After executing the mass selective technique described in Section 4.1.4 to ensure only Th^{3+} remains in the trap, the program triggers the camera to take an image of the ions. The ions are then delivered to the CEM for counting. If the number of ions is smaller than a preset threshold value, the preceding operations are repeated at the same laser detunings. The fluorescence signal is ultimately normalized according to the number of ions present in the trap when

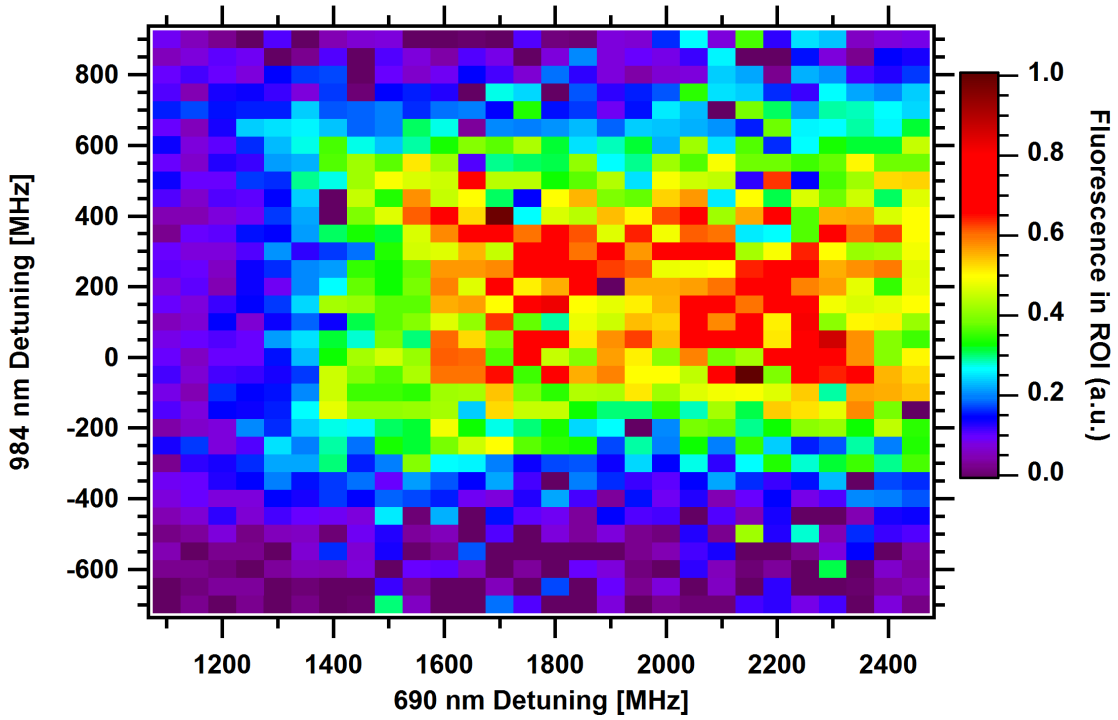

Figure 38: Spectroscopy of $^{232}Th^{3+}$ lambda system. Detunings are given from the value published by Klinkenberg [36].

the image was taken.

The spectrum in Figure 38 was taken with 3×10^{-5} torr of helium buffer gas present in the system. The temperature of the trapped ions can be estimated by comparing the widths of the two transitions to the formula for the FWHM of a Doppler-broadened atomic resonance [100]:

$$2\delta = 2\omega_0 \sqrt{\frac{2k_B T \ln 2}{mc^2}}. \tag{44}$$

A two-dimensional Gaussian fit of the spectrum reveals the FWHM linewidths of the 690 nm and 984 nm transitions to be 1160 MHz and 860 MHz respectively. In accordance with Eq. (44), the ratio of the Doppler-broadened linewidths is approximately equal to the inverse ratio of the linewidths. These linewidths correspond to an ion temperature of ~ 3200 K.

The temperature calculated above reflects only the ion motion in the dimension of laser propagation. Since the lasers are oriented on the axis of the trap, this method measures

the axial motion of the ions. The temperature of the ions in the radial dimension is higher due to the RF driven micromotion in this dimension. Doppler-broadening with transverse optical excitation is normally on the order of several GHz at typical buffer gas pressures.

In the process of performing these laser frequency scans, the spatial distribution of the ion fluorescence along the trap axis was found to vary with laser detuning. The images of Figure 39 show this phenomenon. The distribution is modeled mathematically by summing pixels vertically and fitting the result to the equation

$$f(x) = y_0 + A \exp\left\{-\frac{(x - \overline{x} - x_0)^2}{2w^2}\right\} + B \exp\left\{-\frac{(x - \overline{x} + x_0)^2}{2w^2}\right\}. \tag{45}$$

Here, $\overline{x}$ is the center position of the fluorescence distribution, and $2x_0$ represents the separation between the two regions of fluorescence. The separation as a function of 690 nm detuning is shown in Figure 40.

A similar effect was reported by Gudjons, et al. [108] for singly-ionized calcium in a three-dimensional Paul trap. Just as in our experiment, optical excitation of the calcium ions was between energy levels of a Λ-system, and the ions were collisionally cooled with helium buffer gas. The group noted that when one of the excitation lasers is detuned, only those ions that are Doppler-shifted into resonance with the incident light will fluoresce. Since RF micromotion is the dominant velocity component of ion motion, it must be responsible for the Doppler shift that allows the ions to be resonant with the detuned laser. In a linear Paul trap, the amplitude of an ion's micromotion in the dimensions of RF confinement scales linearly with the ion's displacement from the center of the trap (Eq. (25)). This relationship holds in all dimensions in a three-dimensional Paul trap. Thus, as a laser is detuned from the atomic resonance, only those ions a sufficient distance from the trap center will fluoresce.

In the linear Paul trap, micromotion in the axial dimension is typically neglected. However, as mentioned in Section 2.2, the presence of the endcap electrodes introduces an axial component to the RF field, and with that comes micromotion in the axial dimension. Furthermore, the amplitude of the axial micromotion is higher as one moves from the center

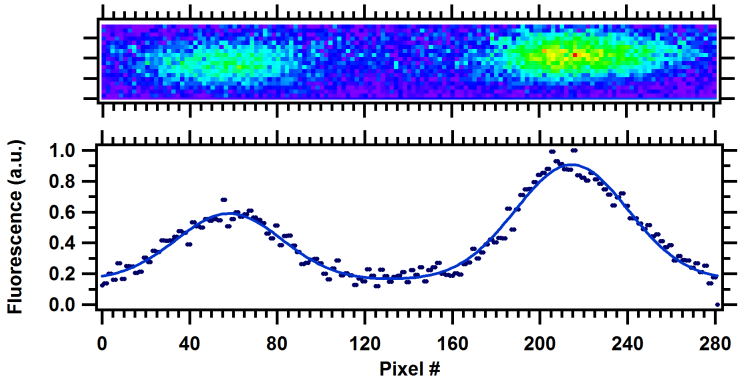

(a)

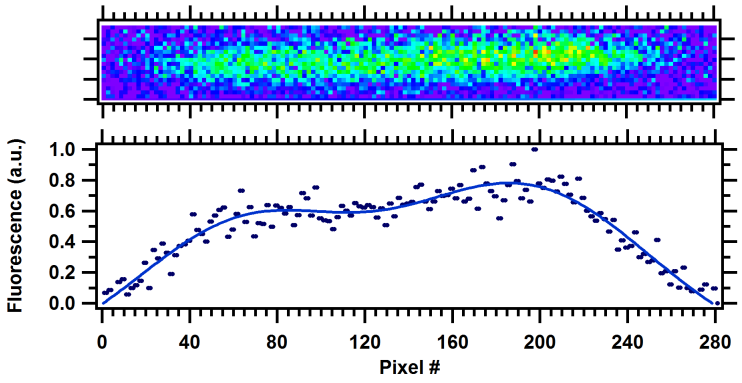

(b)

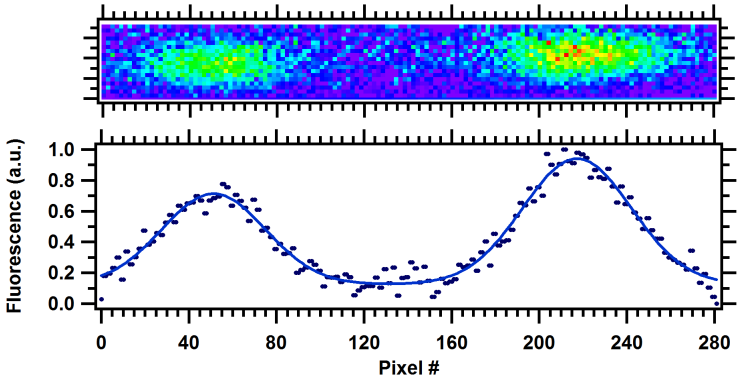

(c)

Figure 39: Spatial distribution of $^{232}Th^{3+}$ fluorescence. For all images, the 984 nm laser was on resonance. The detuning of the 690 nm laser from resonance was (a) −400 MHz, (b) 0 MHz, and (c) 400 MHz. The graphs below each image are produced by summing pixels vertically and fitting to Eq. (45).

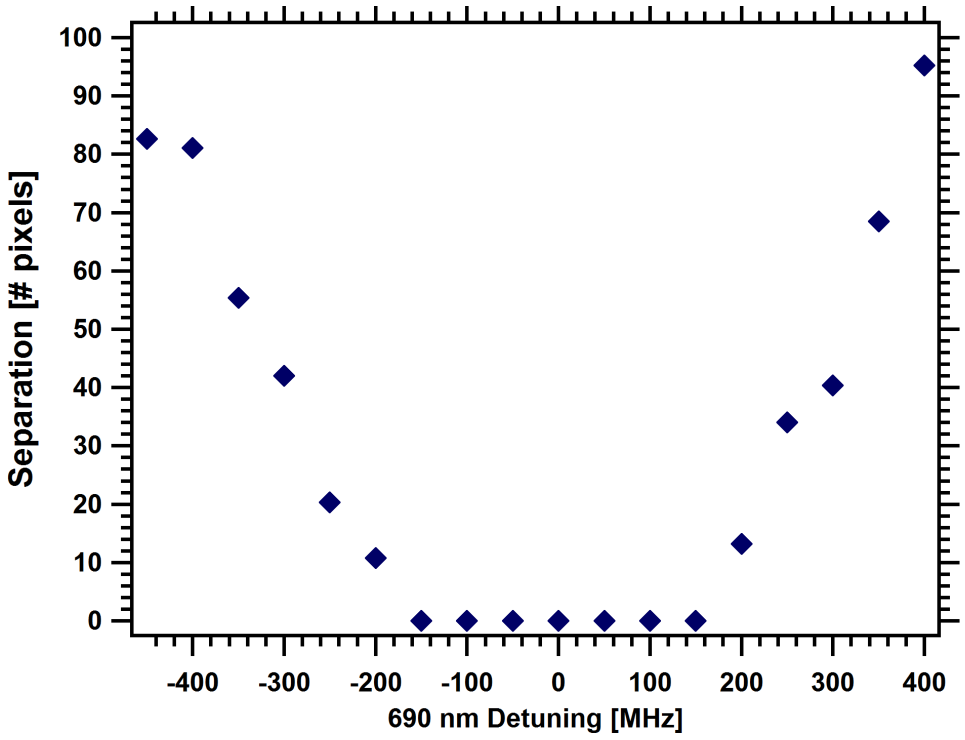

Figure 40: Spatial distribution of $^{232}Th^{3+}$ fluorescence vs. detuning.

of the trap toward the endcaps [86]. This is consistent with the effect as seen in the linear trap.

This phenomenon has been observed in both the modified RGA trap and the modified Campbell trap. All of the data presented here shows how the spatial distribution varies with respect to the detuning of the 690 nm laser, but the effect can be seen by detuning either of the excitation lasers. The laser with the largest detuning determines the minimum velocity amplitude necessary for resonance. [108].

4.4 Thorium Nitrate Sources

All thorium nuclei decay via either alpha or beta radiation. With a half-life of 14 billion years, only the ^{232}Th isotope is readily found in nature. The ^{232}Th isotope can be obtained relatively easily and inexpensively in a number of forms, including as a solid metal.

The ^{229}Th isotope, on the other hand, is incredibly rare and very expensive. According to a fact sheet from the Idaho National Laboratory (INL) [109], there is a total of ~ 140 g of

Figure 41: ^{229}Th nitrate sample obtained from Oak Ridge National Laboratory. The ^{229}Th nitrate is the yellow residue at the bottom of the vial. It contains 100 μg of the ^{229}Th isotope. This sample cost $12,225.

^{229}Th in the United States. Most of this small quantity is dispersed throughout metric tons of uranium-233 (^{233}U) waste, which is housed at INL and Oak Ridge National Laboratory (ORNL). The ^{229}Th arises as a result of the alpha decay of ^{233}U, which has a half-life of 160,000 years [110]. Only a small fraction of the ^{229}Th has actually been extracted from the ^{233}U stockpile [109, 111].

We were able to obtain 100 μg of ^{229}Th in the form of a thorium nitrate compound, $^{229}Th(NO_3)_4$, from ORNL Isotope Sales. A picture of the sample is shown in Figure 41. The price of this sample was $12,225. This amounts to a cost for ^{229}Th of over $100,000/mg.

Prior to making the significant investment in the ^{229}Th sample, we conducted a test to determine if Th^{3+} could in fact be loaded via ablation of trace quantities of thorium nitrate. For this purpose, we purchased 25 g of ^{232}Th nitrate tetrahydrate ($^{232}Th(NO_3)_4 \cdot 4H_2O$) from Spectrum Chemical Corporation. Unlike anhydrous thorium nitrate, which is yellow, thorium nitrate tetrahydrate is a white, crystalline powder. As of this writing, the list price for this quantity of ^{232}Th nitrate tetrahydrate is $385.20, or $\sim$ 3¢/mg.

Both ^{232}Th and ^{229}Th are radioactive alpha emitters. The decay chains for ^{232}Th and ^{229}Th are given in Tables 3 and 4, respectively. Special precautions must be taken when handling the thorium nitrate to prevent inhalation and ingestion of the material or contamination of the surrounding work areas. This is especially true in the case of ^{229}Th, which

has a specific activity nearly 2,000,000 times greater than that of ^{232}Th. The recoil energy from the alpha decay of either isotope is sufficient to eject the daughter nuclide from the sample and onto surrounding surfaces. Over a period of weeks, a vacuum viewport that was located near one of our ^{229}Th samples became heavily contaminated as a result of this process.

With help from the Georgia Tech Office of Radiation Safety (ORS), we developed a protocol for the safe handling of our radiological samples. All work with the radioisotopes is done inside a fume hood. Handling of the ^{229}Th is further confined to within a glove bag and is done only under the active supervision of a member of ORS. A lab coat and two pairs of latex or nitrile gloves are worn when working with the radioisotopes. The inner pair of gloves is taped to the sleeves of the lab coat to ensure no area on the arms is exposed. The outer pair of gloves is changed frequently to prevent the potential spread of contamination. All personnel who work in lab areas where radiological samples are kept are trained as radiation workers. Those who handle the ^{229}Th are equipped with radiation badges and rings to measure exposure.

After work with the radioisotopes is complete and all sample containers are sealed, the work area and any tools used in the process are thoroughly frisked with a geiger counter. Alpha and beta samples are collected by rubbing the tools and work area with small pieces of filter paper. These samples, or *smears*, are collected in an envelope and taken to ORS for counting. All solid and liquid waste is disposed of in designated containers. When not in use, the ^{229}Th sample is kept in a secure location at ORS.

The UHV systems in which the samples are ultimately placed are actively pumped by a turbomolecular pump backed by a dry scroll pump. The pump is far removed from the sample, and there is no direct line of sight between them. Nevertheless, alpha and beta smears of the scroll pump exhaust and surrounding areas are done on a weekly basis. Additional smears are also taken on various surfaces of the lab space as a precautionary measure.

Table 3: The decay chain of ^{232}Th. Data compiled from NuDat 2.5 [110]. P_α and P_β are the branching ratios to alpha and beta decay, respectively. $\langle N_\gamma \rangle$ is the average number of subsequent gamma emissions per alpha or beta decay, and $\langle E_\gamma \rangle$ is the average *total* energy emitted via subsequent gamma decay. Energies are given in keV.

Nuclide	Daughter(s)	Half-Life	P_α	$\langle E_\alpha \rangle$	P_β	$\langle E_\beta \rangle$	$\langle N_\gamma \rangle$	$\langle E_\gamma \rangle$
^{232}Th	^{228}Ra	1.4×10^{10} yr	1.0	4003	–	–	0.074	1
^{228}Ra	^{228}Ac	5.75 yr	–	–	1.0	7	0.029	0
^{228}Ac	^{228}Th	6.15 hr	–	–	1.0	353	1.513	861
^{228}Th	^{224}Ra	1.912 yr	1.0	5406	–	–	0.106	3
^{224}Ra	^{220}Rn	3.66 days	1.0	5673	–	–	0.049	10
^{220}Rn	^{216}Po	55.6 s	1.0	6288	–	–	0	0
^{216}Po	^{212}Pb	0.145 s	1.0	6788	–	–	0	0
^{212}Pb	^{212}Bi	10.64 hr	–	–	1.0	100	0.967	144
^{212}Bi	^{212}Po, ^{208}Tl	60.55 min	0.360	2175	0.641	494	0.201	104
^{212}Po	^{208}Pb	299 ns	1.0	8785	–	–	0	0
^{208}Tl	^{208}Pb	3.053 min	–	–	1.0	560	2.405	3380
^{208}Pb	–	**STABLE**						

Table 4: The decay chain of ^{229}Th. Data compiled from NuDat 2.5 [110]. P_α and P_β are the branching ratios to alpha and beta decay, respectively. $\langle N_\gamma \rangle$ is the average number of subsequent gamma emissions per alpha or beta decay, and $\langle E_\gamma \rangle$ is the average *total* energy emitted via subsequent gamma decay. Energies are given in keV.

Nuclide	Daughter(s)	Half-Life	P_α	$\langle E_\alpha \rangle$	P_β	$\langle E_\beta \rangle$	$\langle N_\gamma \rangle$	$\langle E_\gamma \rangle$
^{229}Th	^{225}Ra	7880 yr	1.0	4921	–	–	1.485	89
^{225}Ra	^{225}Ac	14.9 days	–	–	1.0	97	0.438	14
^{225}Ac	^{221}Fr	10.0 days	1.0	5788	–	–	0.305	14
^{221}Fr	^{217}At	4.9 min	1.0	6359	–	–	0.167	29
^{217}At	^{213}Bi	0.032 s	1.0	7063	–	–	0.001	0
^{213}Bi	^{213}Po, ^{209}Tl	45.59 min	0.021	122	0.975	424	0.325	126
^{213}Po	^{209}Pb	4.2 μs	1.0	8376	–	–	0.005	0
^{209}Tl	^{209}Pb	2.2 min	–	–	1.0	655	3.119	2138
^{209}Pb	^{209}Bi	3.25 hr	–	–	1.0	198	0	0
^{209}Bi	–	**STABLE**						

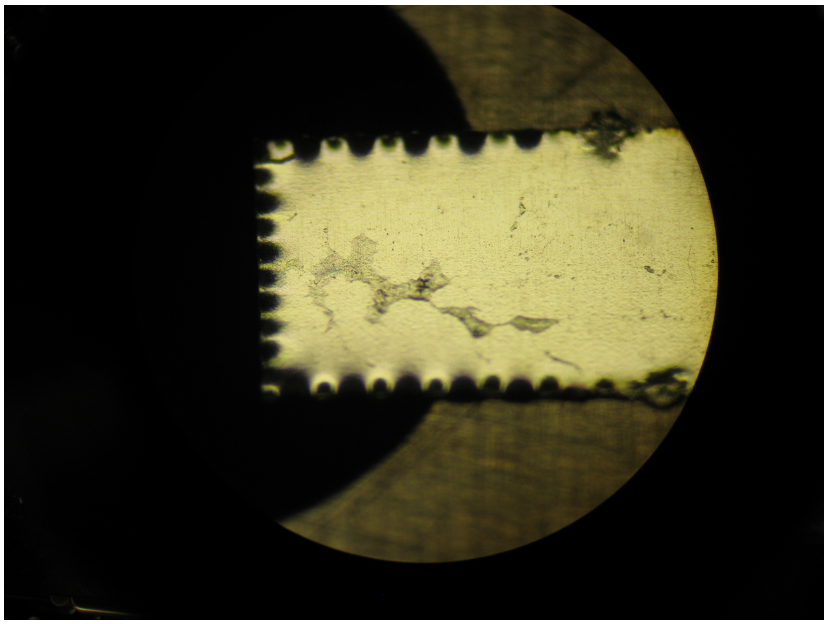

Figure 42: Thorium nitrate sample on stainless steel substrate. The sample is created by drying a small drop of thorium nitrate solution on the substrate. Some crystallization of the thorium nitrate can be seen. Although it does not appear in the image, a thin film covered the entire area where the droplet was placed. The substrate is ~ 3 mm wide. Picture taken by C. Campbell.

In general, thorium nitrate ablation targets are made by preparing a thorium nitrate solution and drying a small droplet of it on a metal substrate. An example of a thorium nitrate target is shown in Figure 42. To determine the feasibility of performing our experiment with only a small amount of thorium nitrate, we produced a target with $\sim 10\,\mu$g of the compound for testing. To do this, we dissolved 9 mg of ^{232}Th nitrate tetrahydrate in 35 mL of distilled water. Using a disposable pipette, a small drop of approximately $50\,\mu$L of the solution was placed on a stainless steel substrate and dried overnight in the fume hood. The substrate was cut from 0.003" stainless steel shim stock. After drying, a thin, white film covered the area where the droplet had been placed. In some denser areas, crystalline structures, similar in texture to the original powder, had formed.

The target was placed approximately 1" from the end of the modified RGA trap. At the time, the setup of the system prevented observation of Th^{3+} fluorescence, so mass selective CEM detection was used to measure the loading. The Nd:YAG laser was focused to a

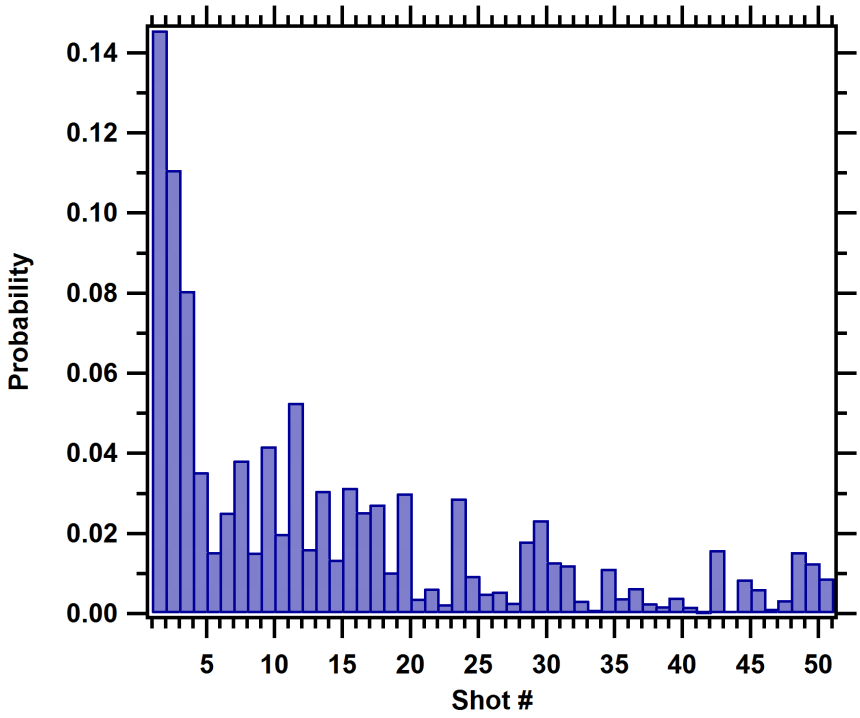

Figure 43: Probability distribution of loading Th^{3+} from a single position on a thorium nitrate target.

$\sim 10\,\mu$m spot size on the target. The pulse energy used was $\sim 100\,\mu$J. The ablation laser was directed onto the sample via a Thor Labs VM1 mirror mount, which has graduated knobs for adjusting the mirror angle. The graduated knobs allowed us to carefully map the positions on the target that were ablated. At each position, the ablation laser was fired 50 times, and the number of Th^{3+} ions loaded with each individual shot was recorded. To obtain an accurate sampling, the position of the laser was varied over multiple regions of the target. Over the course of the experiment, $\sim 1\%$ of the target surface was ablated. Quantities of Th^{3+} ions sufficient for spectroscopy were detected 80 times.

A single position on thorium metal can be ablated for weeks without it becoming necessary to change the position of the laser on the target. However, since the thorium nitrate forms a very thin residue over the surface of the substrate, the probability of loading from a single position on the target decays with the number of ablative pulses. This is shown in Figure 43.

Table 5: Assay of Georgia Tech ^{229}Th sample. The assay was performed on March 10, 2009 by Dr. Saed Mirzadeh of Oak Ridge National Laboratory. The total mass of thorium in the original sample was 132.2 μg.

Radioisotope	**Mass**	γ**-activity (%)**
^{229}Th	100.0 μg (75.6%)	21.3 μCi (> 99.5%)
^{228}Th	–	< 0.1 μCi (< 0.5%)
^{230}Th	0.63 μg (0.48%)	–
^{232}Th	31.6 μg (23.9%)	–

Without conclusive identification via observation of laser-induced fluorescence, there can be some doubt that the ions detected were in fact $^{232}Th^{3+}$. The mass selection criteria utilized in the measurement were calibrated against $^{232}Th^{3+}$ loaded from a metal target and, based on the theoretical stability diagram, they had an uncertainty of ±5 amu/e. All attempts at loading from areas of the substrate where thorium nitrate was not present yielded negative results. The results are further supported by an independent verification of Th^{3+} loading from a thorium nitrate target by Corey Campbell in a new trap of his design [112]. Campbell observed the Th^{3+} with laser-induced fluorescence.

The ^{229}Th was purchased from ORNL. The ^{229}Th nitrate was delivered to us in a 1 mL polypropylene vial, housed within a lead cylinder, which, in turn, was contained within a metal can. Upon arrival, ORS did a thorough inspection of the container and packaging materials to ensure there was no contamination. The assay of the original sample is reproduced in Table 5.

The ^{229}Th sample was made into a solution. On the advice of the radiochemist who prepared the ^{229}Th sample [113], 0.1 M nitric acid was used as a solvent instead of distilled water. The acidity of the solvent helps prevent molecules of the radionuclide from adsorbing to the surface of the vessel in which the solution is contained. Using a high-precision model XL 3000i digital pipettor from Denville Scientific, Inc., 200 μL of nitric acid was added to the vial containing the ^{229}Th. The solution was agitated by carefully drawing the solution into the pipette tip and expelling it back into the container. Model P2101-N

200 μL pipette tips from Denville Scientific were used for this procedure. There was no visible retention of the sample in the pipette tip at the conclusion of the procedure.

At the same time and in the same fashion, two new ^{232}Th nitrate solutions were made. One solution was made at the same thorium concentration as that of the ^{229}Th nitrate solution, while the other was made at ten times that concentration. Two ablation targets were made from each of the three thorium nitrate solutions. Each target was made by depositing 20 μL of the given solution on a substrate made of aluminum 6061. Deposition was done with the aforementioned high-precision pipettor. The 20 μL droplet represented 10 μg of ^{229}Th on two targets, 10 μg of ^{232}Th on two targets, and 100 μg of ^{232}Th on two targets. The targets are shown in Figure 28(d).

The use of aluminum as a substrate was another recommendation from the radiochemist who prepared our ^{229}Th sample [113]. Aluminum does not react with nitric acid. The aluminum substrates are 9/16" long, 1/8" wide, and 1/16" thick. Each substrate has a thru-slot at one end that allows it to be secured to a mounting apparatus with #0-80 bolts. Prior to the deposition, the substrates were all secured to the mounting assembly that would ultimately hold the targets in the vacuum system. The mounting assembly was, in turn, secured to a small optical breadboard such that the target sides of the substrates were oriented upward. Use of the mounting assembly in the deposition process made individual handling of the small substrates after deposition unnecessary. Having a stable structure to hold the substrates is important, as it allows two hands to be used in handling the pipettor during deposition.

The targets were dried overnight in the fume hood. The mounting assembly was attached to a linear translator inside the vacuum system of the modified Campbell trap. The linear system allowed each target in turn to be positioned for loading. The targets were approximately 3/8" from the end of the trap.

Efforts to load Th^{3+} into the modified Campbell trap from the nitrate samples were ultimately unsuccessful. We were able to demonstrate loading of Th^{+} from both the high

and low concentration ^{232}Th nitrate samples. No Th^{2+} was detected from either sample. The Th^{+} exhibited a similar decay in loading as that shown in Figure 43. The largest quantities of Th^{+} loaded from the high concentration sample were comparable to quantities typically loaded from the ^{232}Th metal. However, this does not necessarily indicate that the same number of Th^{+} ions are created by ablation of each of the samples. The loading of Th^{+}, whether from metal or nitrate, may only be limited by the volume of the trap. If significantly fewer ions are created in the ablation of nitrate than in the ablation of metal, it may not be detectable in terms of the quantities of Th^{+} trapped. Even if that were not the case, there is no reason to believe that the ratio of Th^{3+} ions to Th^{+} ions in an ablation plasma are generally the same for metal and nitrate targets.

No conclusive reason can be given why neither Th^{2+} nor Th^{3+} were loaded into the modified Campbell trap from the nitrate samples. Comparable Nd:YAG pulse energies and focuses were used in both successful demonstrations and the unsuccessful attempt. Differences between the two successful demonstrations of Th^{3+} loading from nitrate and the unsuccessful attempt are recorded here for future investigation. The first difference between the various attempts is the substrate material. Like the targets from which loading was unsuccessful, the target substrate in Campbell's successful attempt was made of aluminum. However, Campbell's substrate was cut from 99.99% pure aluminum stock, while the unsuccessful targets were made of 6061 aluminum alloy. Furthermore, Campbell's aluminum substrate, like the original stainless steel substrate, was cut from rolled metal stock, which has a smooth, lustrous surface. The aluminum 6061 substrates, on the other hand, have machined surfaces. These differences in material and surface quality may have affected how the thorium nitrate residue adhered to the surface after drying. They may also affect the way energy from the ablation pulse is distributed over the target or affect the number of electrons emitted from the surface during ablation. If interactions between emitted electrons and thorium in the ablation plasma are responsible for the ionization of the latter, the use of a substrate that emits fewer electrons in the ablation process may not allow for the

creation of higher charge states.

The second difference between the two successful demonstrations of Th^{3+} loading from nitrate and the unsuccessful attempt is in the length of the trap used. The rods of the modified RGA trap are 4" (101.6 mm) long, and the rods of the current Campbell trap are 174 mm long. The rods of the modified Campbell trap, on the other hand, are only 37 mm long. In Figure 12 of Section 2.1.3, we see that by scaling the length of the modified Campbell trap by a factor of 1.5, we could reduce the axial secular frequency of the trap by a factor of $\sim$ 10. The modified RGA trap and the current Campbell trap are 2.7 and 4.7 times as long as the modified Campbell trap, respectively. Therefore, the axial secular frequencies in those traps should be lower still. The reduced axial secular frequency affords a longer period of interaction between the helium buffer gas and the Th^{3+} ions as they first pass through the trapping region. This likely increases Th^{3+} loading efficiency. One could compensate for the reduced interaction time in the modified Campbell trap by a corresponding increase in the pressure of helium buffer gas. However, with the modified Campbell trap, we already typically operate near the maximum helium pressure allowed by our vacuum and pumping system. Raising the pressure by the order of magnitude or more that may be required is not feasible in this system.

CHAPTER V

$^{232}TH^{3+}$ CHARGE EXCHANGE AND CHEMICAL REACTIONS

In our earliest observations of $^{232}Th^{3+}$, the ions would remain in the trap for only a few seconds. This is in stark contrast to singly-ionized barium, which can remain in an ion trap for long periods (> 1 day), even without laser cooling. The loss of Th^{3+} from the ion trap is due primarily to charge exchange and chemical reactions with background gases. With higher purity buffer gas and improved vacuum conditions, we were able to extend the trap lifetime of Th^{3+} to minutes. By removing the buffer gas immediately after the initial trap loading and laser cooling the ions, a lifetime of $\gtrsim$ 10 minutes was obtained [35].

This limited lifetime presents a significant challenge in time-intensive experiments like measuring the hyperfine states of $^{229}Th^{3+}$ and searching for the nuclear isomer transition. Furthermore, the short lifetime represents a tremendous cost in performing experiments with $^{229}Th^{3+}$ given the extraordinary price of the isotope (>\$100,000/mg).

To better understand the charge exchange and chemical reaction processes, we conducted a series of experiments to determine the reaction rate coefficients between Th^{3+} and various gases. A summary of the experimental results can be found in Table 6. We found that reactions of Th^{3+} with carbon dioxide, methane, and oxygen all occur near the classical rate limit, while reaction rates with argon, hydrogen, and nitrogen are orders of magnitude lower. Reactions of $Th^{3+}$with oxygen and methane were found to proceed primarily via charge exchange, while simultaneous charge exchange and chemical reaction occurs between Th^{3+} and carbon dioxide. Loss rates of Th^{3+} in helium and neon gases are consistent with reaction with impurities in the respective gases. Reaction rates of Th^{3+} with nitrogen and argon depend on the internal electronic configuration of the Th^{3+}. The remainder of this section is devoted to explaining these experiments in greater detail. These experiments

were conducted using the modified Campbell trap.

We begin by considering the loss rate of Th^{3+} in the presence of helium buffer gas. This is shown in Figure 44. Helium is a noble gas and a charge exchange reaction between it and Th^{3+} would be endothermic by 4.6 eV[1]. Therefore, it is likely that the loss shown in Figure 44 is due to an impurity in the helium rather than to the helium itself[2]. Nevertheless, the example will serve to illustrate the concepts that follow. The helium gas we use in our experiment comes from a cylinder with a built-in purifier (BIP). The BIP helium is supplied by Airgas, Inc. More will be said regarding buffer gas impurities later in the chapter.

The exponential decay rate of the trapped Th^{3+} is measured in one of two ways. The first method employs the mass selective detection described in Section 4.1.4. We load ions into the trap via ablation, wait for some amount of time, perform a mass selection of Th^{3+}, and then deliver the Th^{3+} in the trap to the CEM. The time interval before the mass selection varies, and the data is accumulated over several iterations through all of the various wait times. Many iterations are required to suppress the variation due to the fluctuations in the ablative loading. This method is typically used when the Th^{3+} lifetime is a few seconds or less. An example of such a measurement is shown in Figure 45.

The second method for measuring the Th^{3+} decay rate is to observe the reduction of fluorescence over a series of images. This is the preferred method when the lifetime of the ions is sufficient to allow enough fluorescence measurements for a proper exponential fit. Since the measurements are taken on a single group of ions, this method eliminates variance arising from ablative loading. This method was used to acquire the Th^{3+} loss rate in helium shown in Figure 44.

The decay rate through any given reaction channel is proportional to the density of the reactant in the system. This relation can be written as $\tau^{-1} = kn$, where n is the density of

[1] Tables containing relevant ionization energies and polarizabilities are found in Appendix A.
[2] A table containing the specifications of the gases used can also be found in Appendix A.

Table 6: Charge exchange and chemical reaction rate coefficients for $^{232}Th^{3+}$. Reaction rate coefficients are given in units of cm^3s^{-1}. Here, k_L is the calculated Langevin rate, and k is the experimental reaction rate coefficient. The corrected reaction rate coefficient is $k_\epsilon = \epsilon \cdot k$, where ϵ is the ion gauge correction factor for the gas in question. Experimental reaction rate coefficients for helium and neon are upper bounds. The accuracy of the coefficients given here is limited by the accuracy of the ion gauge used to measure the pressure of the reactants. $(*)$ The reaction rate depends on the electronic configuration of Th^{3+}. The experimental rate refers to reaction from the $5F_{5/2}$ ground state.

Reactant	k	k_ϵ	(ϵ)	k_L
$Ar^{(*)}$	1.3×10^{-14}	1.7×10^{-14}	(1.3)	1.5×10^{-9}
CH_4	2.6×10^{-9}	3.6×10^{-9}	(1.4)	2.8×10^{-9}
CO_2	2.8×10^{-9}	4.0×10^{-9}	(1.4)	1.8×10^{-9}
H_2	4.6×10^{-13}	2.1×10^{-13}	(0.46)	4.4×10^{-9}
He	$< 3.4 \times 10^{-15}$	$< 6.0 \times 10^{-16}$	(0.18)	1.6×10^{-9}
$N_2^{(*)}$	1.6×10^{-13}	1.6×10^{-13}	(1.0)	1.8×10^{-9}
Ne	$< 4.1 \times 10^{-15}$	$< 1.2 \times 10^{-15}$	(0.30)	1.0×10^{-9}
O_2	3.7×10^{-9}	3.7×10^{-9}	(1.0)	1.7×10^{-9}

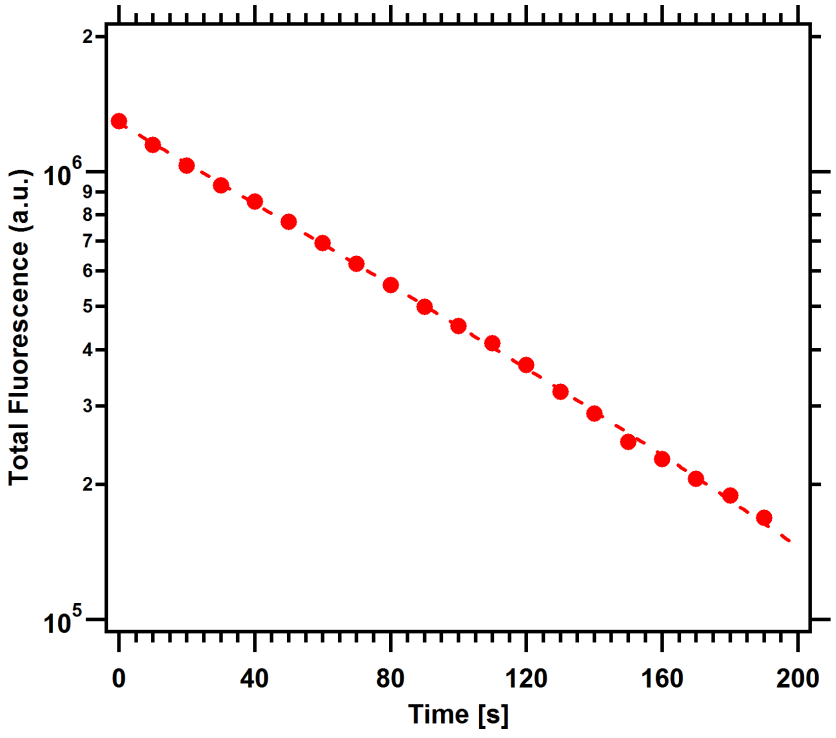

Figure 44: Accumulated fluorescence signal for determination of $^{232}Th^{3+}$ loss rate. This data was taken with 5×10^{-5} torr of BIP helium in the vacuum chamber. The loss rate was determined to be $\tau^{-1} = 0.0100(2)\,s^{-1}$.

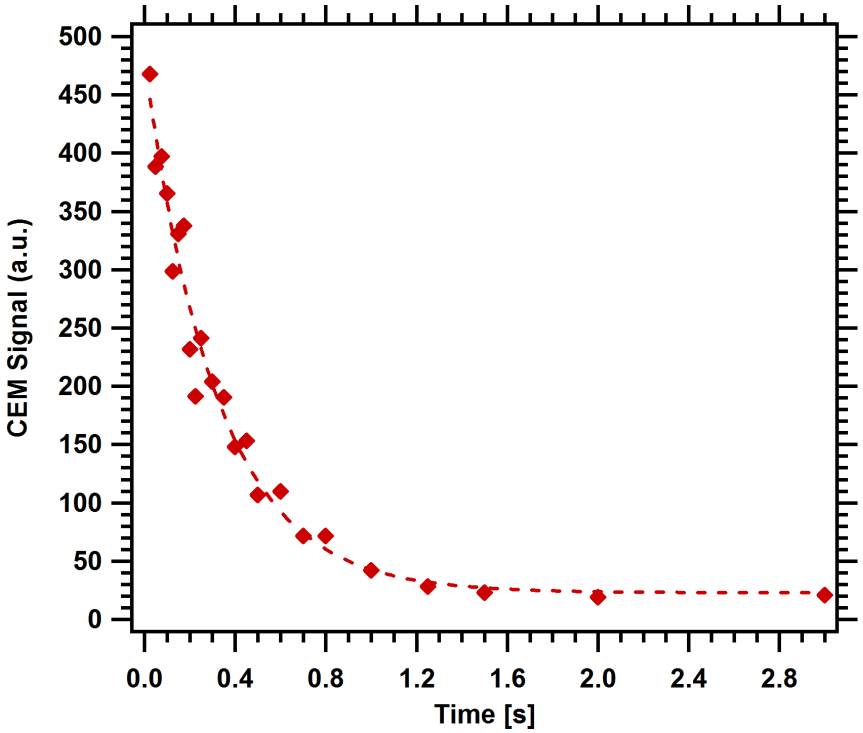

Figure 45: Accumulated CEM signal for determination of $^{232}Th^{3+}$ loss rate. This data was taken with 3×10^{-8} torr of methane in the vacuum chamber. Each data point is the sum of 12 independent measurements. The loss rate was determined to be $\tau^{-1} = 3.1(3)\,s^{-1}$.

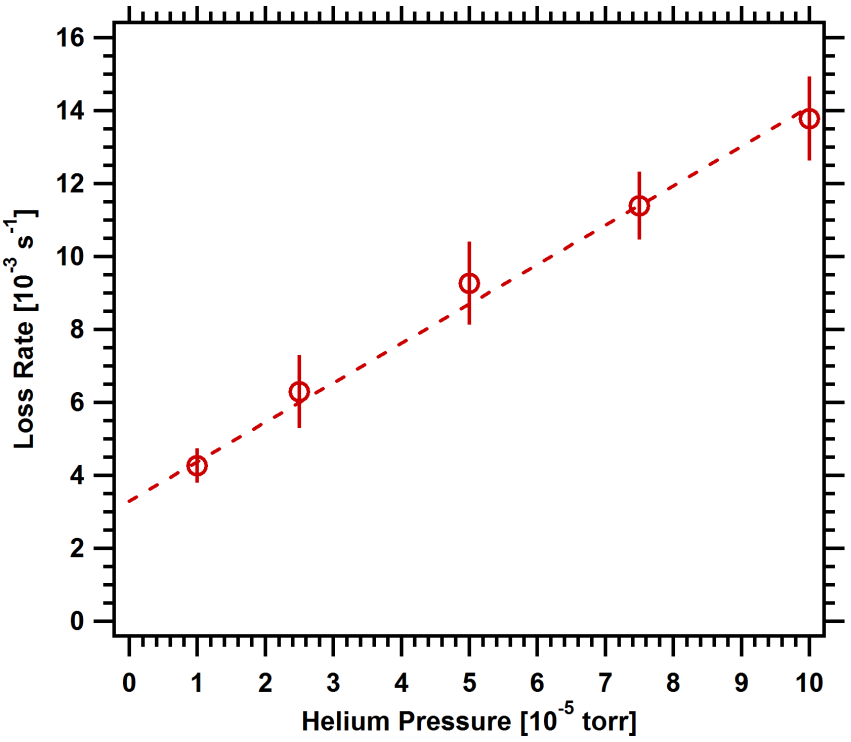

Figure 46: $^{232}Th^{3+}$ loss rate as a function of BIP helium buffer gas pressure. The slope of the linear fit implies a reaction rate coefficient of $k = 3.4 \times 10^{-15}\,\mathrm{cm^3 s^{-1}}$ ($k_\epsilon = 6.0 \times 10^{-16}\,\mathrm{cm^3 s^{-1}}$ with an ion gauge correction factor of $\epsilon = 0.18$), while the intercept implies a background loss rate of $\tau^{-1} = 3.3 \times 10^{-3}\,\mathrm{s^{-1}}$. It is likely that the Th^{3+} reacts with an impurity in the helium rather than with the helium itself; therefore, the value for k sets an upper bound on the reaction rate coefficient for helium.

the reactant, and

$$k \equiv \langle \sigma v \rangle \tag{46}$$

is the reaction rate coefficient for the given channel. Here, σ is the reaction cross-section and v is the relative velocity between the reactants. For a given reaction, the rate coefficient can be determined by measuring the Th^{3+} decay rate as a function of the pressure of the reactive gas. The reaction rate coefficient is extracted from the slope of a linear fit of this data. The intercept of the linear fit gives the loss rate due to background gases in the vacuum. For BIP helium, the data and corresponding linear fit are shown in Figure 46.

A classical collision model introduced by Langevin [114] and refined by Gioumousis and Stevenson [115] is helpful in estimating the reaction cross-sections between ions and molecules. We assume the ion is a point particle with charge Ze, and that the molecule is

spherically symmetric[3] with polarizability α. The primary interaction between the ion and molecule is due to the electric field of the ion and the field-induced dipole moment of the molecule. The interaction potential scales as $1/r^4$.

For certain values of the relative velocity and the impact parameter, the interaction potential leads to a spiraling orbit of the ion and molecule about their shared center of mass. If a reaction between the ion and molecule is exothermic, it is assumed to occur with unit probability when a spiraling orbit occurs. The so-called Langevin cross-section for reaction is then [115]

$$\sigma_L = 2\pi \frac{Ze}{v} \sqrt{\frac{\alpha}{\mu}}, \tag{47}$$

where v is the relative velocity between the particles and μ is the reduced mass. The corresponding reaction rate coefficient is simply

$$k_L = \langle \sigma_L v \rangle = 2\pi Ze \sqrt{\frac{\alpha}{\mu}}. \tag{48}$$

The preceding equations are given in gaussian units, which is how they are most commonly found in the literature. For a singly-charged ion, k_L is typically on the order of 10^{-9} cm^{3}s^{-1}.

This model has several shortcomings. First, it treats only spherically-symmetric, non-polar molecules. If the molecule possesses a permanent dipole moment, the leading term in the interaction potential scales as $1/r^2$ rather than as $1/r^4$ [116]. Furthermore, several experiments [117–119] have shown a departure from the inverse velocity dependence of the classical cross-section in some reactions. Ultimately, the probability of a reaction occurring in the event of a classical interaction is dependent on the combined energy state of the reactants, the available energy states in the final products, and the possible reaction pathways between them [120]. Several experiments [121–125], including our own, have found that some reaction rates can differ significantly depending on the internal energy state of a reactant.

[3] In this context, *spherically symmetric* refers specifically to the polarizability of the molecule. The term also implies that the molecule has no permanent dipole moment.

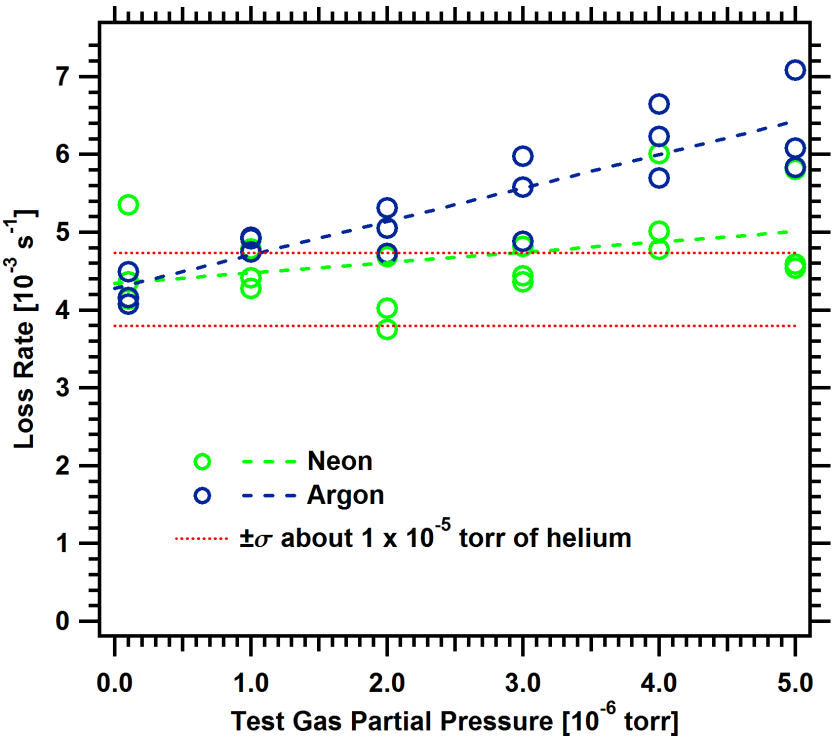

Figure 47: $^{232}Th^{3+}$ loss rate in the presence of neon and argon. A partial pressure of 10^{-5} torr of helium was added to the test gas to cool the ions for fluorescence observation. The reaction rate coefficient for neon is $k = 4.1 \times 10^{-15}\,cm^3s^{-1}$ ($k_\epsilon = 1.2 \times 10^{-15}\,cm^3s^{-1}$ with an ion gauge correction factor of $\epsilon = 0.30$). The decay rates shown for argon represent Th^{3+} loss from the $5F_{5/2}$ ground state. The reaction rate coefficient is $k = 1.3 \times 10^{-14}\,cm^3s^{-1}$ ($k_\epsilon = 1.7 \times 10^{-14}\,cm^3s^{-1}$ with an ion gauge correction factor of $\epsilon = 1.3$).

Nevertheless, the Langevin rate is useful in setting an upper bound on the reaction rate between ions and non-polar molecules [126]. Many ion-molecule reactions do occur at or near the Langevin rate [122,127–130]. The Langevin rates for the reactions we investigated are given in Table 6 with the experimental results.

In light of our discussion of Langevin rates, let us return to the case of the BIP helium buffer gas. The data of Figure 46 implies a reaction rate coefficient between Th^{3+} and the BIP helium on the order of 10^{-16} to $10^{-15}\,cm^3s^{-1}$. Assume for a moment that the reaction occurring is not between Th^{3+} and helium, but between Th^{3+} and some contaminant in the helium. If the reaction between Th^{3+} and the contaminant in question occurs at the Langevin rate, it would imply an impurity of 0.1 to 1 ppm, which is only slightly above the specifications for the BIP helium. However, one must also consider the possibility that

additional contaminants are added to the helium in the gas handling apparatus connecting the helium cylinder to the leak valve. Because of these factors, the reaction rate coefficient can only give an upper limit on the rate of reaction between the Th^{3+} and helium. The difference in electron affinity between helium and Th^{3+} suggests the reaction rate between them is, in fact, zero.

Loss rates of Th^{3+} in the presence of neon and argon are shown in Figure 47, while loss rates in the presence of nitrogen and hydrogen are shown in Figure 48. For all of these decay measurements, a partial pressure of 10^{-5} torr of helium was added to cool the ions for fluorescence imaging. As can be seen from Figure 46, this quantity of helium does not add significantly to the background loss rate of Th^{3+}. The reactions with argon, nitrogen, and hydrogen all proceed relatively slowly, with reaction rate coefficients orders of magnitude below the corresponding Langevin rates. Since our interest was in gases that react quickly with Th^{3+}, we did not attempt to identify the products of these reactions.

Like helium, neon is a noble gas with a high ionization energy that would inhibit charge exchange reactions with Th^{3+}. As can be seen in Figure 47, Th^{3+} loss rates in neon were never significantly larger than what could be attributed to the presence of the helium buffer gas. In addition, the reaction rate coefficient we determined from the data is consistent with reaction occurring between the Th^{3+} and a $\sim$ 0.5 ppm carbon dioxide, oxygen, or hydrocarbon impurity in the gas. For these reasons, the coefficient can be considered an upper bound on the reaction rate between Th^{3+} and neon.

Argon is also a noble gas, but a charge exchange reaction between it and Th^{3+} is exothermic by 4.2 eV. The Th^{3+} reaction rates with argon and nitrogen were found to depend on the electronic configuration of the Th^{3+}. The data in Figures 47 and 48 represent loss rates out of the $5F_{5/2}$ ground state of Th^{3+}. The $5F_{5/2}$ state was isolated for study by shuttering the 690 nm laser between fluorescence measurements. This allows Th^{3+} in the Λ-system manifold to be pumped back into the ground state by the 984 nm laser. By keeping the time

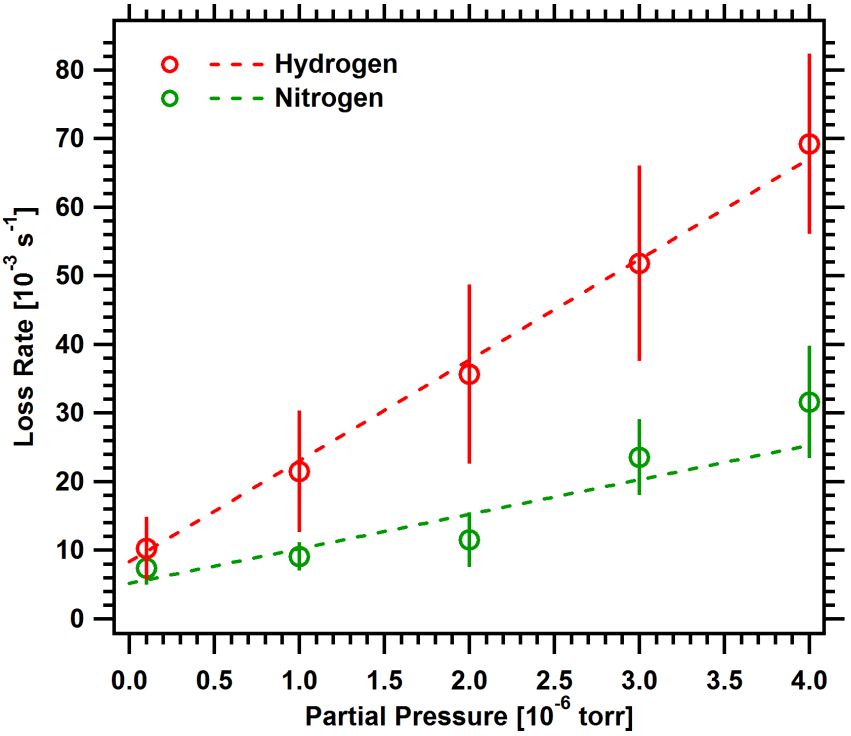

Figure 48: $^{232}Th^{3+}$ loss rate in the presence of hydrogen and nitrogen. A partial pressure of 10^{-5} torr of helium was added to the test gas to cool the ions for fluorescence observation. The reaction rate coefficient for hydrogen is $k = 4.6\times10^{-13}$ cm^{3}s^{-1} ($k_\epsilon = 2.1\times10^{-13}$ cm^{3}s^{-1} with an ion gauge correction factor of $\epsilon = 0.46$). The decay rates shown for nitrogen represent Th^{3+} loss from the $5F_{5/2}$ ground state. The reaction rate coefficient is $k = 1.6\times10^{-13}$ cm^{3}s^{-1}.

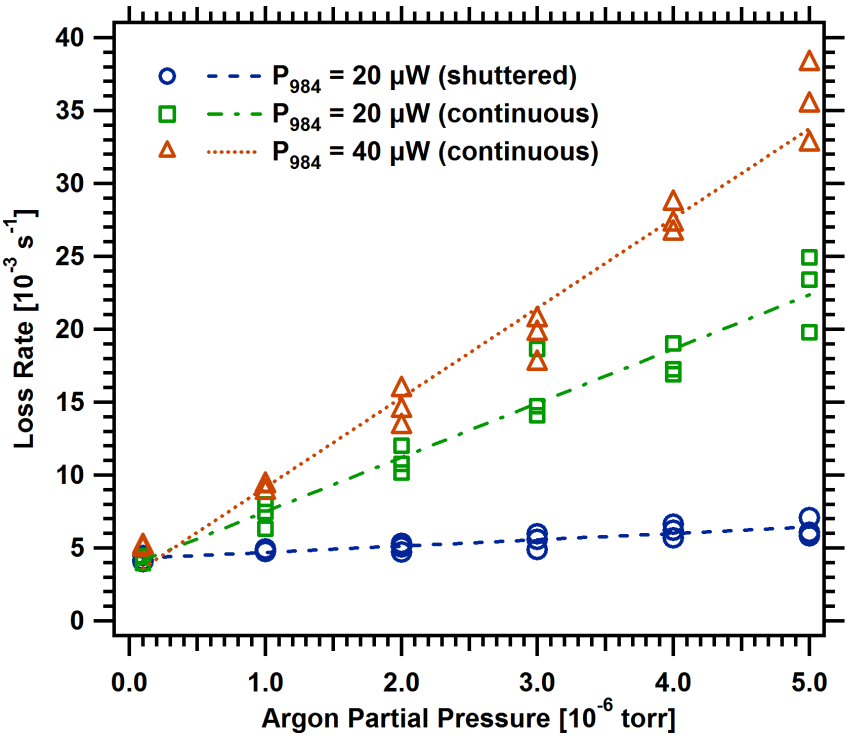

Figure 49: Effect of atomic excitation on $^{232}Th^{3+}$ loss rate in the presence of argon. The data that was taken by shuttering the 690 nm laser represents loss from the Th^{3+} $5F_{5/2}$ ground state. The same data is shown in Figure 47. Increasing the power of the 984 nm laser increases the reaction rate by increasing the number of ions in the $6D_{5/2}$ excited state, from which reaction is more likely.

between measurements sufficiently long, the systematic effect introduced during measurement was held below 10%.

The effect of Th^{3+} optical excitation on its reaction rate with argon can be seen clearly in Figure 49. In one set of measurements, the 690 nm laser was shuttered between fluorescence measurements. This is the same data as shown in Figure 47. In the other two sets of measurements, the 690 nm laser was left on continuously. Increasing the power of the 984 nm laser increases the number of ions occupying the $6D_{5/2}$ excited state, and hence the reaction rate, until the excited state is saturated. The corresponding saturation of the argon reaction rate is shown in Figure 50. The saturation of the nitrogen reaction rate is shown for two different values of 690 nm laser power in Figure 51.

If the $5F_{7/2} - 6D_{5/2}$ manifold is approximated as a two-level system, the excited state

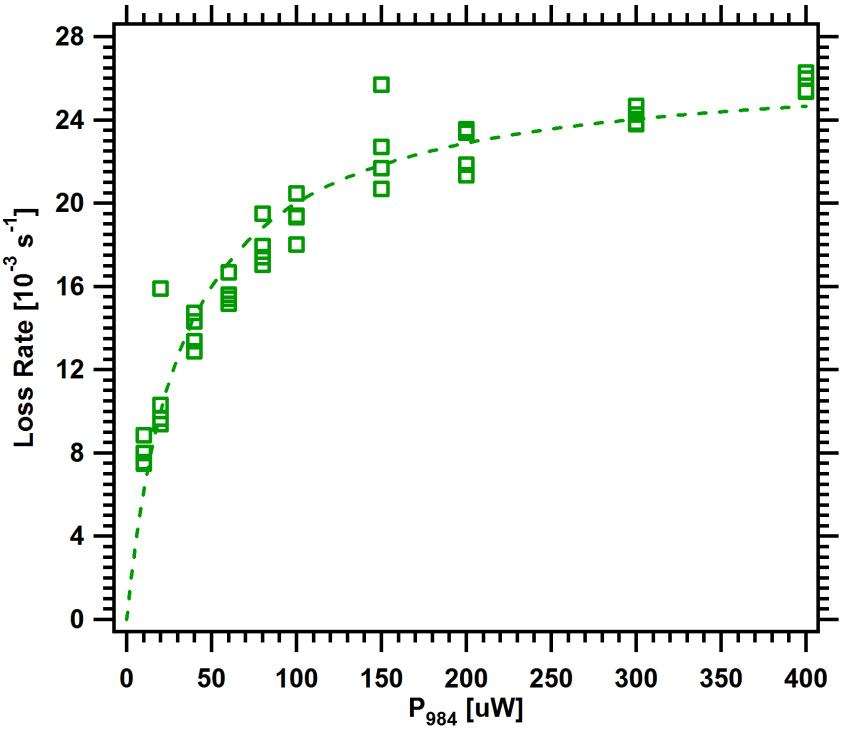

Figure 50: Saturation of $^{232}Th^{3+}$ reaction rate with argon. The fit function is in the form of Eq. (49).

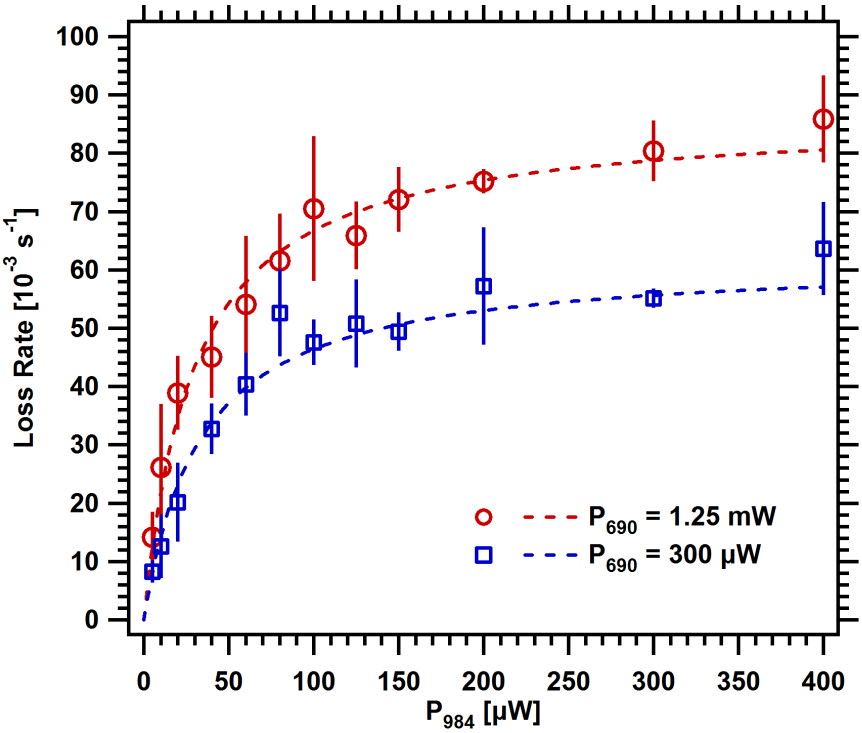

Figure 51: Saturation of $^{232}Th^{3+}$ reaction rate with nitrogen. The fit functions are in the form of Eq. (49).

population obeys the relation

$$\sigma \propto \frac{I/I_{\text{sat,eff}}}{1 + I/I_{\text{sat,eff}}}, \tag{49}$$

where $I_{\text{sat,eff}}$ is the effective saturation intensity. The ratio of the effective saturation intensity to the natural saturation intensity, $I_{\text{sat}} = 2\pi^2 hc\Gamma/3\lambda^3$, is approximately equal to the ratio of the Doppler-broadened linewidth, Γ_{Doppler}, to the natural linewidth, Γ. Therefore,

$$I_{\text{sat,eff}} \approx \frac{2\pi^2 hc}{3\lambda^3}\Gamma_{\text{Doppler}}. \tag{50}$$

By fitting the data in Figures 50 and 51 to a function in the form of Eq. (49), and considering the beam spot size of $\sim 300\,\mu$m, we find an effective saturation intensity of $I_{\text{sat,eff}} \sim 40\,\text{mW/cm}^2$. This result is consistent with what would be expected from Eq. (50) for a Doppler-broadened linewidth, $\Gamma_{\text{Doppler}} \sim 300\,\text{MHz}$.

The reaction rate out of the $5F_{7/2}$ electronic state was found to be equal to the reaction rate from the $5F_{5/2}$ state to within experimental error. The $5F_{7/2}$ state was isolated by shuttering the 984 nm laser between measurements instead of the 690 nm laser. In this way, the Th^{3+} ions were pumped into the long-lived $5F_{7/2}$ state ($\tau = 1.07\,\text{s}$ [99]). The 690 nm laser is left on during the measurement to continuously repopulate the state. To further demonstrate that optical excitation to the $6D_{5/2}$ was responsible for the increased reaction rates, we verified that detuning the lasers far from resonance had the same effect as shuttering them.

By optically exciting with the 1087 nm laser, we found that reactions with nitrogen were also faster from the $6D_{3/2}$ state than from the $5F_{5/2}$ state. No quantitative comparisons were made between the reaction rates from the $6D_{3/2}$ state and the $6D_{5/2}$ state. The reaction rate between Th^{3+} and argon with 1087 nm optical excitation was not measured.

Loss rates of Th^{3+} in the presence of carbon dioxide, methane, and oxygen are shown in Figures 52, 53, and 54, respectively. All of these gases react very quickly with Th^{3+}. Even at relatively low pressures, reactions occurring between the ablation target and the trap significantly reduced the number of Th^{3+} ions loaded. To ensure sufficient loading and

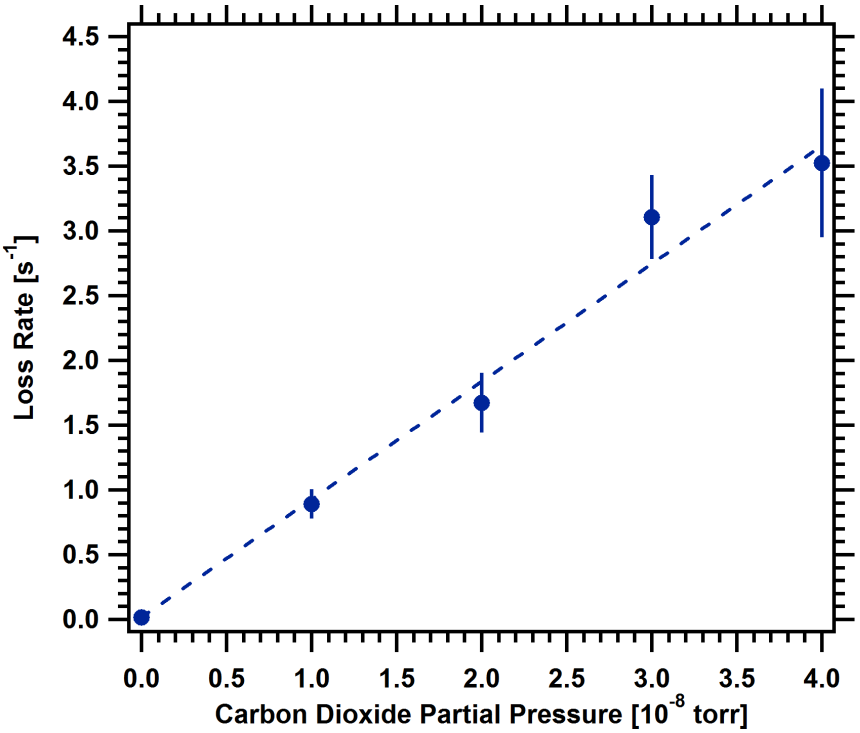

Figure 52: $^{232}Th^{3+}$ loss rate in the presence of carbon dioxide. Measurements were made with 10^{-4} torr of helium buffer gas. The data point at zero pressure is the loss rate when only helium at 10^{-4} torr is present. The reaction rate coefficient for carbon dioxide with Th^{3+} is $k = 2.8 \times 10^{-9}\,cm^3s^{-1}$ ($k_\epsilon = 4.0 \times 10^{-9}\,cm^3s^{-1}$ with an ion gauge correction factor of $\epsilon = 1.4$).

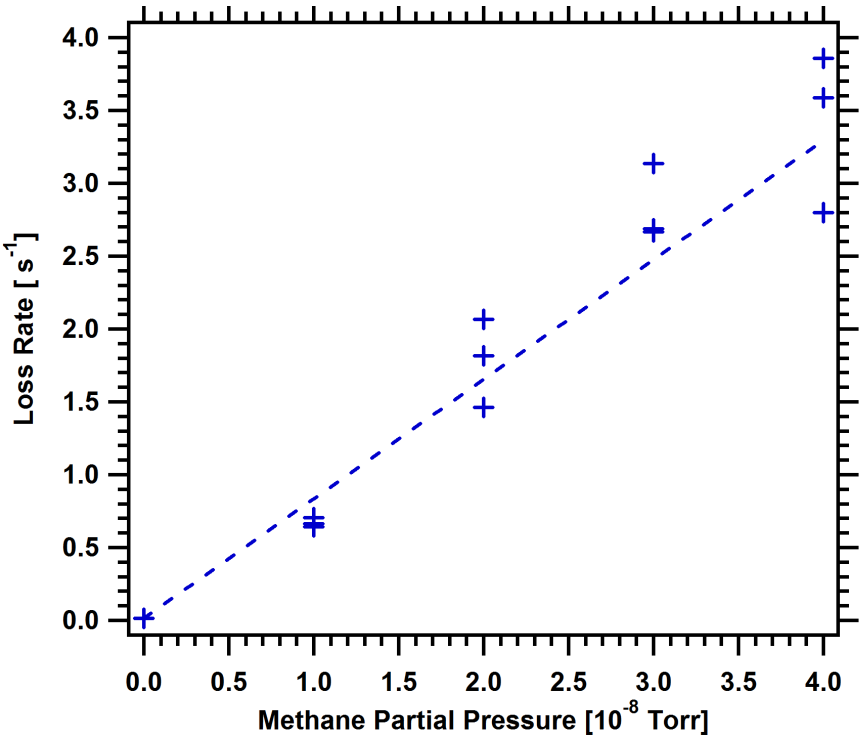

Figure 53: $^{232}Th^{3+}$ loss rate in the presence of methane. Measurements were made with 10^{-4} torr of helium buffer gas. The data point at zero pressure is the loss rate when only helium at 10^{-4} torr is present. The reaction rate coefficient for methane with Th^{3+} is $k = 2.6 \times 10^{-9}\,\mathrm{cm^3 s^{-1}}$ ($k_\epsilon = 3.6 \times 10^{-9}\,\mathrm{cm^3 s^{-1}}$ with an ion gauge correction factor of $\epsilon = 1.4$.

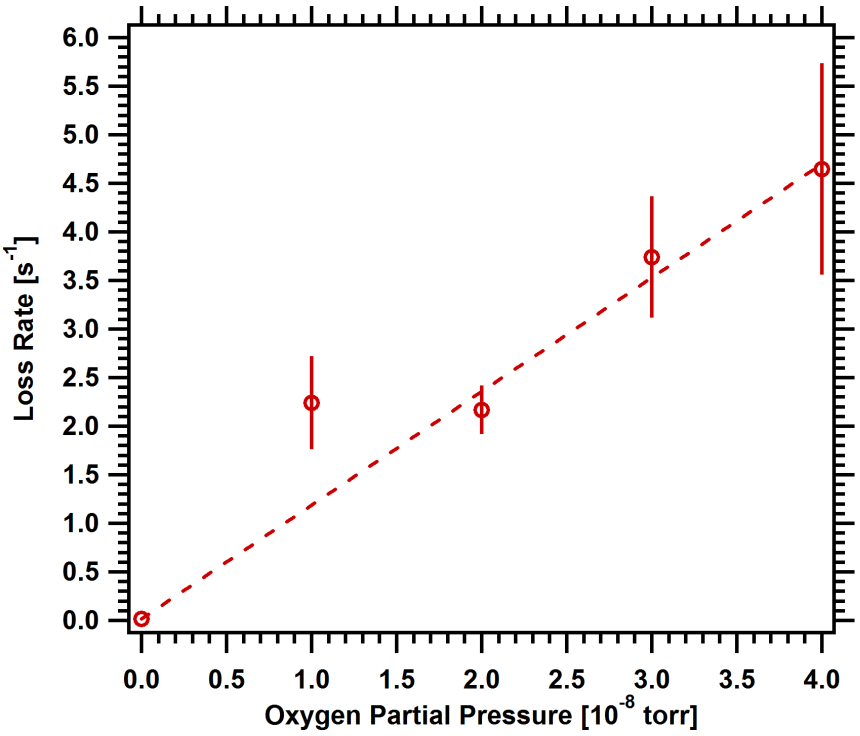

Figure 54: $^{232}Th^{3+}$ loss rate in the presence of oxygen. Measurements were made with 10^{-4} torr of helium buffer gas. The data point at zero pressure is the loss rate when only helium at 10^{-4} torr is present. The reaction rate coefficient for oxygen with Th^{3+} is $k = 3.7 \times 10^{-9}\,\mathrm{cm^3 s^{-1}}$.

an adequate SNR for measurement, 10^{-4} torr of helium was added to the system for each measurement. The loss rates measured here were in all cases significantly higher than the loss rate with only 10^{-4} torr of helium present.

The products of reaction between Th^{3+} and carbon dioxide, methane, and oxygen were identified using mass selective CEM detection. For these measurements, 2×10^{-8} torr of the test gas and 10^{-4} torr of helium buffer gas was introduced into the system. The ion trap was loaded a number of times. Each time the trap was loaded, we waited a short period (~ 1 s) for reactions to occur, performed a mass selection, and checked for the presence of ions. Since the RF power supply for our trap could not provide high enough voltage to perform rigorous mass selection on singly ionized molecules, we were only able to identify doubly ionized molecules.

When either carbon dioxide or oxygen was present, Th^{2+} and ThO^{2+} were found in the trap. Although thorium dioxide is chemically stable, no ThO_2^{2+} was detected with either gas. In their work, Johnsen et al. [127] found that oxidation of Th^+ occurs via the sequential reactions

$$Th^+ + O_2 \rightarrow ThO^+ + O \tag{51}$$

$$ThO^+ + O_2 \rightarrow ThO_2^+ + O. \tag{52}$$

They found that the first reaction proceeded quickly, with a rate coefficient of $(6 \pm 1) \times 10^{-10}\,cm^3s^{-1}$, while the rate of the second reaction was more than an order of magnitude lower, $(2 \pm 0.5) \times 10^{-11}\,cm^3s^{-1}$.

Reactions between Th^{3+} and methane led to Th^{2+} and $ThCH_2^{2+}$. Special care was taken to properly identify $ThCH_2^{2+}$. Andrews and Cho [131] were able to create $ThCH_4$ by ablating thorium in a methane environment. However, Marcalo et al. [132] found that the only reaction channel between singly-ionized thorium and methane is

$$Th^+ + CH_4 \rightarrow ThCH_2^+ + H_2. \tag{53}$$

Only 1 amu/e separates the mass-to-charge ratio of $ThCH_2^{2+}$ from $ThCH_4^{2+}$ and ThO^{2+}. By

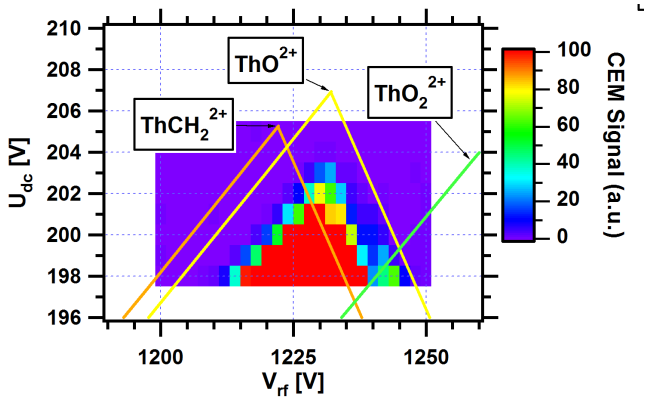

(a)

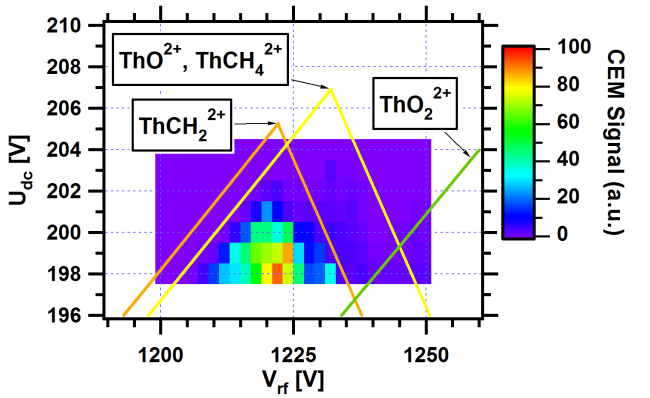

(b)

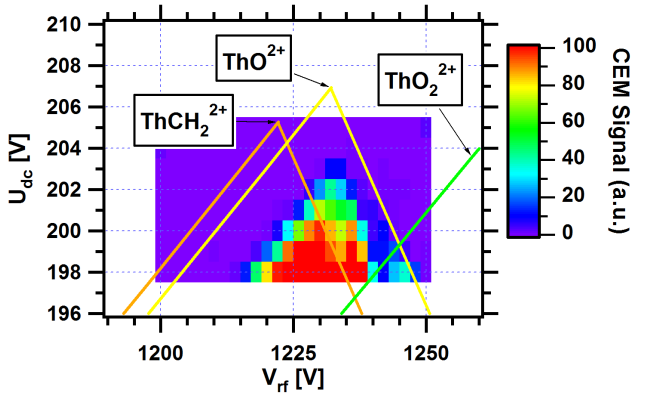

(c)

Figure 55: Doubly-ionized thorium molecules. Ions are identified by comparing the voltage space in which they are stable to the theoretical stability region. (a) The reaction between Th^{3+} and carbon dioxide produces ThO^{2+}. (b) The reaction between Th^{3+} and methane produces Th^{2+}, which in turn reacts with methane to produce $ThCH_2^{2+}$. (c) The reaction between Th^{3+} and oxygen produces Th^{2+}, which in turn reacts with oxygen to produce ThO^{2+}.

Table 7: CEM scaling factors for Th^{3+} reaction data.

Species	Carbon Dioxide	Methane	Oxygen
$\mathbf{Th^{3+}}$	9.0	4.6	3.6
$\mathbf{Th^{2+}}$	23.4	26.2	14.7
$\mathbf{ThO^{2+}}$	36.8	–	12.7
$\mathbf{ThCH_2^{2+}}$	–	53.9	–
$\mathbf{Th}X^{\mathbf{1+}}$	20.5	30.0	39.3

carefully mapping the voltage space in which ThO^{2+} and $ThCH_2^{2+}$ were stable, we were able to achieve the resolution necessary to correctly determine the product (see Figure 55).

Once the reaction products were identified, we were able to measure how Th^{3+} evolved over time in the presence of each of these gases. The results are shown in Figures 56, 57, and 58 for carbon dioxide, methane, and oxygen, respectively. Each data point in these graphs represents the average and standard deviation of six measurements. For each measurement, the trap would be loaded, and Th^{3+} would be mass selected. A fluorescence measurement would be taken immediately after the mass selection. After the specified wait time, we would mass select the ion of interest and deliver the trap contents to the CEM. The CEM signal was then normalized according to the initial fluorescence measurement. By normalizing the signal in this way, we were able to reduce the impact of loading fluctuations on the data.

As was mentioned previously, the RF power supply for our trap could not provide high enough voltage to perform rigorous mass selection on singly ionized molecules. However, by ramping the RF to its maximum voltage, we could isolate ions with mass-to-charge ratios greater than 156 amu/e. The only ions in the trap above that mass-to-charge ratio would be singly-ionized thorium molecules. These are represented as ThX^{1+} in the graphs above.

For the reasons discussed in Section 4.1.4, direct comparison of the CEM signals of the various ions is of very limited value. The ions have different charge states, masses,

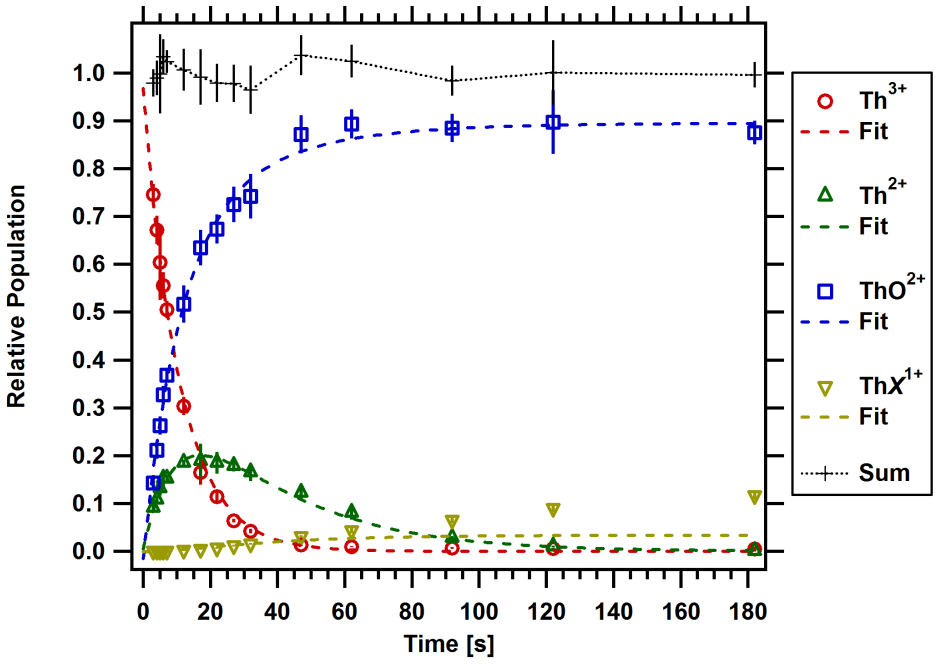

(a)

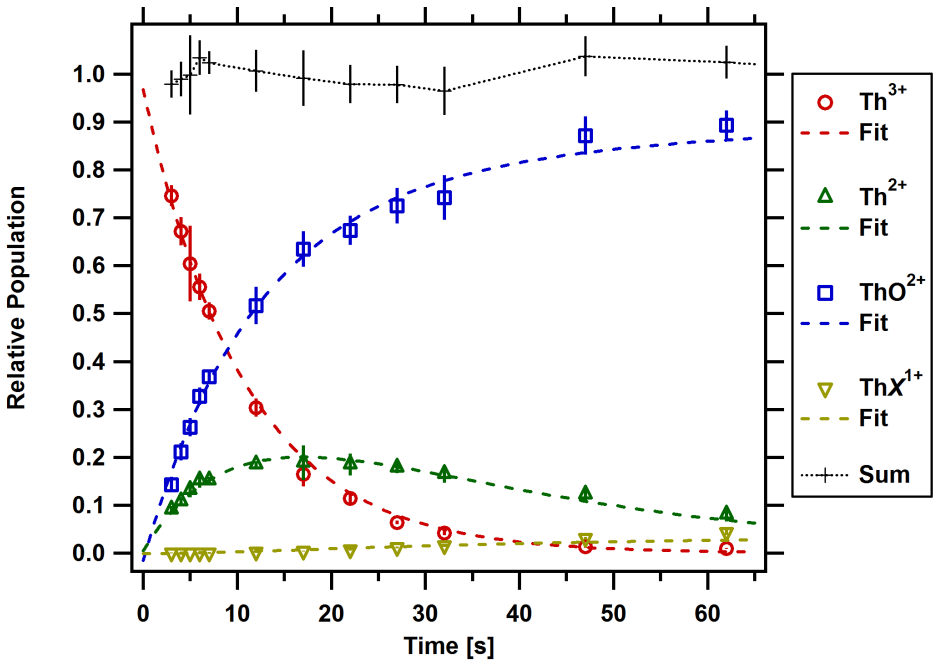

(b)

Figure 56: $^{232}Th^{3+}$ evolution in the presence of carbon dioxide. The data is scaled according to the values given in Table 7. The data sets are fit to the system of equations given in Eqs. 61 - 64. (a) Full time scale. (b) Shortened time scale.

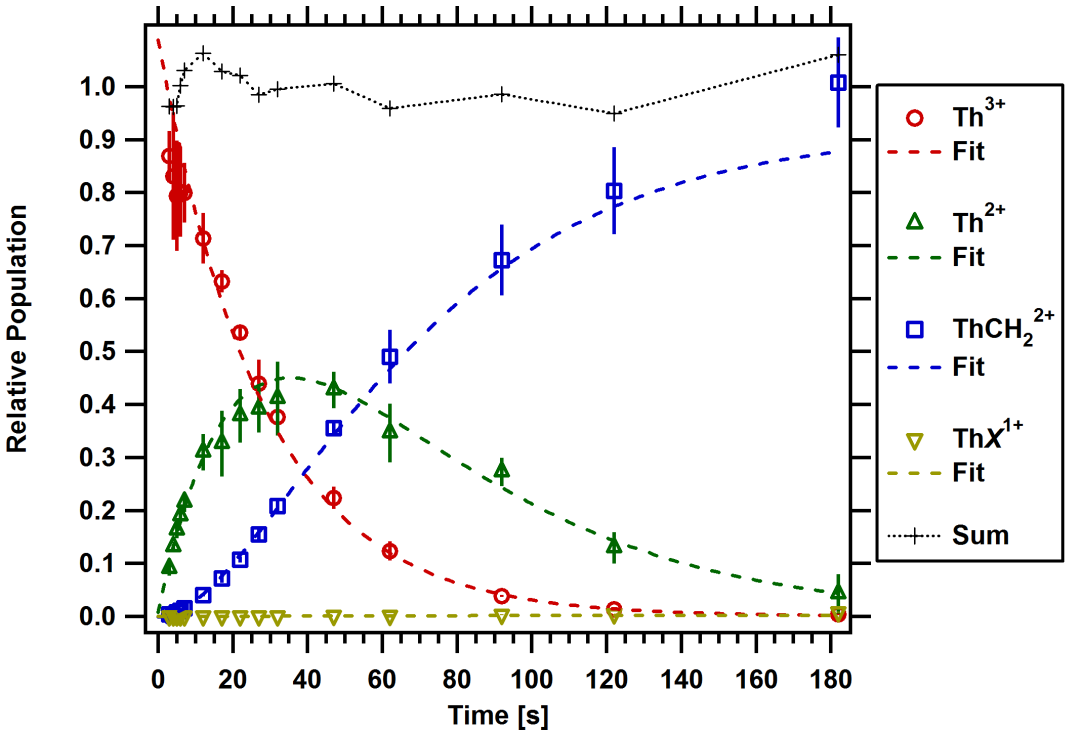

Figure 57: $^{232}Th^{3+}$ evolution in the presence of methane. The data is scaled according to the values given in Table 7. The data sets are fit to the system of equations given in Eqs. 61 - 64.

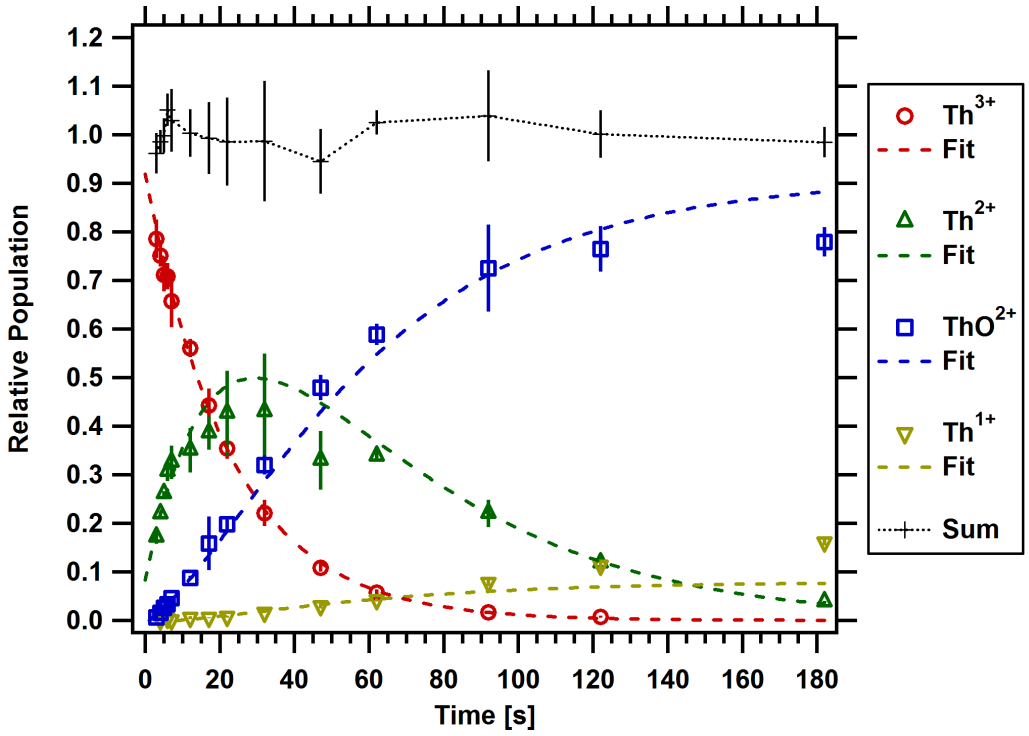

Figure 58: $^{232}Th^{3+}$ evolution in the presence of oxygen. The data is scaled according to the values given in Table 7. The data sets are fit to the system of equations given in Eqs. 61 - 64.

and chemical compositions, all of which influence the magnitude of the CEM response. In addition, mass selection in the ion trap can result in some loss of nominally stable ions. The amount of loss for a given ion at a given point in *qa*-space is not well characterized.

In order to compare the relative populations of the various ions in the trap over time, we adopted a simple method for scaling the CEM data. The method is based on two assumptions. We assume first that ions are not lost from the trap over the period of investigation. This is reasonable given the trap depth is $\sim 100\,\mathrm{eV}$ for the ions in question, while the exothermicity of the reactions is only on the order of a few eV. We further assume that the only ions present in the trap are those identified in our earlier search for the reaction products. Since our method of searching for reaction products focused only on products resulting from fast reactions, this assumption could lead to error when considering longer time scales. However, here we focus our attention on the rapid chemical kinetics that occur on short time scales.

To scale the data we consider the sum

$$N(t) = \sum_i \alpha_i n_i(t)\,, \tag{54}$$

where N is the total trap population, and n_i and α_i are the fluorescence normalized CEM signal and the CEM scaling factor for ion i, respectively. The sum is over all ion species present in the trap. The scaling factors are determined via a least-squares algorithm that attempts to make $N(t) = 1$ for all t. The data shown in Figures 56, 57, and 58 was scaled using this method. The scaling factors are given in Table 7.

Regardless of the scaling method, it is clear that the dynamics responsible for the appearance of ThO^{2+} in the presence of carbon dioxide are different from the dynamics that cause ThO^{2+} to arise in oxygen and that bring about $ThCH_2^{2+}$ in the presence of methane. Based on the identified products, the possible reactions between Th^{3+} and these gases can

be written generally as

$$\mathrm{Th}^{3+} + \mathrm{CO}_2 \quad \begin{cases} \xrightarrow{\alpha_1} & \mathrm{Th}^{2+} + \mathrm{CO}_2^+ \\ \xrightarrow{\alpha_2} & \mathrm{ThO}^{2+} + \mathrm{CO}^+ \end{cases} \tag{55}$$

$$\mathrm{Th}^{3+} + \mathrm{CH}_4 \quad \begin{cases} \xrightarrow{\beta_1} & \mathrm{Th}^{2+} + \mathrm{CH}_4^+ \\ \xrightarrow{\beta_2} & \mathrm{ThCH}_2^{2+} + \mathrm{H}_2^+ \end{cases} \tag{56}$$

$$\mathrm{Th}^{3+} + \mathrm{O}_2 \quad \begin{cases} \xrightarrow{\gamma_1} & \mathrm{Th}^{2+} + \mathrm{O}_2^+ \\ \xrightarrow{\gamma_2} & \mathrm{ThO}^{2+} + \mathrm{O}^+ \end{cases} \tag{57}$$

Here, α_i, β_i, and γ_i represent the relative probabilities of the reaction channels. The possible subsequent reactions with Th^{2+} can be summarized as

$$\mathrm{Th}^{2+} + \mathrm{CO}_2 \quad \begin{cases} \xrightarrow{\alpha_3} & \mathrm{Th}X^+ + \cdots \\ \xrightarrow{\alpha_4} & \mathrm{ThO}^{2+} + \mathrm{CO} \end{cases} \tag{58}$$

$$\mathrm{Th}^{2+} + \mathrm{CH}_4 \quad \begin{cases} \xrightarrow{\beta_3} & \mathrm{Th}X^+ + \cdots \\ \xrightarrow{\beta_4} & \mathrm{ThCH}_2^{2+} + \mathrm{H}_2 \end{cases} \tag{59}$$

$$\mathrm{Th}^{2+} + \mathrm{O}_2 \quad \begin{cases} \xrightarrow{\gamma_3} & \mathrm{Th}X^+ + \cdots \\ \xrightarrow{\gamma_4} & \mathrm{ThO}^{2+} + \mathrm{O} \end{cases} \tag{60}$$

No decay in the quantity of ThO^{2+} or ThCH_2^{2+} is seen over the time scales investigated, so these can be treated as stable final products. Thus, from the above reaction equations, we can write a system of differential equations describing the chemical kinetics in each gas. For example, in carbon dioxide,

$$\frac{d}{dt} n\left(\mathrm{Th}^{3+}\right) = -k_1 n\left(\mathrm{Th}^{3+}\right) \tag{61}$$

$$\frac{d}{dt} n\left(\mathrm{Th}^{2+}\right) = -k_2 n\left(\mathrm{Th}^{2+}\right) + \alpha_1 k_1 n\left(\mathrm{Th}^{3+}\right) \tag{62}$$

$$\frac{d}{dt} n\left(\mathrm{ThO}^{2+}\right) = \alpha_2 k_1 n\left(\mathrm{Th}^{3+}\right) + \alpha_4 k_2 n\left(\mathrm{Th}^{2+}\right) \tag{63}$$

$$\frac{d}{dt} n(\mathrm{Th}X^+) = \alpha_3 k_2 n\left(\mathrm{Th}^{2+}\right) \tag{64}$$

Similar systems of equations can be written to describe the reaction dynamics in methane and oxygen.

Table 8: Branching ratios for thorium reactions.

Branching Ratio	Carbon Dioxide	Methane	Oxygen
$[\alpha,\beta,\gamma]_1$	0.36	0.89	1.0
$[\alpha,\beta,\gamma]_2$	0.78	0.0	0.09
$[\alpha,\beta,\gamma]_3$	0.10	0.0	0.08
$[\alpha,\beta,\gamma]_4$	0.44	0.94	0.83

To estimate the relative probabilities of the various reaction channels, the data of Figures 56, 57, and 58 was numerically fit to dynamic equations of the form shown above. Fits were performed in the order of the above equations. Once a value was obtained for a fitting parameter, that value was enforced on subsequent fits. The branching ratios that were determined in this fashion are given in Table 8.

The values given in Table 8 can only be considered rough estimates of the actual branching ratios because of the uncertainties inherent in the CEM scaling procedure. They are given only to illustrate the general reaction dynamics. While reactions of Th^{3+} with methane and oxygen proceed predominantly via charge exchange, simultaneous charge exchange and chemical reaction is the dominant branch in reactions between Th^{3+} and carbon dioxide. Since methane has the highest ionization energy and lowest polarizability among hydrocarbons [133], the charge exchange reaction rates between other hydrocarbons and Th^{3+} are likely as high as those of methane.

In conclusion, we have determined the effect of various gases on the trap lifetime of Th^{3+}. Reactions involving carbon dioxide, oxygen, and methane proceed at a rate near the classical Langevin limit. Although charge exchange reactions with them are exothermic, the reaction rate coefficients for nitrogen, hydrogen, and argon are orders of magnitude less than the Langevin rate. The reaction rate coefficient between Th^{3+} and helium provides a measure of the impurities in the buffer gas. The measurement of the coefficient here provides a standard against which the vacuum and buffer gas quality of future systems can be measured. Lifetimes on the order of $5-6$ minutes were achieved in the presence of

10^{-5} torr of high purity helium buffer gas.

CHAPTER VI

CONCLUSION AND OUTLOOK

This thesis has presented progress in two experiments involving trapped ions. In the first experiment, barium ions were confined for long periods in a linear ion trap and laser cooled. The barium ions were created through electron impact and photoionization techniques. The photoionization technique relied on neutral barium spectroscopy performed in one of two high-temperature vapor cells of our design. The shortcomings in the design of the first vapor cell, notably the short vapor region and the inadequate heater, were corrected in the implementation of the second cell, which remains operable even after a year of continuous use. Though it was built for barium spectroscopy, the vapor cell can be used for spectroscopy of any alkaline-earth metal.

The last two chapters of the thesis have discussed progress toward the observation of a unique optical nuclear transition in $^{229}Th^{3+}$. Early work in this experiment was done primarily with $^{232}Th^{3+}$ that was produced via laser ablation of a metal sample. In preparation for the transition to working with the ^{229}Th isotope, a technique for creating ablation targets from small quantities of thorium nitrate was developed. The technique incorporated several precautions for the safe handling of the radioactive ^{229}Th isotope. Tests with ^{232}Th have shown that production of $^{229}Th^{3+}$ from the ablation of thorium nitrate targets is feasible.

Reaction rate coefficients between Th^{3+} and several different gases were measured. Reactions with carbon dioxide, oxygen, and methane can severely limit the trap lifetime of Th^{3+} since these gases react at a rate comparable to the classical Langevin rate. With reaction rates that are orders of magnitude lower, nitrogen, hydrogen, and argon are far less deleterious, despite the fact that charge exchange reactions between them and Th^{3+} are exothermic by several eV. The reaction rates of Th^{3+} with nitrogen and argon were found

to depend on the electronic state of the Th^{3+}. Reaction rates with helium and neon were found to correspond to reaction with impurities in the gases.

With a better understanding of the charge exchange and chemical reaction processes, additional steps can be taken to improve vacuum and buffer gas conditions. This will lead to correspondingly longer trap lifetimes for Th^{3+}. A measurement of the reaction rate coefficient between trapped Th^{3+} and the helium buffer gas provides a valuable diagnostic for determining the quality of the background vacuum in the system and the purity of the helium buffer gas. The rate coefficient for helium and the background vacuum lifetime recorded here provide a standard against which future ion trap systems can be measured.

6.1 Future Directions

The experiment involving the strong coupling of a barium ion in an optical cavity has not been actively pursued since the graduation of Adam Steele. Details on the next steps to be taken in that project are covered in his Ph.D thesis [55]. Therefore, the remarks here will be limited to the subject of the thorium ion trapping experiment.

Observation of fluorescence from trapped $^{229}Th^{3+}$ ions is the next goal in the thorium ion trapping experiment. To accomplish this goal, two challenges must be overcome. First, the frequency shift between the $^{232}Th^{3+}$ and $^{229}Th^{3+}$ isotopes must be determined. The isotope shift is due to two factors, the difference in nuclear mass, and the difference in the size of the nucleus. For atoms with heavy nuclei, like thorium, the larger contribution is from the change in the size of the nucleus. Values for the average radii of the thorium nuclei were determined by Angeli [134]. They are given in Table 9. Using these values, we have

$$\langle r^2\rangle_{232} - \langle r^2\rangle_{229} = \langle (r_{232} + r_{229})\,(r_{232} - r_{229})\rangle = (0.334 \pm 0.046)\ \text{fm}^2. \tag{65}$$

The first step in the above equation allows us to take advantage of the smaller relative uncertainty in the values of the nuclear radii to achieve a lower uncertainty in the final result.

Table 9: Nuclear radii of ^{232}Th and ^{229}Th. These values were determined by Angeli [134]. Values are given in fm.

Isotope	**r**	$(\Delta \mathbf{r})_{\mathbf{abs}}$	$(\Delta \mathbf{r})_{\mathbf{rel}}$
$^{\mathbf{229}}$**Th**	5.6807	0.0509	0.0040
$^{\mathbf{232}}$**Th**	5.7100	0.0504	

Table 10: Field shift coefficients for low-lying electronic states of Th^{3+}. Values were calculated by Berengut et al. [42]. The values are given relative to the $5F_{5/2}$ ground state.

State	**F** (GHz/fm^2)
$5F_{7/2}$	2(2)
$6D_{3/2}$	33(8)
$6D_{5/2}$	35(8)
$7S_{1/2}$	146(4)
$7P_{1/2}$	57(3)
$7P_{3/2}$	49(2)

Field shift constants for many of the low-lying electronic states were calculated by Berengut et al. [42], and they are given in Table 10. The isotope shifts of the relevant transitions can be estimated by using these values with the result of Eq. (65). The calculated shifts are given in Table 11.

The second issue that must be addressed to observe fluorescence from $^{229}Th^{3+}$ is the hyperfine structure. Consider, for example, the 1087 nm transition between the $5F_{5/2}$ ground state and the $6D_{3/2}$ state. When ^{229}Th is in its nuclear ground state, its nuclear spin is $I = 5/2$. Adding this to the total angular momentum of the ground electronic state, $j = 5/2$, results in six hyperfine levels. To observe continuous fluorescence from a $^{229}Th^{3+}$ ion, all of the hyperfine levels in the ground state must be somehow addressed.

One approach to addressing the hyperfine manifold involves putting sidebands on the optical carrier frequency of the incident laser. The hyperfine interaction causes the upper $6D_{3/2}$ state to split into four levels. By using an optical sideband to connect each of the hyperfine states in the ground state manifold to an allowed hyperfine state in the $6D_{3/2}$

Table 11: Isotope shifts for electronic transitions in Th^{3+}.

Transition	$\nu_{232} - \nu_{229}$ (GHz)
$5F_{5/2} \rightarrow 6D_{3/2}$	11(3)
$5F_{5/2} \rightarrow 6D_{5/2}$	12(3)
$5F_{7/2} \rightarrow 6D_{5/2}$	11(3)
$6D_{3/2} \rightarrow 7S_{1/2}$	38(7)
$6D_{3/2} \rightarrow 7P_{1/2}$	8(4)
$6D_{3/2} \rightarrow 7P_{3/2}$	5(4)
$6D_{5/2} \rightarrow 7P_{3/2}$	5(4)
$7S_{1/2} \rightarrow 7P_{1/2}$	−30(7)
$7S_{1/2} \rightarrow 7P_{3/2}$	−32(7)

manifold, continuous excitation can be achieved. Since the frequency shifts of the hyperfine levels are unknown, it is not possible to know at exactly what frequencies to place the optical sidebands. However, the Doppler-broadened linewidth of the transitions in a thermal cloud of Th^{3+} will be on the order of several hundred MHz. Therefore, in a thermal ion cloud, an optical sideband need only be within that range of a hyperfine transition in order to drive it. If at least one transition from each ground hyperfine state can be driven in this way, continuous excitation of the $^{229}Th^{3+}$ ions can be achieved.

Recent theoretical work [42, 135] has provided estimates of the magnetic dipole and electric quadrupole hyperfine coefficients, A and B. These estimates suggest that the hyperfine states of the $5F_{5/2}$ state can be connected to states in the $6D_{3/2}$ state with sidebands at frequencies within the range from −1 GHz to 1 GHz. Using an electro-optical modulator, a π phase shift with modulation at 200 MHz can be applied to the 1087 nm optical carrier. This will create five sidebands of comparable amplitudes spaced at 200 MHz intervals on each side of the optical carrier. This makeshift frequency comb can be scanned over the frequency space suggested by the value of the isotope shift given in Table 11. When the comb and the hyperfine transitions are sufficiently overlapped, fluorescence from a thermal cloud of $^{229}Th^{3+}$ should be observable. This will provide a reasonable first measurement of the isotope shift of the transition.

In the above, we specifically considered the $5F_{5/2} \rightarrow 6D_{3/2}$ transition, but a similar approach can be used to find the isotope shifts of the Λ-system that connects the $5F_{5/2}$, $5F_{7/2}$, and $6D_{5/2}$ states. In fact, it may be better to initially search for $^{229}Th^{3+}$ fluorescence using these transitions because optical detector efficiencies are higher at the 690 nm and 984 nm wavelengths. Alternatively, a detector sensitive at the 1087 nm wavelength, such as a member of the ID400 series from ID Quantique, could be purchased.

After fluorescence of the $^{229}Th^{3+}$ ions is initially found, an iterative approach to improving the placement of the optical sidebands can be attempted. By using multiple frequency generators to produce the optical sidebands, the sidebands can be individually tuned to maximize the fluorescence of the $^{229}Th^{3+}$ ion cloud. This approach may allow the hyperfine shifts to be determined to a precision sufficient to implement laser cooling of the $^{229}Th^{3+}$.

Alternatively, if the hyperfine shifts must be measured to higher precision, a microwave-optical double resonance technique could be used. This technique has been used, for example, to measure the complex hyperfine manifolds of several singly-ionized europium isotopes [136, 137]. The technique works as follows. A single optical transition is driven between hyperfine levels of the ground and excited states. The population of the ground hyperfine state addressed by the laser is depleted as ions are optically pumped into adjacent hyperfine states. A microwave field is applied to the trapped ions using a resonator or an antenna, and its frequency is scanned. When the microwaves drive ions from the adjacent hyperfine levels back into the pumped hyperfine state, photons from the optically excited ions can be detected. If these photons are detected with a time-resolved photon counter synchronized to the scanning microwave field, the splitting between the hyperfine states can be measured. The resonances detected in this way are essentially free of Doppler-broadening because of the long wavelength of the microwaves. Thus, a very precise measurement is obtained without laser cooling the ions.

Even with a thorough knowledge of the hyperfine structure, laser cooling $^{229}Th^{3+}$ will

not be trivial. Each hyperfine state in the lower electronic levels of the optical transitions will still have to be addressed either with an optical sideband or a microwave field. To this author's knowledge, no ion or atom with such a large number of hyperfine levels in the electronic states of its main optical transitions has ever been laser cooled. However, the ability to directly laser cool the ion may not be strictly necessary. Sympathetic cooling with $^{232}Th^{3+}$ or another ion could be employed.

Once a single $^{229}Th^{3+}$ can be cooled and localized in the ion trap, the search for the isomer transition can begin. The search is complicated by the large uncertainty in the energy of the transition. The range of wavelengths corresponding to the latest measurement of the isomer energy is in the deep UV. Light at these wavelengths is difficult to generate, and once generated, it is strongly attenuated in air. By initially searching for the isomer via an electron bridge transition, the search range can be shifted to the near UV and visible spectrum. Furthermore, by searching with a frequency comb, the search range can be covered much more rapidly.

Increasing the trap lifetime of Th^{3+} would benefit both the search for the hyperfine structure and the search for the isomer transition. The measurements of Chapter 5 have shown some of the gases that must be specifically targeted for removal from the vacuum system and buffer gas to reduce the rate of Th^{3+} reactions. If the sum of the partial pressures of all fast reacting gases was brought below 10^{-12} torr, a Th^{3+} trap lifetime of over an hour could be obtained.

APPENDIX A

ADDITIONAL TABLES

Table 12: Ionization energies of thorium. The values are taken from the CRC Handbook of Chemistry and Physics [133]. Ionization energies are given in eV.

Atom/Ion	**Ionization Energy**
Th	6.3067
Th^{1+}	11.9
Th^{2+}	20.0
Th^{3+}	28.8

Table 13: Ionization energies and polarizabilities of relevant atoms and molecules. The values are taken from the CRC Handbook of Chemistry and Physics [133]. Ionization energies are given in eV. Polarizabilities are given in $Å^3$.

Atom/Molecule	**Ionization Energy**	**Polarizability**
Ar	15.759	1.664
CH_4	12.610	2.448
CO_2	13.777	2.507
H_2	15.426	0.787
He	24.587	0.208
N_2	15.581	1.710
Ne	21.565	0.381
O_2	12.070	1.581

Table 14: Purity specifications of gases used in reaction experiments. Specifications are taken from the Airgas 2009 Product Catalog [138]. Values are given in ppm unless otherwise stated. (∗) CO + CO_2 < 1 ppm. (∗∗) < 20 ppm ethane, < 15 ppm other hydrocarbons.

Gas	Symbol	Minimum Purity	Ar	CO	CO_2	He	H_2O	N_2	O_2	THC
Research Grade Argon	**Ar**	99.9997%		< 0.5	< 0.5		< 0.5	< 3	< 0.2	< 0.2
Pure Clean Carbon Dioxide	**CO_2**	99.995%					< 5			< 5
BIP Helium	**He**	99.9999%					< 20 ppb	< 3	< 10 ppb	< 100 ppb
UHP Hydrogen	**H_2**	99.999%		< 0.5*	< 0.5*		< 2	< 5	< 1	< 0.5
UHP Methane	**CH_4**	99.99%					< 5	< 70	< 5	< 35**
Research Grade Neon	**Ne**	99.999%	< 1	< 0.5	< 0.5	< 8	< 1	< 2	< 0.5	< 0.5
Prepurified Nitrogen	**N_2**	99.998%					< 5		< 5	
UHP Oxygen	**O_2**	99.994%	< 35	< 1	< 1	< 2	< 15		< 0.5	

APPENDIX B

PROGRAM LISTINGS

This appendix includes programs used to create stability diagrams.

B.1 Stability Base Package

In Listing B.1 is the header file for the stability base package.

```
#ifndef _STABILITYBASE_H
#define _STABILITYBASE_H

#include <maplec.h>
#include <math.h>
#include <stdio.h>

#ifndef PI
#define PI 3.141592653589793
#endif

int————→startMaple();
int ZI_Xcurve(int, double, char*, double*, double*);
int————→ZI_Ycurve(int, double, char*, double, double);
int mapBeta(int, int, double, double, int, double, ↓
→    double, char*);

double getMatrixTrace(int, double, double);
double getBeta(int, double, double);
double findQCrossing(int, double, double, double, double↓
→    , double*);
double findACrossing(int, double, double, double, double↓
→    , double*);

static void M_DECL textCallBack(void*, int, char*);

#endif
```

Listing B.1: (StabilityBase.h)The header file for the stability base package.

In Listing B.2 is the definitions file for the stability base package

```
#include "stdafx.h"

static MKernelVector kv = NULL;    /* Maple kernel handle */
static char err[2048];    /* command input and error string buffers */
static MCallBackVectorDesc cb = {
   textCallBack,
   0,    /* errorCallBack not used */
   0,    /* statusCallBack not used */
   0,    /* readLineCallBack not used */
   0,    /* redirectCallBack not used */
   0,    /* streamCallBack not used */
   0,    /* queryInterrupt not used */
   0     /* callBackCallBack not used */
};

int startMaple() {
   if ( (kv = StartMaple(0,NULL,&cb,NULL,NULL,err)) == ↓
→        NULL)
      return (-1);
   else
      return (0);
}

int ZI_Xcurve(int dprec, double tval, char *fname, ↓
→     double *qend, double *aend) {
   int slp, apx;
   double q, ql, qh, a, al, ah, prec, pprec, hprec, tres↓
→       ;
   FILE *fp;

   if (fname == NULL)
      fp = stdout;
   else if ( (fp = fopen(fname,"w")) == NULL)
      return (-1);

   prec = pow(0.1,dprec);
   pprec = prec*10;
   hprec = 0.5*prec;

   apx = 0;
   slp = 0;
   ql = 0;
```

```
      qh = 0.1;
41    a = 0;

      while (!apx) {
         if (!slp)
            q = findQCrossing(dprec,tval,-1*a,ql,qh,&tres);
46       else
            a = abs(findACrossing(dprec,tval,q,-1*al,-1*ah↓
→              ,&tres));

         if (abs(getMatrixTrace(dprec,q,a)) > tres)
            apx = 1;
51
         if (!slp) {
            if ((q < (ql+hprec)) && (q > 0)) {
               slp = 1;
               al = a;
56             ah = al + pprec;
               q += prec;
               continue;
            }
            else if (q > (qh-hprec)) {
61             qh += pprec;
               continue;
            }
         }
         else {
66          if (a < (al+hprec)) {
               slp = 0;
               ql = q;
               qh = ql + pprec;
               a += prec;
71             continue;
            }
            else if (a > (ah-hprec)) {
               ah += pprec;
               continue;
76          }
         }

         fprintf(fp, "%0.*f,␣%0.*f\n", dprec, q, dprec, a);

81       if (!slp) {
            qh = q + q - ql + prec;
            ql = q;
```

```
            a += prec;
         }
86       else {
            ah = a + a - al + prec;
            al = a;
            q += prec;
         }
91    }

      if (fname != NULL)
         fclose(fp);

96    *qend = q;
      *aend = a;

      return (0);
   }
101
   int ZI_Ycurve(int dprec, double tval, char *fname, ↓
→     double qx, double ax) {
      int slp;
      double q, ql, qh, a, al, ah, prec, pprec, hprec, tres↓
→        ;
      FILE *fp;
106
      if (fname == NULL)
         fp = stdout;
      else if ( (fp = fopen(fname,"w")) == NULL)
         return (-1);
111
      prec = pow(0.1,dprec);
      pprec = prec*10;
      hprec = 0.5*prec;

116   ql = 0;
      qh = 0;

      slp = 1;
      al = ax;
121   ah = al - 0.1;
      q  = qx;

      while (al > 0) {
         if (!slp){
126         q = findQCrossing(dprec,tval,a,ql,qh,&tres);
```

```
            fprintf(fp, "find␣Q:\tq␣=␣%f,␣ql␣=␣%f,␣qh␣=␣%f\↓
→               n\ta␣=␣%f,␣al␣=␣%f,␣ah␣=␣%f\n\ttr␣=␣%f\n",
                q, ql, qh, a, al, ah,tres);

            if ((q < (ql+hprec)) && (q > 0)) {
131             slp = 1;
                al = a;
                ah = al - pprec;
                q += prec;
————————→————————→————————→continue;
136         }
            else if (q > (qh-hprec)) {
                qh += pprec;
                continue;
            }
141     }
        else {
            a = findACrossing(dprec,tval,q,al,ah,&tres);

            if (a > (al-hprec)) {
146             slp = 0;
                ql = q;
                qh = ql + pprec;
                a -= prec;
                continue;
151         }
            else if (a < (ah+hprec)) {
                ah -= pprec;
                continue;
            }
156     }

        fprintf(fp, "%0.*f,␣%0.*f\n", dprec, q, dprec, a);

        if (!slp) {
161         qh = q + q - ql + prec;
            ql = q;
            a -= prec;
        }
        else {
166         ah = a + a - al - prec;
            al = a;
            q += prec;
        }
    }
```

```
171
      if (fname != NULL)
         fclose(fp);

      return (0);
176 }

   int mapBeta(int dprec, int qstep, double qlow, double ↓
→     qhigh, int astep, double alow, double ahigh, char *↓
→     fname) {
      double q, a, dq, da;
      FILE *fp;
181
      dq = (qhigh - qlow)/(qstep - 1);
      da = (ahigh - alow)/(astep - 1);

      if ( (fp = fopen(fname,"w")) == NULL)
186      return (-1);

      fprintf(fp,"qlow␣=␣%f,␣qhigh␣=␣%f,␣dq␣=␣%f,␣steps␣=␣%↓
→        d\n", qlow, qhigh, dq, qstep);
      fprintf(fp,"alow␣=␣%f,␣ahigh␣=␣%f,␣da␣=␣%f,␣steps␣=␣%↓
→        d\n", alow, ahigh, da, astep);
      fprintf(fp,"----------------------------------------\↓
→        n");
191
      for (q = qlow; q <= qhigh; q += dq) {
         for (a = alow; a < ahigh; a += da)
            fprintf(fp,"%0.*f,␣", dprec, getBeta(dprec,q,a)↓
→              );

196      fprintf(fp,"%0.*f\n", dprec, getBeta(dprec,q,a));
      }

      fclose(fp);

201   return (0);
   }

   double getMatrixTrace(int dprec, double q, double a) {
      char expr[256];
206
      sprintf(expr, "MathieuC(%0.*f,%0.*f,Pi)+MathieuSPrime↓
→        (%0.*f,%0.*f,Pi);",
         dprec, a, dprec, q, dprec, a, dprec, q);
```

```
   return (MapleToFloat64(kv,EvalMapleStatement(kv,expr)↓
→     ));
}

double getBeta(int dprec, double q, double a) {
   char expr[256];

   sprintf(expr, "evalf(Re(arccos(0.5*(MathieuC(%0.*f↓
→     ,%0.*f,Pi)+MathieuSPrime(%0.*f,%0.*f,Pi))))/Pi);",
      dprec, a, dprec, q, dprec, a, dprec, q);

   return (MapleToFloat64(kv,EvalMapleStatement(kv,expr)↓
→     ));
}

double findQCrossing(int dprec, double tval, double aset↓
→   , double qlow, double qhigh, double *tres) {
   double q, ql, qh, t, tl, th, prec;

   ql = qlow;
   qh = qhigh;
   th = -1;
   tl = abs(getMatrixTrace(dprec, ql, aset));

   prec = pow(0.1,dprec);

   while (abs(qh-ql) > prec) {
      q = (ql+qh)/2;
      t = abs(getMatrixTrace(dprec, q, aset));

      if (t == tval)
         { ql = q; qh = q; tl = t; th = t; }
      else if (tl == tval)
         { qh = ql; th = tl; }
      else if ((tval - tl)*(tval - t) < 0)
         { qh = q; th = t; }
      else
         { ql = q; tl = t; }
   }

   if (th < 0)
      th = abs(getMatrixTrace(dprec, qh, aset));

   if (abs(tval - th) < abs(tval - tl)) {
```

```
      q = qh;
      *tres = th;
   }
   else {
      q = ql;
      *tres = tl;
   }

   return (q);
}

double findACrossing(int dprec, double tval, double qset↓
   , double alow, double ahigh, double *tres) {
   double a, al, ah, t, tl, th, prec;

   al = alow;
   ah = ahigh;
   th = -1;
   tl = abs(getMatrixTrace(dprec, qset, al));

   prec = pow(0.1,dprec);

   while (abs(ah-al) > prec) {
      a = (al+ah)/2;
      t = abs(getMatrixTrace(dprec, qset, a));

      if (t == tval)
         { al = a; ah = a; tl = t; th = t; }
      else if (tl == tval)
         { ah = al; th = tl; }
      else if ((tval - tl)*(tval - t) < 0)
         { ah = a; th = t; }
      else
         { al = a; tl = t; }
   }

   if (th < 0)
      th = abs(getMatrixTrace(dprec, qset, ah));

   if (abs(tval - th) < abs(tval - tl)) {
      a = ah;
      *tres = th;
   }
   else {
      a = al;
```

```
        *tres = tl;
    }

    return (a);
}

static void M_DECL textCallBack(void *data, int tag, ↓
→   char *output)
{
    // printf("%s\n",output);
}
```

Listing B.2: (StabilityBase.c) The definitions file for the stability base package.

B.2 Stability Diagrams

In Listing B.3 is a program that utilizes functions in the stability base package to produce diagrams of the first stability region of the Mathieu equation.

```
#include "stdafx.h"

int init_trace(int, char**, double*);

int main(int argc, char **argv)
{
    int dprec;
    double qx, ax, tr;

    if ( (dprec = init_trace(argc, argv, &tr)) < 0)
        return (-1);

    if (startMaple() < 0) {
        printf("ERROR:␣unable␣to␣start␣Open␣Maple\n");
        return (-1);
    }

    if (ZI_Xcurve(dprec, tr, argv[3], &qx, &ax) < 0) {
        printf("ERORR:␣unable␣to␣write␣stability␣curve\n")↓
→           ;
        return (-1);
    }
```

```
22
      if (ZI_Ycurve(dprec, tr, argv[4], qx, ax) < 0) {
         printf("ERROR\n");
         return (-1);
      }
27
      return (0);
   }

   int init_trace(int argc, char **argv, double *trace) {
32    int dprec;
      char usage[256];

      sprintf(usage, "USAGE:␣%s␣[digits_of_precision]␣[↓
→        trace_value]␣[file_1]␣[file_2]", argv[0]);

37    if (argc != 5) {
         printf ("ERROR:␣incorrect␣number␣of␣arguments\n%s\↓
→           n", usage);
         return (-1);
      }

42    if (sscanf(argv[1], "%d", &dprec) != 1) {
         printf("ERROR:␣[digits_of_precision]␣must␣be␣an␣↓
→           integer\n%s\n", usage);
         return (-1);
      }

47    if (dprec < 3) {
         printf("ERROR:␣[digits_of_precision]␣must␣be␣↓
→           greater␣than␣or␣equal␣to␣three\n%s\n", usage);
         return (-1);
      }

52    if (sscanf(argv[2], "%lf", trace) != 1) {
         printf("ERROR:␣[trace_value]␣must␣be␣a␣floating␣↓
→           point␣number\n%s\n", usage);
         return (-1);
      }

57    if ((*trace < 0) || (*trace > 2)) {
         printf("ERROR:␣[trace_value]␣must␣not␣be␣less␣than↓
→           ␣zero␣or␣greater␣than␣two\n%s\n", usage);
         return (-1);
      }
```

```
62     return (dprec);
   }
```

Listing B.3: (Stability.c) The main program file for producing stability diagrams.

B.3 Beta Contour Maps

In Listing B.4 is a program that utilizes functions in the stability base package to produce a contour map of the beta parameter.

```
 1  #include "StabilityBase.h"
 2
    int init_beta(int, char **, int*, double*, double*, int↓
→      *, double*, double*);

    int main(int argc, char **argv)
    {
 7     int dprec, qstep, astep;
       double qlow, qhigh, alow, ahigh;

       if ( (dprec = init_beta(argc, argv, &qstep, &qlow, &↓
→         qhigh, &astep, &alow, &ahigh)) < 0)
          return (-1);
12
       if (startMaple() < 0) {
          printf("ERROR:␣unable␣to␣start␣Open␣Maple\n");
          return (-1);
       }
17
       if (mapBeta(dprec, qstep, qlow, qhigh, astep, alow, ↓
→         ahigh, argv[8]) < 0) {
          printf("ERROR:␣unable␣to␣open␣file␣%s\n", argv[8])↓
→            ;
          return (-1);
       }
22
       return 0;
    }
```

```
int init_beta(int argc, char **argv, int *qstep, double ↓
→    *qlow, double *qhigh, int *astep, double *alow, ↓
→    double *ahigh) {
    int dprec;
    char usage[256];

    sprintf(usage, "USAGE: %s [digits_of_precision] [↓
→       q_steps] [q_low] [q_high] [a_steps] [a_low] [↓
→       a_high] [file]", argv[0]);

    if (argc != 9) {
       printf("ERROR: incorrect number of arguments\n%s\n↓
→          ", usage);
       return (-1);
    }

    if (sscanf(argv[1], "%d", &dprec) != 1) {
       printf("ERROR: [digits_of_precision] must be an ↓
→          integer\n%s\n", usage);
       return (-1);
    }

    if (dprec < 3) {
       printf("ERROR: [digits_of_precision] must be ↓
→          greater than or equal to three\n%s\n", usage);
       return (-1);
    }

    if (sscanf(argv[2], "%d", qstep) != 1) {
       printf("ERROR: [q_steps] must be an integer\n%s\n"↓
→          , usage);
       return (-1);
    }

    if (*qstep < 2) {
       printf("ERROR: [q_steps] must be greater than or ↓
→          equal to two\n%s\n", usage);
       return (-1);
    }

    if (sscanf(argv[3], "%lf", qlow) != 1) {
       printf("ERROR: [q_low] must be a floating point ↓
→          number\n%s\n", usage);
       return (-1);
    }
```

```
62      if (sscanf(argv[4], "%lf", qhigh) != 1) {
           printf("ERROR:␣[q_high]␣must␣be␣a␣floating␣point␣↓
→             number\n%s\n", usage);
           return (-1);
        }

67      if (*qhigh <= *qlow) {
           printf("ERROR:␣[q_high]␣must␣be␣greater␣than␣[↓
→             q_low]\n%s\n", usage);
           return (-1);
        }

72      if (sscanf(argv[5], "%d", astep) != 1) {
           printf("ERROR:␣[a_steps]␣must␣be␣an␣integer\n%s\n"↓
→             , usage);
           return (-1);
        }

77      if (*astep < 2) {
           printf("ERROR:␣[a_steps]␣must␣be␣greater␣than␣or␣↓
→             equal␣to␣two\n%s\n", usage);
           return (-1);
        }

82      if (sscanf(argv[6], "%lf", alow) != 1) {
           printf("ERROR:␣[a_low]␣must␣be␣a␣floating␣point␣↓
→             number\n%s\n", usage);
           return (-1);
        }

87      if (sscanf(argv[7], "%lf", ahigh) != 1) {
           printf("ERROR:␣[a_high]␣must␣be␣a␣floating␣point␣↓
→             number\n%s\n", usage);
           return (-1);
        }

92      if (*ahigh <= *alow) {
           printf("ERROR:␣[a_high]␣must␣be␣greater␣than␣[↓
→             a_low]\n%s\n", usage);
           return (-1);
        }

97      return (dprec);
     }
```

Listing B.4: (Beta.c) The main program file for producing contour plots of the beta parameter.

REFERENCES

[1] D. Wineland and H. Dehmelt, "Proposed 1014 Delta Upsilon Less Than Upsilon Laser Fluorescence Spectroscopy on T1+ Mono-Ion Oscillator Iii," *Bulletin of the American Physical Society* **20**, 637 (1975).

[2] T. W. Hansch and A. L. Schawlow, "Cooling of Gases by Laser Radiation," *Optics Communications* **13**, 68 (1975).

[3] M. H. Anderson, J. R. Ensher, M. R. Matthews, C. E. Wieman, and E. A. Cornell, "Observation of Bose-Einstein Condensation in a Dilute Atomic Vapor," *Science* **269**, 198 (1995).

[4] K. B. Davis, M. O. Mewes, M. R. Andrews, N. J. Vandruten, D. S. Durfee, D. M. Kurn, and W. Ketterle, "Bose-Einstein Condensation in a Gas of Sodium Atoms," *Physical Review Letters* **75**, 3969 (1995).

[5] J. Benhelm, G. Kirchmair, C. F. Roos, and R. Blatt, "Towards fault-tolerant quantum computing with trapped ions," *Nature Physics* **4**, 463 (2008).

[6] T. Monz, K. Kim, W. Hansel, M. Riebe, A. S. Villar, P. Schindler, M. Chwalla, M. Hennrich, and R. Blatt, "Realization of the Quantum Toffoli Gate with Trapped Ions," *Physical Review Letters* **102**, (2009).

[7] D. Hanneke, J. P. Home, J. D. Jost, J. M. Amini, D. Leibfried, and D. J. Wineland, "Realization of a programmable two-qubit quantum processor," *Nature Physics* **6**, 13 (2010).

[8] M. D. Barrett, J. Chiaverini, T. Schaetz, J. Britton, W. M. Itano, J. D. Jost, E. Knill, C. Langer, D. Leibfried, R. Ozeri, and D. J. Wineland, "Deterministic quantum teleportation of atomic qubits," *Nature* **429**, 737 (2004).

[9] M. Riebe, H. Haffner, C. F. Roos, W. Hansel, J. Benhelm, G. P. T. Lancaster, T. W. Korber, C. Becher, F. Schmidt-Kaler, D. F. V. James, and R. Blatt, "Deterministic quantum teleportation with atoms," *Nature* **429**, 734 (2004).

[10] R. Zhao, Y. O. Dudin, S. D. Jenkins, C. J. Campbell, D. N. Matsukevich, T. A. B. Kennedy, and A. Kuzmich, "Long-lived quantum memory," *Nature Physics* **5**, 100 (2009).

[11] P. Clade, E. de Mirandes, M. Cadoret, S. Guellati-Khelifa, C. Schwob, F. Nez, L. Julien, and F. Biraben, "Determination of the fine structure constant based on Bloch oscillations of ultracold atoms in a vertical optical lattice," *Physical Review Letters* **96**, (2006).

[12] V. Gerginov, K. Calkins, C. E. Tanner, J. J. McFerran, S. Diddams, A. Bartels, and L. Hollberg, "Optical frequency measurements of 6s S-2(1/2)-6p P-2(1/2) (D-1) transitions in Cs-133 and their impact on the fine-structure constant," *Physical Review A* **73**, (2006).

[13] A. K. Tuchman and M. A. Kasevich, "Phase-Slip Interferometry for Precision Force Measurements," *Physical Review Letters* **103**, (2009).

[14] N. National Space-Based Positioning and T. C. Office, "Global Positioning System: Serving the World," 2010.

[15] M. A. Lombardi, T. P. Heavner, and S. R. Jefferts, "NIST Primary Frequency Standards and the Realization of the SI Second," *NCSL International Measure* **2**, 74 (2007).

[16] L. Essen and J. V. L. Parry, "Caesium Resonator," *Nature* **176**, 281 (1955).

[17] N. F. Ramsey, "The Method of Successive Oscillatory Fields," *Physics Today* **33**, 25 (1980).

[18] J. H. Shirley, W. D. Lee, and R. E. Drullinger, "Accuracy evaluation of the primary frequency standard NIST-7," *Metrologia* **38**, 427 (2001).

[19] A. D. Ludlow, T. Zelevinsky, G. K. Campbell, S. Blatt, M. M. Boyd, M. H. G. de Miranda, M. J. Martin, J. W. Thomsen, S. M. Foreman, J. Ye, T. M. Fortier, J. E. Stalnaker, S. A. Diddams, Y. Le Coq, Z. W. Barber, N. Poli, N. D. Lemke, K. M. Beck, and C. W. Oates, "Sr lattice clock at 1 x 10(-16) fractional uncertainty by remote optical evaluation with a Ca clock," *Science* **319**, 1805 (2008).

[20] C. W. Hoyt, Z. W. Barber, C. W. Oates, T. M. Fortier, S. A. Diddams, and L. Hollberg, "Observation and absolute frequency measurements of the S-1(0)-P-3(0) optical clock transition in neutral ytterbium," *Physical Review Letters* **95**, (2005).

[21] T. Rosenband, D. B. Hume, P. O. Schmidt, C. W. Chou, A. Brusch, L. Lorini, W. H. Oskay, R. E. Drullinger, T. M. Fortier, J. E. Stalnaker, S. A. Diddams, W. C. Swann, N. R. Newbury, W. M. Itano, D. J. Wineland, and J. C. Bergquist, "Frequency ratio of Al+ and Hg+ single-ion optical clocks; Metrology at the 17th decimal place," *Science* **319**, 1808 (2008).

[22] J. I. Cirac, P. Zoller, H. J. Kimble, and H. Mabuchi, "Quantum state transfer and entanglement distribution among distant nodes in a quantum network," *Physical Review Letters* **78**, 3221 (1997).

[23] A. V. Steele, L. R. Churchill, P. F. Griffin, and M. S. Chapman, "Photoionization and photoelectric loading of barium ion traps," *Physical Review A* **75**, (2007).

[24] E. Peik and C. Tamm, "Nuclear laser spectroscopy of the 3.5eV transition in Th-229," *Europhysics Letters* **61**, 181 (2003).

[25] V. V. Flambaum, "Enhanced effect of temporal variation of the fine structure constant and the strong interaction in Th-229," *Physical Review Letters* **97**, (2006).

[26] A. C. Hayes and J. L. Friar, "Sensitivity of nuclear transition frequencies to temporal variation of the fine structure constant or the strong interaction," *Physics Letters B* **650**, 229 (2007).

[27] X. T. He and Z. Z. Ren, "Enhanced sensitivity to variation of fundamental constants in the transitions of Th-229 and Bk-249," *Journal of Physics G-Nuclear and Particle Physics* **34**, 1611 (2007).

[28] X. T. He and Z. Z. Ren, "Temporal variation of the fine structure constant and the strong interaction parameter in the Th-229 transition," *Nuclear Physics A* **806**, 117 (2008).

[29] L. A. Kroger and C. W. Reich, "Features of Low-Energy Level Scheme of Th-229 as Observed in Alpha-Decay of U-233," *Nuclear Physics A* **259**, 29 (1976).

[30] C. W. Reich and R. G. Helmer, "Energy Separation of the Doublet of Intrinsic States at the Ground-State of Th-229," *Physical Review Letters* **64**, 271 (1990).

[31] D. G. Burke, P. E. Garrett, T. Qu, and R. A. Naumann, "Additional Evidence for the Proposed Excited-State at Less-Than-or-Equal to 5 Ev in Th-229," *Physical Review C* **42**, R499 (1990).

[32] R. G. Helmer and C. W. Reich, "An Excited-State of Th-229 at 3.5 Ev," *Physical Review C* **49**, 1845 (1994).

[33] B. R. Beck, J. A. Becker, P. Beiersdorfer, G. V. Brown, K. J. Moody, J. B. Wilhelmy, F. S. Porter, C. A. Kilbourne, and R. L. Kelley, "Energy splitting of the ground-state doublet in the nucleus Th-229," *Physical Review Letters* **98**, (2007).

[34] D. G. Burke, P. E. Garrett, T. Qu, and R. A. Naumann, "Nuclear structure of Th-229,Th-231 studied with the Th-230,Th-232(d, t) reactions," *Nuclear Physics A* **809**, 129 (2008).

[35] C. J. Campbell, A. V. Steele, L. R. Churchill, M. V. DePalatis, D. E. Naylor, D. N. Matsukevich, A. Kuzmich, and M. S. Chapman, "Multiply Charged Thorium Crystals for Nuclear Laser Spectroscopy," *Physical Review Letters* **102**, (2009).

[36] P. F. A. Klinkenberg, "Spectral Structure of Trebly Ionized Thorium, Th-Iv," *Physica B & C* **151**, 552 (1988).

[37] P. Kalman and T. Bukki, "Deexcitation of Th-229(m): Direct gamma decay and electronic-bridge process," *Physical Review C* **6302**, (2001).

[38] E. V. Tkalya, "Properties of the optical transition in the Th-229 nucleus," *Physics-Uspekhi* **46**, 315 (2003).

[39] S. G. Porsev and V. V. Flambaum, "Effect of atomic electrons on the 7.6-eV nuclear transition in Th-229(3+)," *Physical Review A* **81**, (2010).

[40] Gerstenk.S, P. Luc, J. Verges, Englekem.Dw, J. E. Gindler, and F. S. Tomkins, "Hyperfine-Structure, Magnetic and Quadrupole-Moments of Thorium 229 Isotope," *Journal De Physique* **35**, 483 (1974).

[41] A. M. Dykhne and E. V. Tkalya, "Matrix element of the anomalously low-energy (3.5 +/- 0.5eV) transition in Th-229 and the isomer lifetime," *Jetp Letters* **67**, 251 (1998).

[42] J. C. Berengut, V. A. Dzuba, V. V. Flambaum, and S. G. Porsev, "Proposed Experimental Method to Determine alpha Sensitivity of Splitting between Ground and 7.6 eV Isomeric States in Th-229," *Physical Review Letters* **102**, (2009).

[43] B. H. Bransden and C. J. Joachain, *Physics of atoms and molecules*, 2nd ed. (Prentice Hall, Harlow, England ; New York, 2003).

[44] J. D. Prestage, G. J. Dick, and L. Maleki, "New Ion Trap for Frequency Standard Applications," *Journal of Applied Physics* **66**, 1013 (1989).

[45] W. Paul and H. Steinwedel, "*Ein Neues Massenspektrometer Ohne Magnetfeld," *Zeitschrift Fur Naturforschung Section a-a Journal of Physical Sciences* **8**, 448 (1953).

[46] J. D. Prestage, R. L. Tjoelker, R. T. Wang, G. J. Dick, and L. Maleki, "Hg+ Trapped Ion Standard with the Superconducting Cavity Maser Oscillator," *Ieee Transactions on Instrumentation and Measurement* **42**, 200 (1993).

[47] D. J. Griffiths, *Introduction to electrodynamics*, 3rd ed. (Prentice Hall, Upper Saddle River, N.J., 1999).

[48] P. K. Ghosh, *Ion traps*The International series of monographs on physics (Clarendon Press ; Oxford University Press, Oxford New York, 1995).

[49] N. V. Konenkov, M. Sudakov, and D. J. Douglas, "Matrix methods for the calculation of stability diagrams in quadrupole mass spectrometry," *Journal of the American Society for Mass Spectrometry* **13**, 597 (2002).

[50] L. A. Pipes, "Matrix Solution of Equations of the Mathieu-Hill Type," *Journal of Applied Physics* **24**, 902 (1953).

[51] F. G. Major and H. G. Dehmelt, "Exchange-Collision Technique for Rf Spectroscopy of Stored Ions," *Physical Review* **170**, 91 (1968).

[52] Maplesoft, "Maple 11.0," 2007.

[53] T. Baba and I. Waki, "Laser-cooled fluorescence mass spectrometry using laser-cooled barium ions in a tandem linear ion trap," *Journal of Applied Physics* **89**, 4592 (2001).

[54] B. Thestrup, B. Toftmann, J. Schou, B. Doggett, and J. G. Lunney, "Ion dynamics in laser ablation plumes from selected metals at 355 nm," *Applied Surface Science* **197**, 175 (2002).

[55] A. V. Steele, *Barium Ion Cavity QED and Triply Ionized Thorium Ion Trapping*, PhD thesis Georgia Institute of Technology 2008.

[56] P. H. Dawson, *Quadrupole mass spectrometry and its applications* (Elsevier Scientific Pub. Co. ; distributor for the U.S. and Canada, Elsevier/North-Holland, Amsterdam New York, 1976).

[57] D. J. Berkeland, "Linear Paul trap for strontium ions," *Review of Scientific Instruments* **73**, 2856 (2002).

[58] Y. Hashimoto, H. Hasegawa, T. Baba, and I. Waki, "Mass selective ejection by axial resonant excitation from a linear ion trap," *Journal of the American Society for Mass Spectrometry* **17**, 685 (2006).

[59] H. Higaki, K. Ito, R. Takai, K. Nakayama, W. Saiki, K. Izawa, and H. Okamoto, "Axial resonances of Ar+ ions observed in a linear Paul trap," *Hyperfine Interactions* **174**, 77 (2007).

[60] G. S. Dobson and C. G. Enke, "Axial focusing following low kinetic energy pulsed extraction from a miniature linear ion trap," *Rapid Communications in Mass Spectrometry* **21**, 2905 (2007).

[61] G. A. Salazar and T. Masujima, "Computer simulation of the gap-tripole ion trap with linear injection, 3D ion accumulation, and versatile packet ejection," *Journal of the American Society for Mass Spectrometry* **19**, 1367 (2008).

[62] M. E. Belov, E. N. Nikolaev, R. Harkewicz, C. D. Masselon, K. Alving, and R. D. Smith, "Ion discrimination during ion accumulation in a quadrupole interface external to a Fourier transform ion cyclotron resonance mass spectrometer," *International Journal of Mass Spectrometry* **208**, 205 (2001).

[63] Y. Hashimoto, H. Hasegawa, H. Satake, T. Baba, and I. Waki, "Duty cycle enhancement of an orthogonal acceleration TOF mass spectrometer using an axially-resonant excitation linear ion trap," *Journal of the American Society for Mass Spectrometry* **17**, 1669 (2006).

[64] M. G. Raizen, J. M. Gilligan, J. C. Bergquist, W. M. Itano, and D. J. Wineland, "Ionic-Crystals in a Linear Paul Trap," *Physical Review A* **45**, 6493 (1992).

[65] T. Baba and I. Waki, "Cooling and mass-analysis of molecules using laser-cooled atoms," *Japanese Journal of Applied Physics Part 2-Letters & Express Letters* **35**, L1134 (1996).

[66] J. C. Schwartz, M. W. Senko, and J. E. P. Syka, "A two-dimensional quadrupole ion trap mass spectrometer," *Journal of the American Society for Mass Spectrometry* **13**, 659 (2002).

[67] M. Drewsen, I. Jensen, J. Lindballe, N. Nissen, R. Martinussen, A. Mortensen, P. Staanum, and D. Voigt, "Ion Coulomb crystals: a tool for studying ion processes," *International Journal of Mass Spectrometry* **229**, 83 (2003).

[68] I. Scientific Instrument Services, "Simion 8.0," 2006.

[69] C. Ma, H. W. Lee, and D. M. Lubman, "Computer-Simulation of the Operation of a 3-Dimensional Quadrupole Ion Trap," *Applied Spectroscopy* **46**, 1769 (1992).

[70] L. Ding and F. L. Brancia, "Electron capture dissociation in a digital ion trap mass spectrometer," *Analytical Chemistry* **78**, 1995 (2006).

[71] C. L. Hendrickson, S. C. Beu, G. T. Blakney, and A. G. Marshall, "SIMION modeling of ion image charge detection in Fourier transform ion cyclotron resonance mass spectrometry," *International Journal of Mass Spectrometry* **283**, 100 (2009).

[72] M. Drewsen and A. Broner, "Harmonic linear Paul trap: Stability diagram and effective potentials," *Physical Review A* **6204**, (2000).

[73] J. J. Coon, J. E. P. Syka, J. C. Schwartz, J. Shabanowitz, and D. F. Hunt, "Anion dependence in the partitioning between proton and electron transfer in ion/ion reactions," *International Journal of Mass Spectrometry* **236**, 33 (2004).

[74] X. Yu, W. Jin, S. A. McLuckey, F. A. Londry, and J. W. Hager, "Mutual storage mode ion/ion reactions in a hybrid linear ion trap," *Journal of the American Society for Mass Spectrometry* **16**, 71 (2005).

[75] D. R. Denison, "Operating Parameters of a Quadrupole in a Grounded Cylindrical Housing," *Journal of Vacuum Science & Technology* **8**, 266 (1971).

[76] D. J. Douglas and N. V. Konenkov, "Influence of the 6th and 10th spatial harmonics on the peak shape of a quadrupole mass filter with round rods," *Rapid Communications in Mass Spectrometry* **16**, 1425 (2002).

[77] N. Konenkov, F. Londry, C. F. Ding, and D. J. Douglas, "Linear quadrupoles with added hexapole fields," *Journal of the American Society for Mass Spectrometry* **17**, 1063 (2006).

[78] M. Sudakov and D. J. Douglas, "Linear quadrupoles with added octopole fields," *Rapid Communications in Mass Spectrometry* **17**, 2290 (2003).

[79] R. M. Jones, D. Gerlich, and S. L. Anderson, "Simple radio-frequency power source for ion guides and ion traps," *Review of Scientific Instruments* **68**, 3357 (1997).

[80] R. M. Jones and S. L. Anderson, "Simplified radio-frequency generator for driving ion guides, traps, and other capacitive loads," *Review of Scientific Instruments* **71**, 4335 (2000).

[81] P. B. O'Connor, C. E. Costello, and W. E. Earle, "A high voltage RF oscillator for driving multipole ion guides," *Journal of the American Society for Mass Spectrometry* **13**, 1370 (2002).

[82] R. Mathur and P. B. O'Connor, "Design and implementation of a high power rf oscillator on a printed circuit board for multipole ion guides," *Review of Scientific Instruments* **77**, (2006).

[83] S. R. Systems, "Operating Manual and Programming Reference: Models RGA 100, RGA 200, and RGA 300 Residual Gas Analyzer," 2009.

[84] C. Monroe, D. M. Meekhof, B. E. King, S. R. Jefferts, W. M. Itano, D. J. Wineland, and P. Gould, "Resolved-Side-Band Raman Cooling of a Bound Atom to the 3d Zero-Point Energy," *Physical Review Letters* **75**, 4011 (1995).

[85] W. W. Macalpine and R. O. Schildknecht, "Coaxial Resonators with Helical Inner Conductor," *Proceedings of the Institute of Radio Engineers* **47**, 2099 (1959).

[86] D. J. Berkeland, J. D. Miller, J. C. Bergquist, W. M. Itano, and D. J. Wineland, "Minimization of ion micromotion in a Paul trap," *Journal of Applied Physics* **83**, 5025 (1998).

[87] A. Gallagher, "Oscillator Strengths of Ca II, Sr II, and Ba II," *Phys. Rev.* **157**, 24 (1967).

[88] D. J. Berkeland and M. G. Boshier, "Destabilization of dark states and optical spectroscopy in Zeeman-degenerate atomic systems," *Physical Review A* **65**, (2002).

[89] N. D. Scielzo, J. R. Guest, E. C. Schulte, I. Ahmad, K. Bailey, D. L. Bowers, R. J. Holt, Z.-T. Lu, T. P. O'Connor, and D. H. Potterveld, "Measurement of the lifetimes of the lowest $P13$ state of neutral Ba and Ra," *Phys. Rev. A* **73**, 010501 (2006).

[90] C. J. Erickson, B. Neyenhuis, and D. S. Durfee, "High-temperature calcium vapor cell for spectroscopy on the 4s(2) S-1(0)-4s4p P-3(1) intercombination line," *Review of Scientific Instruments* **76**, (2005).

[91] Y. Li, T. Ido, T. Eichler, and H. Katori, "Narrow-line diode laser system for laser cooling of strontium atoms on the intercombination transition," *Applied Physics B-Lasers and Optics* **78**, 315 (2004).

[92] J. A. Neuman, P. Wang, and A. Gallagher, "Robust High-Temperature Sapphire Cell for Metal Vapors," *Review of Scientific Instruments* **66**, 3021 (1995).

[93] C. R. Vidal and J. Cooper, "Heat-Pipe Oven - a New, Well-Defined Metal Vapor Device for Spectroscopic Measurements," *Journal of Applied Physics* **40**, 3370 (1969).

[94] R. L. Cavasso, A. Mirage, A. Scalabrin, D. Pereira, and F. C. Cruz, "Laser spectroscopy of calcium in hollow-cathode discharges," *Journal of the Optical Society of America B-Optical Physics* **18**, 1922 (2001).

[95] D. Hansen and A. Hemmerich, "Doppler-free spectroscopy of metastable calcium in a discharge heat pipe," *Physical Review A* **72**, (2005).

[96] G. Ferrari, P. Cancio, R. Drullinger, G. Giusfredi, N. Poli, M. Prevedelli, C. Toninelli, and G. M. Tino, "Precision frequency measurement of visible intercombination lines of strontium," *Physical Review Letters* **91**, (2003).

[97] P. Grundevik, M. Gustavsson, G. Olsson, and T. Olsson, "Hyperfine-Structure and Isotope-Shift Measurements in the 6s5d[- -]6p5d Transitions of Ba-I in the Far-Red Spectral Region," *Zeitschrift Fur Physik a-Hadrons and Nuclei* **312**, 1 (1983).

[98] I. Varian, "UHV-24/UHV-24p Ionization Gauge Instruction Manual," 2004.

[99] U. I. Safronova, W. R. Johnson, and M. S. Safronova, "Excitation energies, polarizabilities, multipole transition rates, and lifetimes in ThIV," *Physical Review A* **74**, (2006).

[100] R. Loudon, *The quantum theory of light*Oxford science publications, 3rd ed. (Oxford University Press, Oxford ; New York, 2000).

[101] J. H. Moore, C. C. Davis, and M. A. Coplan, *Building scientific apparatus : a practical guide to design and construction*, 2nd ed. (Addison-Wesley, Redwood City, Calif., 1989).

[102] M. P. Seah, "Channel Electron Multipliers - Quantitative Intensity Measurement - Efficiency, Gain, Linearity and Bias Effects," *Journal of Electron Spectroscopy and Related Phenomena* **50**, 137 (1990).

[103] M. Krems, J. Zirbel, M. Thomason, and R. D. DuBois, "Channel electron multiplier and channelplate efficiencies for detecting positive ions," *Review of Scientific Instruments* **76**, (2005).

[104] N. R. Reagan, L. C. Frees, and J. W. Gray, "Mass-Dependent Effects of Channel Electron Multipliers in Residual-Gas Analyzers," *Journal of Vacuum Science & Technology a-Vacuum Surfaces and Films* **5**, 2389 (1987).

[105] D. R. Leibrandt, R. J. Clark, J. Labaziewicz, P. Antohi, W. Bakr, K. R. Brown, and I. L. Chuang, "Laser ablation loading of a surface-electrode ion trap," *Physical Review A* **76**, (2007).

[106] V. H. S. Kwong, "Production and Storage of Low-Energy Highly Charged Ions by Laser Ablation and an Ion Trap," *Physical Review A* **39**, 4451 (1989).

[107] R. D. Knight, "Storage of Ions from Laser-Produced Plasmas," *Applied Physics Letters* **38**, 221 (1981).

[108] T. Gudjons, F. Arbes, M. Benzing, F. Kurth, and G. Werth, "Spatial Fluorescence Distribution and Laser Cooling of Ca+ in a Paul Trap," *Physica Scripta* **T59**, 396 (1995).

[109] I. N. Laboratory.

[110] N. N. D. Center, "NuDat 2.5,".

[111] R. A. Boll, D. Malkemus, and S. Mirzadeh, "Production of actinium-225 for alpha particle mediated radioimmunotherapy," *Applied Radiation and Isotopes* **62**, 667 (2005).

[112] C. J. Campbell, "Personal Communication," 2009.

[113] S. Mirzadeh, "Personal Communication," 2009.

[114] P. Langevin, "The recombination and mobilities of ions in gases," *Annales De Chimie Et De Physique* **28**, 433 (1903).

[115] G. Gioumousis and D. P. Stevenson, "Reactions of Gaseous Molecule Ions with Gaseous Molecules .5. Theory," *Journal of Chemical Physics* **29**, 294 (1958).

[116] J. Troe, "Statistical Adiabatic Channel Model of Ion Neutral Dipole Capture Rate Constants," *Chemical Physics Letters* **122**, 425 (1985).

[117] D. O. Schissler and D. P. Stevenson, "Reactions of Gaseous Molecule Ions with Gaseous Molecules .2.," *Journal of Chemical Physics* **24**, 926 (1956).

[118] F. H. Field, J. L. Franklin, and F. W. Lampe, "Reactions of Gaseous Ions .1. Methane and Ethylene," *Journal of the American Chemical Society* **79**, 2419 (1957).

[119] N. Boelrijk and W. H. Hamill, "Effects of Relative Velocity Upon Gaseous Ion-Molecule Reactions - Charge Transfer to Neopentane Molecule," *Journal of the American Chemical Society* **84**, 730 (1962).

[120] B. H. Mahan, "Molecular Orbital Correlations and Ion-Molecule Reaction Dynamics," *Journal of Chemical Physics* **55**, 1436 (1971).

[121] R. Johnsen and M. A. Biondi, "Measurements of Radiative Charge-Transfer Reactions of Doubly and Singly Charged Rare-Gas Ions with Rare-Gas Atoms at Thermal Energies," *Physical Review A* **18**, 996 (1978).

[122] R. Johnsen and M. A. Biondi, "Thermal-Energy Charge-Transfer, Quenching, and Association Reactions of Doubly Charged Ions in the Rare-Gases," *Physical Review A* **20**, 87 (1979).

[123] R. Johnsen and M. A. Biondi, "Charge-Transfer Coefficients for the O+(2d)+N2 and O+(2d)+O2 Excited Ion Reactions at Thermal-Energy," *Journal of Chemical Physics* **73**, 190 (1980).

[124] H. M. Holzscheiter and D. A. Church, "Near Thermal Charge-Transfer between Ar-+2 and N-2," *Journal of Chemical Physics* **74**, 2313 (1981).

[125] D. A. Church and H. M. Holzscheiter, "Charge-Transfer from Molecular-Hydrogen to Stored O-2+ and O-3+ Ions," *Physical Review A* **40**, 54 (1989).

[126] E. W. McDaniel, *Ion-molecule reactions*Wiley-Interscience series in atomic and molecular collisional processes (Wiley-Interscience, New York,, 1970).

[127] R. Johnsen, F. R. Castell, and M. A. Biondi, "Rate Coefficients for Oxidation of Ti+ and Th+ by O2 and No at Low Energies," *Journal of Chemical Physics* **61**, 5404 (1974).

[128] H. M. Holzscheiter and D. A. Church, "Charge-Transfer Reaction of Multicharged Oxygen Ions with O-2," *Physics Letters A* **86**, 25 (1981).

[129] H. Chatham, D. Hils, R. Robertson, and A. C. Gallagher, "Reactions of He+, Ne+, and Ar+ with Ch4, C2h6, Sih4, and Si2h6," *Journal of Chemical Physics* **79**, 1301 (1983).

[130] D. A. Church, "Charge-Changing Collisions of Stored, Multiply-Charged Ions," *Journal of Modern Optics* **39**, 423 (1992).

[131] L. Andrews and H. G. Cho, "Infrared spectrum and structure of CH2=ThH2," *Journal of Physical Chemistry A* **109**, 6796 (2005).

[132] J. Marçalo, J. P. Leal, and A. P. de Matos, "Gas phase actinide ion chemistry: Activation of alkanes and alkenes by thorium cations," *International Journal of Mass Spectrometry and Ion Processes* **157-158**, 265 (1996).

[133] D. R. Lide, *CRC Handbook of Chemistry and Physics, 88th Edition (Crc Handbook of Chemistry and Physics)* (CRC, 2007).

[134] I. Angeli, "A consistent set of nuclear rms charge radii: properties of the radius surface R(N,Z)," *Atomic Data and Nuclear Data Tables* **87**, 185 (2004).

[135] M. S. Safronova, "Personal Communication," 2009.

[136] O. Becker, K. Enders, G. Werth, and J. Dembczynski, "Hyperfine-Structure Measurements of the Eu-151+, Eu-153+ Ground-State," *Physical Review A* **48**, 3546 (1993).

[137] K. Enders, E. Stachowska, G. Marx, C. Zölch, U. Georg, J. Dembczynski, and G. Werth, "Ground-state hyperfine-structure measurements of unstable *Eu*+ isotopes in a Paul ion trap," *Phys. Rev. A* **56**, 265 (1997).

[138] I. Airgas, "Airgas 2009 Product Catalog," 2009.

VITA

Layne R. Churchill was born in Grand Rapids, Michigan.